

Structure-Mechanical Property Relationship Modelling using the Finite Element Method and Machine Learning

Nikolić, Filip

Doctoral thesis / Disertacija

2025

Degree Grantor / Ustanova koja je dodijelila akademski / stručni stupanj: **University of Rijeka, Faculty of Engineering / Sveučilište u Rijeci, Tehnički fakultet**

Permanent link / Trajna poveznica: <https://um.nsk.hr/um:nbn:hr:190:638642>

Rights / Prava: [Attribution 4.0 International](#)/[Imenovanje 4.0 međunarodna](#)

Download date / Datum preuzimanja: **2025-03-20**



Repository / Repozitorij:

[Repository of the University of Rijeka, Faculty of Engineering](#)



UNIVERSITY OF RIJEKA
FACULTY OF ENGINEERING

Filip Nikolić

**Structure-Mechanical Property
Relationship Modelling using Finite
Element Method and Machine Learning**

DOCTORAL THESIS

Rijeka, 2024.

UNIVERSITY OF RIJEKA
FACULTY OF ENGINEERING

Filip Nikolić

**Structure-Mechanical Property
Relationship Modelling using Finite
Element Method and Machine Learning**

DOCTORAL THESIS

Supervisors: Prof. D.Sc. Marko Čanadija & Prof. D.Sc. Ivan
Štajduhar

Rijeka, 2024.

SVEUČILIŠTE U RIJECI
TEHNIČKI FAKULTET

Filip Nikolić

**Modeliranje odnosa strukture i mehaničkih
značajki metodom konačnih elemenata i
strojnim učenjem**

DOKTORSKI RAD

Mentori: Prof. dr. sc. Marko Čanađija & Prof. dr. sc. Ivan
Štajduhar

Rijeka, 2024.

Acknowledgement

Completing this dissertation has been a journey that I could not have undertaken alone. I would like to extend my sincere thanks to everyone who has supported and helped me throughout this process.

First and foremost, I would like to express my deepest gratitude to my supervisor, Prof. D. Sc. Marko Čanađija, for his significant support and mentoring. His previous guidance was crucial in my decision to pursue this doctoral study, and his support has been a cornerstone of my academic journey.

I would also like to extend my heartfelt thanks to my co-supervisor, Prof. D. Sc. Ivan Štajduhar, for his invaluable assistance and encouragement throughout this journey. His insights and expertise have been essential to the completion of this work.

My sincere thanks go to my colleague, Martin Zlatic, at the University of Rijeka: Faculty of Engineering. His assistance and companionship throughout the PhD process has been greatly appreciated.

I am also deeply grateful to my department head, Blaž Paladin, and colleague Jasna Stanković, who supported my PhD process during my employment at Cimos d.d. Automotive Industry in Koper. Their encouragement and support were significantly helpful during this phase of my research.

Similarly, I extend my sincere thanks to my department head, Blaž Grafenauer, and colleagues Miha Škof and Matic Franjković, at Elaphe Propulsion Technologies Ltd in Ljubljana. Their support and understanding were also significantly helpful in enabling me to balance my professional responsibilities with my academic pursuits.

Furthermore, I am also grateful to Aventa Adriatic d.o.o. and its employees for their support throughout my PhD dissertation. Their encouragement was very supportive to the successful completion of this work.

I owe a great deal of appreciation to my family. To my parents, Ines and Saša Nikolić, and my grandparents, Ankica and Milenko Nikolić, your constant love and support have been the foundation of my journey. Even during the most challenging times, your encouragement has been a source of immense strength to finish this study.

Last but not least, I am grateful to all the other participants and collaborators who contributed to this research.

Thank you all for making this journey possible!

Doctoral thesis supervisors: Prof. D. Sc. Marko Čanađija and Prof. D. Sc. Ivan Štajduhar (University of Rijeka, Faculty of Engineering, Croatia)

The doctoral thesis was defended on _____ at the University of Rijeka, Faculty of Engineering, Croatia, in front of the following Evaluation Committee:

1. Prof. D. Sc. Marino Brčić, University of Rijeka: Faculty of Engineering, Croatia. Committee Chair
2. Prof. D. Sc. Zdenko Tonković, University of Zagreb: Faculty of Mechanical Engineering and Naval Architecture, Croatia
3. Assoc. Prof. D. Sc. Goran Mauša, University of Rijeka: Faculty of Engineering, Croatia

Abstract

In the present study, the structure-property relationships (SPR) are investigated using finite element analysis (FEA) and machine learning (ML) methods. The objective of the research was to create an ML model capable of predicting the temperature-dependent stress-strain response of two-phase composites, as well as the amount of heat generated during plastic deformation considering different Taylor-Quinney coefficients (TQCs). The ML model aims to achieve industrially acceptable prediction accuracy and significantly better computational efficiency compared to FEA.

Microstructure generation and FEA were used to create the datasets for the ML model, and both processes were automated using the Python programming language. FEA was performed for each representative volume element (RVE) to obtain the stress-strain response as well as the temperature increase-strain curve. This means that two separate datasets and two separate ML models were created: one for the stress-strain responses and one for the temperature increase-strain responses.

Both ML models were developed in the form of complex 3D-convolutional neural networks (CNNs), taking the microstructural configuration as input. Other input parameters included the TQC value and temperature for the first and second ML models, respectively. The outputs of the CNNs were the temperature increase-strain curves and the stress-strain curves at specific temperatures for the first and second model, respectively.

Compared to FEA, both the model for predicting temperature-dependent stress-strain curves and the model for predicting plastic deformation-induced heat generation demonstrated very good prediction accuracy suitable for industrial applications. Additionally, both models exhibited significantly faster prediction capabilities and better computational efficiency than FEA.

Keywords: machine learning; temperature-dependent stress-strain curves; structure-property relationships; finite element analysis; Taylor-Quinney coefficient

Prošireni sažetak

U ovoj studiji, odnos između strukture i svojstva (SPR) istraženi su korištenjem metode konačnih elemenata (MKE) i strojnog učenja (SU). Cilj istraživanja bio je napraviti SU model koji može predvidjeti temperaturno ovisnu vezu naprezanja i deformacije dvofaznih kompozita, kao i količinu topline koja se stvara tijekom plastične deformacije uzimajući u obzir različite Taylor-Quinneyjeve koeficijente (TQK). SU model bi trebao postići industrijski prihvatljivu točnost predviđanja i značajno bolju računsku učinkovitost u usporedbi s MKE.

Generiranje mikrostrukture i MKE korišteni su za izradu skupova podataka za SU model i oboje su automatizirani pomoću programskog jezika Python. Svaki reprezentativni volumenski element (RVE) je proračunat pomoću MKE kako bi se dobila krivulja naprezanje-deformacija kao i krivulja povećanje temperature-deformacija. To znači da su stvorena dva različita skupa podataka kao i dva različita SU modela, jedan za krivulje naprezanje-deformacija i drugi za porast temperature-deformacija.

Oba SU modela kreirana su u obliku složene 3D-konvolucijske neuronske mreže (KNM) i mikrostrukturna konfiguracija je ulaz oba SU modela. Ostali ulazni parametri bili su vrijednost TQK za prvi i temperatura za drugi SU model. Rezultati KNM-a bili su krivulja porast temperature-deformacija za prvi te krivulje naprezanja-deformacije na specifičnim temperaturama za drugi model.

U usporedbi s MKE, i model za predviđanje temperaturno-ovisnih krivulja naprezanje-deformacija te model za predviđanje krivulja povećanja temperature-deformacija pokazali su vrlo dobru točnost predviđanja prikladnu za industrijske primjene. Osim toga, oba modela su pokazala znatno brže mogućnosti predviđanja i bolju računalnu učinkovitost u odnosu na MKE.

Ključne riječi: strojno učenje; temperaturno ovisne krivulje deformacija naprezanje; odnos struktura svojstvo; metoda konačnih elemenata; koeficijent Taylor-Quinney

Contents

Abstract	I
Prošireni sažetak	II
1 Introduction	1
1.1 Motivation	1
1.2 About SPR	2
1.3 Deformation-induced Heat Generation	4
1.4 Work Structure	7
2 Related Work	9
2.1 Deformation-induced Heat Generation in Engineering Mechanics and Material Science	9
2.2 SPR in Engineering Mechanics and Material Science	11
2.3 SPR Determination via FEA	12
2.4 Overview of ML Methods in Engineering Mechanics and Material Science	13
2.5 SPR Determination via ML Methods	16
2.6 The Hypothesis	17
3 Theoretical Background of Thermomechanical Analysis	18
3.1 Introduction to Thermomechanical Analysis	18
3.2 Plasticity and Temperature Influence	20
3.3 Small Strain Thermoplasticity Constitutive Modeling	21
4 Materials and Methods	32
4.1 Generation of the RVE microstructure	34
4.2 Dataset Generation	37
4.2.1 Material Properties and Constitutive Model	38

4.2.2	Numerical Simulation Procedure	41
4.3	Overview of the ML Models	60
4.3.1	Data Preprocessing	60
4.3.2	ML Models	61
5	Results and Discussion	67
5.1	Evaluation of Different ML Models	68
5.2	Results for the Temperature-dependent Stress-strain Curves – Six Specific Temperature Levels	72
5.3	Results for the Temperature-dependent Stress-strain Curves – Random Temperature Levels	80
5.4	Results for the Temperature Increase – Strain Curves	84
5.5	Influence of Phases Distribution – Random Temperature Levels Dataset	90
5.6	Influence of Phases Distribution – Temperature Increase Strain Curves	96
6	Conclusion	102
	Bibliography	115
	List of Figures	122
	List of Tables	123
A		124
A.1	Optimization of ML Models	124
	Curriculum Vitae	128
	List of Publications	130

Chapter 1

Introduction

1.1 Motivation	1
1.2 About SPR	2
1.3 Deformation-induced Heat Generation	4
1.4 Work Structure	7

1.1 Motivation

The study of structure-property relationships and the temperature effects during plastic deformation in materials is significant in materials science and engineering. Understanding these relationships allows for the prediction and optimization of material performance and their mechanical properties, which is crucial for developing advanced materials with improved mechanical properties. This research focuses on two different areas: the micro-mechanical analysis of composite materials and the temperature increase during plastic deformation, often characterized by the TQC.

Multiphase materials are increasingly used in various engineering applications due to their superior mechanical properties, such as high strength-to-weight ratios and improved fatigue resistance. However, their complex microstructures pose significant challenges in predicting their behavior under different loading conditions. Traditional experimental and numerical methods, such as physical testing and finite element method (FEM), have been widely used to analyze the micro-mechanical behavior of composites. However, while FEA provides detailed insights, it

is computationally expensive and time-consuming, especially for large-scale and high-fidelity simulations.

The advent of ML methods offers a promising solution to these challenges. ML algorithms, trained on data generated from FEA simulations or experimental tests, can predict the behavior of composite materials and the thermal effects during plastic deformation with high accuracy and significantly reduced computational cost. By exploring the capabilities of ML, this research aims to develop predictive models that can efficiently capture the SPR, stress-strain curves and the temperature increase in materials induced by plastic deformation in dual phase materials.

The aim of this research is to find a balance between detailed but time-consuming FEA simulations and the need for fast, accurate predictions of material mechanical properties. By developing ML models that can accurately predict the micro-mechanical properties of multi-phase materials and the thermal effects during plastic deformation, this research contributes to more efficient material analysis, design, and optimization processes. Ultimately, this work aims to advance the field of materials science and mechanical engineering by providing robust tools for predicting material behavior, thereby accelerating the development of innovative materials for diverse engineering applications.

1.2 About SPR

The study and understanding of SPR are fundamental in materials science and engineering. These relationships highlight the connection between the microscopic structure of materials and their macroscopic properties that govern their behavior under various loading conditions. The current literature is full of studies showing how changes in structural arrangement at different levels of the hierarchy can significantly alter the properties and resulting performance of materials at the macroscopic level. SPR are important for many engineering materials such as metals, polymers, ceramics, composites, biomaterials, and many others. SPR determine the functional aspects of materials, such as mechanical, thermal, electrical and optical properties. Therefore, understanding the relationship between structure and properties allows us to develop materials for specific applications. Consequently, understanding these relationships is crucial to both scientific progress and industrial innovation, driving advances in fields as diverse as energy, healthcare, aerospace, electronics, sustainable development and many more.

This concept of SPR is inherently multiscale. It begins at the atomic level by considering

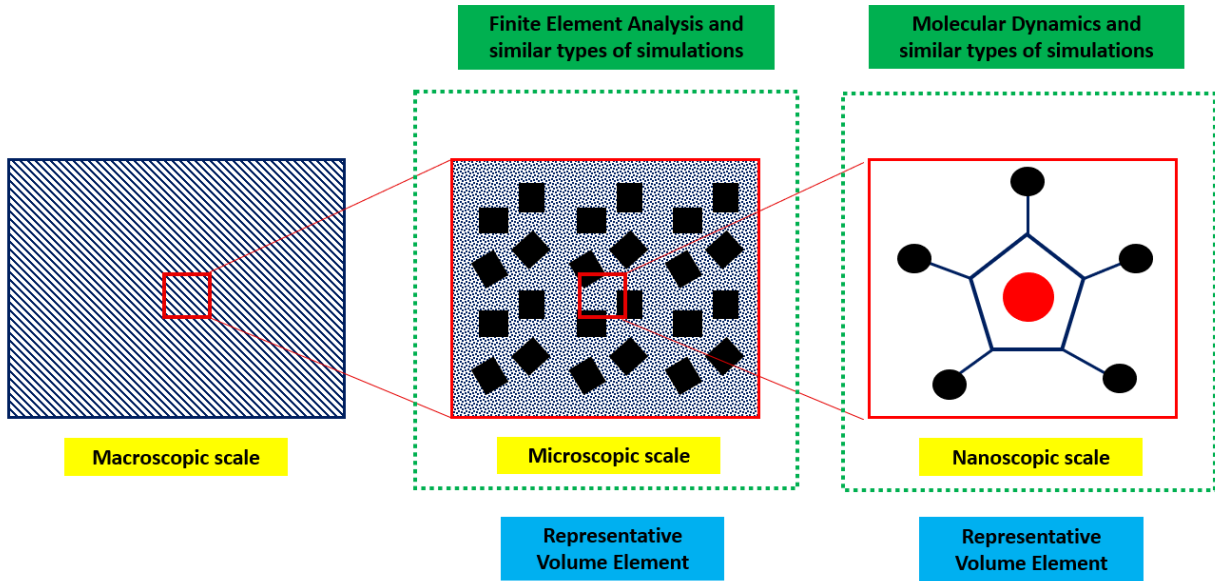


Figure 1.1: Schematic representation of the process of SPR and their representative evaluation by numerical simulations.

the types of atoms and the nature of their bonds. Next, it involves the arrangement of atoms in a lattice structure that forms crystalline or amorphous phases. Further up the scale, the focus shifts to the arrangement of these phases, defects, grain boundaries, and other microstructural features that result from various synthesis and processing operations. At a larger scale, the focus is on the architecture of the material, which includes aspects such as the shape, size, and microstructural arrangement. This multiscale nature often presents a major challenge, as changes at one level can have an influence on other levels. However, it also provides a set of tools for tuning the properties of materials by manipulating their structure. A schematic representation of SPR and their simulation is illustrated in Fig 1.1.

The link between the structural and functional properties of materials is often established by theoretical models and empirical observations, supported by advances in analytical calculations. It is important to establish mathematical methods for interpreting SPR, while it is even more important to provide experimental testing results to validate mathematical models. Modern experimental methods, such as electron microscopy, X-ray diffraction, and spectroscopy, have proven to be excellent in the scanning of microscopic structures of materials. At the same time, computational tools such as FEA, molecular dynamics simulations, and ML algorithms provide numerical approaches to understanding these complex relationships.

The correlation between the structural characteristics and functional attributes of materials

is typically drawn using theoretical models and empirical findings, further reinforced by progressive analytical methods. Creating a mathematical approach for decoding structure-property correlations is important, but even more important is the provision of empirical test results to authenticate these mathematical models. State-of-the-art experimental procedures like scanning electron microscopy and X-ray inspection have proven very successful in examining the microstructures of various materials. Concurrently, computational methodologies, including FEA, molecular dynamics, and ML, serve as supplementary resources to investigate the relationships and interactions within these materials.

Even with the substantial progress achieved so far, the understanding of SPR remains insufficient. Each category of materials presents unique challenges and prospects. Furthermore, in today's world, where nanomaterials and sophisticated functional materials are at the forefront, new and more intricate methods that challenge conventional ones to establish SPR are necessary. The existing gaps in our understanding encourage continuous research in this domain and call for a strategy that merges materials science, physics, chemistry, engineering, computer science, and more.

1.3 Deformation-induced Heat Generation

While temperature-dependent SPR provides valuable insights into the thermal stability and properties of materials, in this concept, it is equally important to address the thermal effects arising from mechanical deformation. Deformation-induced heat generation, a phenomenon in materials science, is important for understanding and improving manufacturing processes. During plastic deformation of materials, as in the manufacturing (i.e., especially machining) of metals and polymers, most of the work done during deformation is converted to heat energy. This transition, deformation-induced heating, is a consequence of thermodynamic irreversibility and interacts with plastic deformation on several levels, including affecting mechanical properties and material behavior during and after deformation.

Plastic deformation involves the permanent mechanical deformation of materials under applied stress that exceeds beyond the yield strength of the material. This involves dislocation motion and propagation within the material, resulting in a realignment of the atomic lattice. This process is inherently non-elastic, permanently altering the shape of the material. However, these internal dislocation activities are not completely efficient and result in energy dissipation

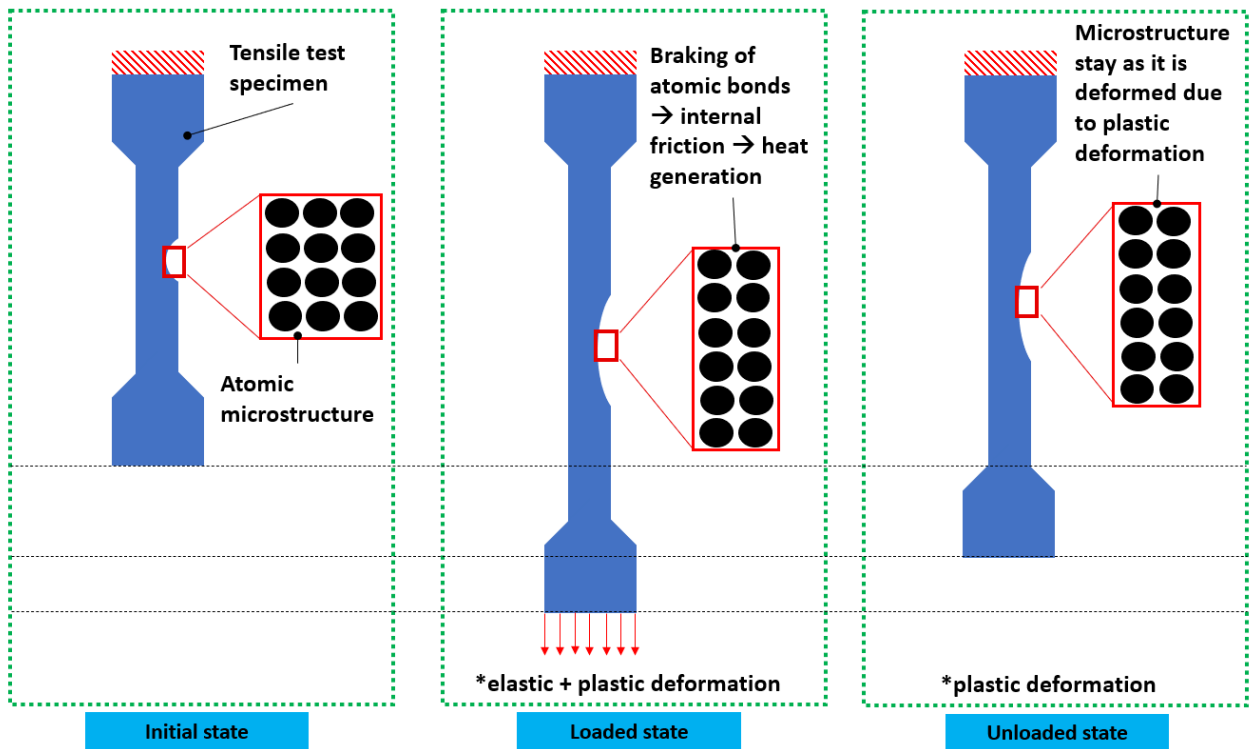


Figure 1.2: Schematic representation of the process of plastic deformation-induced heat generation.

by heat. This phenomenon of deformation-induced heat generation arises from dislocation motion and friction between the dislocations and the crystal lattice during plastic deformation. It is particularly important in high-speed deformation processes such as machining, where the rate of heat generation can lead to a noticeable increase in temperature. A schematic representation of the phenomenon of plastic deformation-induced heat generation is illustrated in Fig 1.2.

The TQC plays an important role in quantifying the fraction of plastic deformation energy that is converted to heat during deformation. John B. Taylor and George I. Quinney proposed this coefficient in 1934 as an empirical measure that captures the energy partitioning during plastic deformation. In essence, the TQC indicates the fraction of the plastic work done during the deformation process that is converted to heat, thus indicating the thermal efficiency of the deformation.

Normally, TQC values range from 0 to 1. A coefficient of 1 means that all the work done is converted to heat, indicating total thermodynamic inefficiency. In contrast, a coefficient of 0 represents a fully efficient, thermodynamically reversible process in which no work is converted to heat. In reality, however, most materials exhibit a TQC that lies between these two extremes, mostly between 0.7 and 0.9, illustrating the inherent irreversibility of plastic deformation pro-

cesses in the real-world. In that case, the part of the energy which is not converted into heat, is transformed into the energy of elastic deformation and stress around dislocations and defects.

The TQC, usually denoted as β , is defined as the ratio of the dissipated energy to the total plastic work. Mathematically, it could be expressed as:

$$\beta = \frac{W_{\text{dissipated}}}{W_{\text{plastic}}}, \quad (1.1)$$

where $W_{\text{dissipated}}$ is the work converted into heat increasing the temperature of the material and W_{plastic} is the total plastic work done on the material increasing the internal energy, primarily in the form of dislocation structures and other defects. Considering a volume element undergoing plastic deformation, the total work done per unit volume, W_{plastic} , can be expressed as:

$$W_{\text{plastic}} = \sigma \epsilon_p, \quad (1.2)$$

where σ is the applied stress and ϵ_p is the plastic strain. Now, the heat generated per unit volume, $W_{\text{dissipated}}$, due to plastic deformation can be written as:

$$W_{\text{dissipated}} = \beta \sigma \epsilon_p = \rho c_p \Delta T, \quad (1.3)$$

where ρ is the density of the material, c_p is the specific heat capacity at constant pressure and ΔT is the change in temperature. Note that this equation is valid in the case of adiabatic process. In other words, the process duration is very short and heat cannot flow to other parts of the material by means of heat conduction. However, that specific heat capacity at a constant volume and constant pressure should be almost the same for solids, therefore, it does not matter which one is used. Now, by combining the above equations the TQC could be expressed as:

$$\beta = \frac{\rho c_p \Delta T}{\sigma \epsilon_p}, \quad (1.4)$$

and alternatively, the change in temperature could be expressed as

$$\Delta T = \frac{\beta \sigma \epsilon_p}{\rho c_p}. \quad (1.5)$$

The concept of deformation-induced heat generation is of particular importance in various fields of engineering and materials science. It is important for understanding and controlling thermal effects in manufacturing processes, predicting material behavior under severe loading

conditions, and improving process control. Understanding deformation-induced heat generation enables better control and reduction of potentially harmful effects such as overheating, structural weakening, and thermally induced phase transformations in materials. It also helps optimize manufacturing processes and improve the structural integrity and performance of the final product. The TQC plays an important role in these efforts, providing a quantitative measure for predicting the extent of heat generation, which can then be used in thermal modeling and simulations.

In summary, an understanding of deformation-induced heat generation, supported by an improved understanding of the TQC, has important implications for materials science and the manufacturing industry. It opens a lot of opportunities for better process controls and innovative material applications. In the following chapters, ML and FEA are utilized to study the amount of heat generated during plastic deformation.

1.4 Work Structure

Given the introduction into deformation-induced heat generation and SPR, it is clear that this phenomenon has significant importance for both mechanical engineering and materials science. Section 1 concludes a short introduction, providing a simple overview of the topic of SPR and deformation-induced heat generation.

Chapter 2 further addresses the practical and theoretical aspects of ML and FEA, and their use in mechanical engineering and materials science, highlighting their synergistic potential in predicting and understanding SPR and heat-induced deformation. The relevance and details of these research areas, including their various applications and limitations, are explored and their contextual importance within the broader scientific and academic landscape is presented.

Chapter 3 covers the theoretical aspects of Thermomechanical Analysis (TMA), which combines thermodynamics and mechanics to study material behavior under thermal and mechanical loads. It introduces TMA principles, focusing on total strain (mechanical and thermal components). The chapter addresses challenges in modeling nonlinear behaviors, time-dependent effects like creep and stress relaxation, phase transformations, and multiscale modeling. It discusses plasticity, including dislocation mechanisms, strain hardening, and temperature effects on metals. Finally, it outlines constitutive modeling approaches for thermoplasticity, highlighting small and finite strain theory.

Moving forward, Chapter 4 details the FEA models, dataset generation techniques, and ML models employed in this study. Shortly, the FEA models were developed to account for nonlinear geometry and material behavior and have been implemented using Abaqus software. Output data from the FEA models include stress-strain curves and temperature increase-strain curves. In addition, data analysis is performed using the Python programming language to generate inputs for the ML models, which is also explained. The ML models employed in this study take the form of complex 3D convolutional neural networks (CNNs) and include inputs such as microstructural configurations, temperature, and TQC. Chapter 4 provides a detailed explanation of the models.

Chapter 5 presents the results obtained from the study, providing an overview of the accuracy achieved by the ML models and investigating their performance. Several metrics are employed to assess the predictive capabilities and reliability of the ML models in capturing the desired outcomes. The evaluation includes measures of predictive accuracy, computational efficiency and model robustness. These findings offer valuable insights into the effectiveness and potential of the ML models, informing future advancements in the field.

Finally, Chapter 6 presents the conclusions drawn from the study. This section summarizes the key findings and contributions of the study.

Chapter 2

Related Work

2.1 Deformation-induced Heat Generation in Engineering Mechanics and Material Science	9
2.2 SPR in Engineering Mechanics and Material Science	11
2.3 SPR Determination via FEA	12
2.4 Overview of ML Methods in Engineering Mechanics and Material Science	13
2.5 SPR Determination via ML Methods	16
2.6 The Hypothesis	17

Chapter 2 addresses the practical and theoretical aspects of ML and FEA within mechanical engineering and materials science. It points out their potential for predicting and understanding SPR and deformation-induced heat generation. This chapter also explores their applications, limitations, and their overall importance in the broader scientific landscape. Furthermore, it also addresses related work on the topic.

2.1 Deformation-induced Heat Generation in Engineering Mechanics and Material Science

Material properties are one of the most important factors in mechanical engineering and materials science. Knowing the exact material properties, the operational behavior of the product can be determined much more accurately. Material properties are usually determined by experimental testing procedures which can sometimes be very time-consuming and costly. Consid-

ering that for many engineering applications the description of materials at room temperature is inadequate, this problem is much more complicated for properties at temperatures other than room temperature. In addition, it is also useful to know the amount of heat generated during deformation of material and this phenomenon has been studied for a long time, see for example [1, 2]. This could have an effect on the material's properties, as its properties change with increasing temperature [3]. Normally, the material becomes softer with increasing temperature. In most cases, the deformation of the material can be divided into plastic and elastic deformation, and both can be rate dependent or independent. The plastic deformation is usually much more interesting, since it belongs to the irreversible processes [1, 4]. Moreover, most of the heat generated during deformation is caused by plastic deformation [2]. As already mentioned, the fraction of plastic energy that is converted to heat is described by the TQC and can depend on the type of material, strain rate, amount of plastic strain and many other factors, see for example [5–8]. However, it is often assumed to be between 70% and 90%, [5] and usually increases with deformation magnitude, see for example [3, 5, 7, 9].

Some recent studies on the topic of deformation-induced heat generation are discussed in the following paragraph. Rubtsov and Kolubaev [10] performed numerical simulations to study heat generation due to plastic deformation during material friction. Bjerke et al. [11] numerically and experimentally investigated the effect of plastic deformation on heat generation during dynamic fracture of polycarbonates. Li et al. [12] performed numerical molecular dynamics simulations to investigate the heat generation during sliding between metals. They conclude that most of the heat generated during friction is related to plastic deformation. Brennhaugen et al. [13] used an experimental approach to study the heat generation in bulk metallic glass due to plastic deformation. Alghamdi et al. [14] on the other hand studied plastic deformation-induced heat generation in polyethylene nanocomposites. Zaera et al. [9] showed that the TQC in 304 grade stainless steel depends on the stress, strain, and strain rate. Benaarbia et al. [15] calibrated the FEA model using tensile and cyclic tests validated by comparing predicted and experimentally observed energy responses. Soares and Hokka [16] presented a study on the effects of strain rate and adiabatic heating on the dynamic compressive response of titanium. Lieou and Bronkhorst [17] performed FEA simulations to investigate conductive and convective energy losses during experiments to determine TQC. Their FEA results agreed very well with the experimental results. Finally, an alternative approach to bypass the TQC is proposed in [18, 19]. The formulation is based on a dissipation that accounts for previous history of deformation and

does not require TQC. In general, evidence suggests that this topic is quite attractive for both mechanical engineering and materials science domains.

2.2 SPR in Engineering Mechanics and Material Science

To present a variety of research directions in the field of SPRs, this section will provide a general overview of various applications. As already said, SPR has lately become very attractive in the field of engineering mechanics and computational materials science, and numerous works on the subject could be found. For example, Homer [20] showed how high-throughput simulations have had an impact on grain boundary SPR and other complex microstructural phenomena. This author presented very complex simulation approaches, including a link between the atomic and crystallographic structures of grain boundaries, the complicated nature of grain boundary-dislocation interactions, and more. Kang et al. [21] simulated the chain flexibility and mechanical properties of polyimides with different chemical structures using molecular dynamics techniques to establish SPR. On the other hand, Ustov et al. [22] studied cellulose nanoparticles including only a single particle level. They applied statistical polymer physics methodologies to electron and atomic force microscopy images. Jancar et al. [23] provided a detailed investigation on the SPR of the nano-scale particles structural behavior in polymer nanocomposites to understand the behavior at the macroscale. Zhang et al. [24] explored the trend in numerical simulations and factors in mechanism of microstructure evolution in titanium alloy.

Temperature-dependent SPR is on the other hand much less attractive due to increased complexity, although some research on this topic could be found as well. Gupta et al. [25] studied the thermal behavior of poly(ethylene terephthalate) set at different temperatures and under different conditions. The behavior was studied by calorimetric measurements with differential scanning, while structural studies were performed by X-ray diffraction and infrared absorption spectrophotometry. Baranek et al. [26] developed SRP for CuAAC-based polymer networks with a library of synthesized multifunctional azides and alkynes. They analyzed properties such as the glass transition temperature. Schlund et al. [27] analyzed dynamic mechanical properties as a function of temperature between $-100\text{ }^{\circ}\text{C}$ and $130\text{ }^{\circ}\text{C}$. They investigated the styrene-butyl acrylate copolymer latexes group of materials. However, this research could be rather classified as chemical engineering than mechanical engineering. On the other hand, Yan et al. [28] presented an approach to predict the work performance of the final products based on given manufacturing

parameters for additively manufactured materials. They used computational models to design and manipulate the SPR combinations to use the raw materials as efficiently as possible based on the process SPR. They used a very complex coupled simulation approach consisting of a thermal-fluid-flow model for melting powder particles. As it could be seen, some researches on the topic of temperature-dependent SPR could be found but this topic is much less attractive.

2.3 SPR Determination via FEA

Various methods are employed to determine SPR of materials, while FEA is one of the most commonly used techniques in this context. There are many studies on SPR determination through FEA, however, for some of the most important ones, the interested reader is referred to the following sources [25–36]. Saucedo and Marrow [29] proposed an FEA approach that normalizes energy release by jointly applying two models: a mesh-free method and cellular automata. They considered the influence of microstructure on quasi-brittle properties in the FEA framework by coupling micro and macro-level simulations to obtain an integrated perspective. Subsequently, Metzger and Seifert [30] proposed a microstructure-based finite-element analysis (MFEM) for determining microstructure-dependent inelastic behavior of lamellar grey cast iron materials. Their innovative approach was validated by correlating the stress-strain curves derived from their model with experimental tensile and compression tests. Prabu and Karunamoorthy [31] developed a 2D MFEA model for predicting the mechanical behavior of metal matrix composites (MMCs), assuming that the properties depend on the particle arrangement in the microstructure. The model accurately predicted failures such as particle fracture, interfacial decohesion, matrix yielding, and the effects of particle arrangement on failure mechanisms.

Furthering the use of 2D MFEA, Phillion et al. [32] used it to predict the behavior of aluminum alloys. They created a model incorporating several microstructural features such as semi-solid equiaxed spherical grains in the as-cast state, interconnected liquid films, and pores at triple junctions. A model-based constitutive relationship was derived from over fifty simulations to account for these microstructural characteristics. Finally, Kim et al. [33] developed a 2D MFEA to investigate fracture and fatigue behavior of Al₂O₃ ceramics, concluding that grain arrangement and size significantly influence the overall length and progression of cracks. Despite the advancements offered by these models, it should be noted that numerical models that consider microstructures can be computationally intensive, especially for large-scale engi-

neering problems. Therefore, many researchers choose to use 2D FEA, even though this might compromise the accuracy of results.

2.4 Overview of ML Methods in Engineering Mechanics and Material Science

In the recent decade, the volume of data generated has significantly exceeded our ability to process it, resulting in the increased adoption of ML algorithms. They also became an attractive topic in the field of mechanical engineering. At this point, only a few results are selected as an illustration of possible applications. For example, the ML methods could be used to accelerate FEA calculations. Capuano and Rimoli [37] developed an ML method that directly relates the state of finite elements to their forces, simplifying the process by eliminating the need to find the internal displacement field and perform numerical iterations. Their results show that this method can reduce computational costs, especially for problems including nonlinear effects. Nie et al. [38] used a deep learning approach based on various CNNs to predict stress fields in elastic deformation of solids. They used the representation embedded CNN with a single input channel and the squeeze-and-excitation residual network modules embedded fully convolutional neural network (SE-Res-FCN) with multiple input channels. The authors' results indicated that the SE-Res-FCN model can accurately predict the stress field. As input to the model, they used an image including the information about the geometry and position of the load. The output of the model is a colored image of the stress field that contains a Mises stress value for each pixel. In addition, this research and the references therein indicate that ML is increasingly being used in areas of computer engineering, such as computational fluid dynamics (CFD), design and topology optimization, nonlinear dynamics analysis, autonomous vehicles, molecular dynamics simulation, quantum learning, and so on. The interested reader is referred to this research for more information. In conclusion, deep learning models have significantly higher computational efficiency compared to conventional FEA models since FEA might be too slow to drive a design process. Therefore, ML models have great foreground and potential in structural design and topology optimization [38].

ML models can be roughly divided into two main groups: Shallow learning models and deep learning models [39]. Shallow learning models such as support vector machine, artificial neural network (ANN), decision tree, etc. are usually used for some very simple assignments where

the data has more straightforward patterns and limited complexity. These tasks often involve smaller datasets and less computational demand. On the other hand, deep learning models like CNNs are usually used for complex tasks that involves complex relationship such as image and speech recognition. This kind of task usually involves larger datasets. However, these types of models are usually much more computationally demanding. As shown in [40, 41], complex models have significantly outperformed simple ML models such as linear regression and the like. However, it is also shown there that significantly more computational effort is required to train a CNN. Complex models are also implemented in [42] and [43] for the task of casting defects recognition from X-ray images. The authors used around 640 000 images to train the ML model while generative adversarial networks were implemented to generate additional data. A transfer learning based approach based on the CNN in [44] showed significantly better results in comparison with other reconstruction approaches such as physical descriptor decision trees, Gaussian fields, two-point correlation, etc.

Wei et al. [39] have, on the other hand, explored the use of ML models in materials science, and it turns out to be quite broad and attractive. For example, DeCost et al. [45] applied a complex deep learning model and automated microstructure segmentation. They presented this application to complex multiphase microstructures. Chowdhury et al. [46] proposed an ML based classification approach to classify micrographs. References could also be found in their study dealing with the classification of precipitate shapes in the microstructure of nickel-based superalloys and cast irons. DeCost et al. [47] also present an approach to classify microstructures based on the support vector machine. Since this model is relatively simple, the achieved the accuracy around only 80%. Azimi et al. [41] also used segmentation based deep learning models to classify microstructures. They use an approach based on CNNs augmented with max-voting. Exl et al. [48] used experimental datasets of 700 and 800 experiments to identify the microstructure features in structured large-grain Nd₂Fe₁₄B permanent magnets. The Stoner-Wohlfarth method is presented in that research, as well as a reduced-order model to determine local switching field maps that guide the data-driven learning procedure. Yucel et al. [49] connected microscopic images of cold-rolled high-strength low-alloy steels to their representative mechanical properties from experimental tensile tests. They examined only yield strength, ultimate tensile strength and elongation. Unfortunately, their ML model developed in the study only works for constant initial conditions before heat treatment. This means that if the initial conditions change, the ML model must be rebuilt based on those conditions. Pokuri et al. [50]

have shown that mapping microstructure to photovoltaic performance can achieve very high test accuracy (up to 96%) using a very complex VGG-16 CNN.

In addition, several studies including ML methods in material science are described below. In the first study [51], optical micrographs predicted SDAS in aluminum alloys, requiring image preparation to reduce ML training parameters. Despite precision, it needed manual hyperparameter setting, limiting usability. Later, automated SDAS detection using grayscale images and ML algorithms was proposed [52], removing manual intervention. Additionally, an ML model for defect detection in cast aluminum alloys was developed [53]. Another study [54] used FEA and ML to analyze the SPR process, creating a model for temperature-dependent stress-strain response in two-phase composites. The ML model showed high prediction accuracy and excellent computational efficiency. A recent study [55] developed an ML model to predict deformation-induced heat generation, considering various TQC values and phase distributions, improving adaptability and robustness for industrial use. All these studies have advanced understanding in aluminum casting, SPR, and heat generation, optimizing processes and product quality. They highlight ML and DL methods' potential and provide a foundation for future research.

Of special interest for this research are thermomechanical problems. King et al. [56] developed a physically informed ML model that can effectively capture the temperature increase during shear assisted processing and extrusion. However, the work does not explicitly model the temperature increases based on the detailed microstructural characteristics or other direct material property relationships. Instead, the complex interplay between process parameters and temperature dynamics is captured by the ML model. Pantalé et al. [57] used an ML model to accurately replace the analytical formulation of a Johnson–Cook behavior law in explicit finite element simulations. Temperature is included in the formulation, but its influence manifests itself by affecting the flow law. Several different network architectures were tested. In the context of predicting stresses and temperature in the thermoelasticity of rubber, the neural network based on the strain invariants shows better performance than the network based on the stress-strain model [58]. However, plastic deformation is not relevant in such cases and was not taken into account.

2.5 SPR Determination via ML Methods

In addition, in the recent past, many studies on the SPR and ML techniques topics have appeared. Zhang et al. [59] used a simple ML approach based on ANNs for SPR determination. Jung et al. [60], on the other hand, used much more complex ML algorithms for the SPR task. They predicted elongation, ultimate tensile strength, and strain localization index from multiphase RVEs. First, they used numerical simulations to determine SPR, and created a dataset of 1 100 different microstructures. Later, they used this dataset to train the ML model. In addition, they used techniques for dimensionality reduction. They kept with multidimensional scaling (MDS) and principal component analysis (PCA), and they compared MDS and PCA and concluded that MDS performs much better for the given task. However, caution should be exercised with these types of methods because, while they may reduce the final ML model input size as well as the overall computational cost, they may also decrease the overall predictive accuracy of the ML model. It should also be noted that the microstructures created in their study do not represent a real-world material. Latypov and Kalidindi [61] also created a dataset with virtual microstructures that do not represent a real-world material. Their approach was similar, and they created a dataset for training using FEA, while later using the ML model to establish SPR. In addition, they were also forced to use PCA to reduce the dimensions of the RVEs. Finally, they reduced their 3D $27 \times 27 \times 27$ input size to the 2D projection. On the other hand, Yang et al. [62] created a dataset of microstructures representing a high-contrast composite. They also established SPR via complex ML models while investigating only linear elastic properties. Wang et al. [63] also used similar a approach while they investigated SPR phenomena in polymer nanocomposites. Cecen et al. [64] also conducted a similar approach to establish SPR based on a 3D CNN. However, their study in the end also involved PCA methods such as regression and 10-fold cross-validation scheme for dimension reduction. Liu et al. [65] demonstrated the deep material network transfer learning approach to establish SPR. Kotha et al., Frankel et al. Chaudry et al. [66–68] predicted material constitutive models based on SPR while also using ML algorithms. None of the above authors included the influence of temperature. In addition, most authors only predicted the elastic properties and didn't predict complete stress-strain curves. As already mentioned, this could be very important for many industrial as well as academic applications.

In addition, studies that performed prediction of stress-strain curves using ML algorithms are presented in the continuation of the text. Anyhow, neither one of them directly predicted

temperature-dependent stress-strain curves based on the microstructural configuration of the 3D-RVE. For example, Jiang et al. [69] investigated stress-strain responses of the real-world material, but their study does not consider the microstructure configuration. Wen et al. [70] studied the deformation as a function of time and temperature using ML algorithms. However, their study was limited to lithium single-phase based metals, and the microstructure information was not taken into account as well. Yang et al. [71] also investigated the stress-strain responses of composites, but used 2D geometry instead of 3D. Versino et al. [72] also conducted a similar study, but examined a material constitutive model as a function of strain rate and temperature. Their model also did not take into account the arrangement of the microstructure. Kronberger et al. [73] presented a genetic programming approach to calibrate temperature-dependent material properties. Thus, neither one of these studies directly predicted temperature-dependent stress-strain curves based on the microstructural configuration of the 3D-RVE.

2.6 The Hypothesis

The evaluation of deformation-induced heat generation and the determination of temperature-dependent stress-strain curves have already been presented in the literature. In addition, as shown in 2.5, many studies dealing with SPR via ML methods can be found in the recent past. However, neither one of them directly address the plastic deformation-induced heat generation and the temperature-dependent stress-strain curves based on the microstructural configuration. Therefore, the hypothesis is as follows: the plastic deformation-induced heat generation and the temperature-dependent stress-strain curves based on microstructural configuration could be determined by ML methods.

Chapter 3

Theoretical Background of Thermomechanical Analysis

3.1	Introduction to Thermomechanical Analysis	18
3.2	Plasticity and Temperature Influence	20
3.3	Small Strain Thermoplasticity Constitutive Modeling	21

Chapter 3 deals with the theoretical background of the TMA. It introduces the principles and applications of TMA, which integrates thermodynamics and mechanics to understand material behavior under combined thermal and mechanical loads. It begins with an introduction to the basic concepts of TMA, highlighting the significance of total strain, considering both mechanical and thermal components. The section further addresses challenges associated with modeling nonlinear behaviors, time-dependent effects such as creep and stress relaxation, phase transformations, and etc. Additionally, it explores plasticity and its temperature influences in metals, detailing dislocation mechanisms, strain hardening, and temperature impacts on mechanical properties. Finally, it outlines constitutive modeling approaches for thermoplasticity, discussing small and finite strain theories.

3.1 Introduction to Thermomechanical Analysis

TMA of solids is an interdisciplinary field that combines effects of thermodynamics and mechanics to study the behavior of materials under the simultaneous influence of thermal and mechanical loads. This type of analysis is crucial for predicting material behavior at elevated tem-

peratures, ensuring its structural integrity. It is used in numerous sectors in mechanical, civil engineering as well as in material science and other sectors.

The fundamental concept of TMA can be expressed through the concept of total strain, which is defined by the following equation:

$$\epsilon_{\text{total}} = \epsilon_{\text{mechanical}} + \epsilon_{\text{thermal}} \quad (3.1)$$

In this equation, total strain is the sum of mechanical strain and thermal strain. This relationship is important in TMA as it shows that both mechanical and thermal effects contribute to the overall strain experienced by a material. Further details, including the constitutive model and its formulation, will be discussed in the following sections.

The integrity and reliability of materials are one of the most important factors in engineering design and application. As materials are subjected to operational environments, they experience changes in temperature and mechanical loads that can significantly influence their behavior and properties. The interaction between thermal and mechanical effects can lead to complex phenomena such as thermal expansion, thermal stress, creep, and phase transformations. Understanding these interactions is essential for the development of materials and structures that can withstand extreme conditions and maintain their functionality over time. In a lot of engineering applications, components are often exposed to mechanical stresses and elevated temperature simultaneously. However, constitutive models of TMA are generally much more complex than constitutive models excluding temperature and that is the most important reason why is the temperature effects often neglected in analysis of structural components.

While significant advancements have been made in TMA during the past several years, several challenges remain:

- **Nonlinear Behavior:** Many materials exhibit nonlinear behavior under large deformations and/or high temperatures. Developing accurate models to capture this behavior is still an ongoing research subject, see for example [58, 74–77]
- **Time-Dependent Effects:** Creep and stress relaxation are time-dependent phenomena that affect material performance. Integrating these effects into thermomechanical models is crucial for the accurate life analysis of structural components, see for example [78–81].
- **Phase Transformations:** Some materials undergo phase changes at certain temperatures, affecting their mechanical properties, see for example [82–86].

- **Multiscale Modeling:** Bridging the gap between microscale material behavior and macroscale structural response is a significant challenge. Multiscale modeling techniques aim to integrate different length scales to provide an understanding of material behavior.

Multiscale modeling is one of the most important challenge these days since it is crucial to understand behavior of materials at a different scale level (e.g., macro, micro, nano, etc.). However, in this research, it is the fundamental idea to understand mechanical behavior at a microscale by modeling mechanical properties that can be used constitutive models on the macroscale.

3.2 Plasticity and Temperature Influence

The microstructural aspects of metals reveal that they are composed of numerous small crystals, or grains, each with its own orientation. These grains are interspersed with various types of defects, including point defects, such as vacancies and interstitial atoms, and line defects, primarily dislocations. Dislocations, categorized into edge and screw types, play a crucial role in the plastic deformation process. Furthermore, planar defects, like grain and twin boundaries, significantly influence the mechanical behavior of metals. These microstructural features and their interactions ultimately determine how a metal responds to mechanical stress.

The physical mechanisms governing plastic deformation in metals are diverse. In an ideal crystal, deformation occurs when the applied stress reaches a threshold sufficient to shear atomic planes. However, real materials exhibit plasticity at much lower stresses due to the presence of defects. Dislocations, particularly, facilitate this process. An edge dislocation involves the movement of atoms along a slip plane, causing the dislocation line to glide through the crystal. In contrast, a screw dislocation moves parallel to the applied shear stress. Both types of dislocations enable planes of atoms to slide past one another, thus contributing to plastic deformation.

Another mechanism, twinning, involves the reorientation of part of the crystal lattice to form a mirror image across a twinning plane. This process is notably faster than slip and is more prevalent in body-centered cubic and hexagonal close-packed structures, especially at lower temperatures. Unlike slip, which does not alter the crystal orientation, twinning changes the lattice orientation, thereby aiding in accommodating deformation.

As plastic deformation progresses, the density of dislocations increases, leading to significant interactions between them. These interactions cause strain hardening, a phenomenon where the material becomes harder and stronger. Strain hardening mechanisms include forest harden-

ing, where dislocations are imposed by others, and kinematic hardening, which is related to the directional nature of slip plane interactions. This increased density of dislocations and their subsequent interactions are crucial in enhancing the material's strength during plastic deformation.

Temperature also plays a significant role in dislocation movement. At elevated temperatures, dislocations can climb, a process involving atomic diffusion that allows dislocations to move perpendicular to their slip planes. This ability to climb enhances the material's capacity to deform plastically at higher temperatures, thereby influencing its mechanical properties.

Yield stress softening is another critical phenomenon observed in metals. After plastic deformation begins, a material's yield stress often decreases, a process influenced by dynamic recovery mechanisms where dislocation structures rearrange to reduce internal stresses. Factors such as strain rate and temperature profoundly affect yield stress softening, impacting the mechanical performance of metals during prolonged deformation.

3.3 Small Strain Thermoelasticity Constitutive Modeling

The thermoelasticity framework presented in this section is based on the assumption of small strain behavior, with the constitutive model derived from [87–89]. In particular, the softening of the yield function and the temperature evolution are presented. These represent the basis of the calculations in the following chapters. Furthermore, each point \mathbf{x} in the configuration $\mathcal{B} \subset \mathbb{R}^3$ is displaced at a given time t by a vector $\mathbf{u} = \mathbf{u}(\mathbf{x}, t) = \{u_x, u_y, u_z\}^T$. Given this assumption, the infinitesimal strain tensor is:

$$\boldsymbol{\epsilon}(\mathbf{x}, t) = \frac{1}{2} \left(\nabla \mathbf{u}(\mathbf{x}, t) + (\nabla \mathbf{u}(\mathbf{x}, t))^T \right), \quad (3.2)$$

and it can be decomposed into:

$$\boldsymbol{\epsilon} = \boldsymbol{\epsilon}_{te} + \boldsymbol{\epsilon}_p \quad (3.3)$$

$$\boldsymbol{\epsilon}_{te} = \boldsymbol{\epsilon}_e + \boldsymbol{\epsilon}_t, \quad (3.4)$$

where the plastic strain tensor $\boldsymbol{\epsilon}_p$ represents a portion of the deformation associated with permanent changes in the solid, and $\boldsymbol{\epsilon}_{te}$ is the thermoelastic strain. Thermoelastic strain consists of two parts: the elastic strain $\boldsymbol{\epsilon}_e$ and the thermal strain $\boldsymbol{\epsilon}_t$. The elastic strain $\boldsymbol{\epsilon}_e$ is responsible for

the stresses within the material, while the thermal strain ϵ_t is solely dependent on temperature variations.

Considering the rate of deformation tensor within the infinitesimal framework, employing its additive decomposition (Eqs. (3.3),(3.4)) the following relation for strain rate could be written:

$$\mathbf{d} = \dot{\epsilon} = \dot{\epsilon}_e + \dot{\epsilon}_t + \dot{\epsilon}_p. \quad (3.5)$$

At this part the following boundary conditions (BC) must be defined:

$$\mathbf{u}(\mathbf{x}, t) = \mathbf{u}_0(\mathbf{x}, t) \quad \forall \mathbf{x} \in \partial_u \mathcal{B}, \quad (3.6)$$

$$\boldsymbol{\sigma}(\mathbf{x}, t) \cdot \mathbf{n}(\mathbf{x}) = \mathbf{t}(\mathbf{x}, t, \mathbf{n}) \quad \forall \mathbf{x} \in \partial_t \mathcal{B}, \quad (3.7)$$

where $\mathbf{n}(x)$ is a vector normal to the surface $\partial_t \mathcal{B}$ at point x while $\partial_u \mathcal{B}$ is the part of the boundary where displacements are prescribed and $\boldsymbol{\sigma}$ is the Cauchy stress tensor.

The integral form of the conservation of momentum represents the balance of forces and momentum in a deformable body. It states that the rate of change of momentum inside a body is equal to the applied forces, which include both surface and body forces. In the equation below, this is formulated with the specific boundary terms related to surface traction and body force acting on the domain. The first term describes the time rate of change of the momentum inside the volume \mathcal{B} , while the second term represents the contribution of surface forces (tractions) over the boundary $\partial \mathcal{B}$. The right-hand side integrates the body forces acting inside the body.

$$\frac{d}{dt} \int_{\mathcal{B}} \rho \mathbf{v} dV - \int_{\partial \mathcal{B}} \mathbf{t}(x, t) dS = \int_{\mathcal{B}} \mathbf{f} dV. \quad (3.8)$$

Here, ρ is the mass density, \mathbf{v} is the velocity vector, $\mathbf{t}(\mathbf{x}, t)$ is the traction force (force per unit area) applied to the surface $\partial \mathcal{B}$ at the boundary. \mathbf{f} is the body force per unit volume (e.g., gravitational forces), \mathcal{B} is the volume of the body and $\partial \mathcal{B}$ is the surface of the body. This formulation ensures the physical consistency of momentum conservation for a deformable solid by relating the internal momentum, surface tractions, and body forces. However, based on the balance of linear momentum (e.g., law of conservation of momentum) in every point of the body, the equation could be rewritten in its local form:

$$\operatorname{div} \boldsymbol{\sigma} + \rho \mathbf{b} = 0, \quad (3.9)$$

where $\boldsymbol{\sigma}$ are stresses in the body and $\rho \mathbf{b}$ are external volumetric forces in the body. In other words, this formulation assumes inertial effects are negligible. Additionally, it is important to remember that the principle of angular momentum requires the Cauchy stress tensor $\boldsymbol{\sigma}$ to be symmetric ($\boldsymbol{\sigma} = \boldsymbol{\sigma}^T$).

Next, the first law of thermodynamics in its global form should be introduced. It states that the rate of change of total energy, consisting of internal energy E and kinetic energy K within a domain \mathcal{B} , is equal to the external mechanical power input P_x plus the heat added Q . This balance ensures energy conservation within the system as it interacts with its surroundings through mechanical work and heat transfer:

$$\frac{d}{dt}(E + K) = P_x + Q. \quad (3.10)$$

The local form of first law of thermodynamic (e.g., energy balance in every point of the body) could be derived from the global form following the procedure in [88]:

$$\rho \dot{e} - \boldsymbol{\sigma} : \dot{\boldsymbol{\epsilon}} - \rho r + \operatorname{div} \mathbf{q} = 0, \quad (3.11)$$

where the kinematic relationship Eq. (3.5) has been utilized. Here, $\rho \dot{e}$ term represents the rate of change of internal energy per unit volume of the material. The density, ρ , refers to the mass per unit volume, while \dot{e} refers to the rate of change of specific internal energy (internal energy per unit mass). Therefore, $\rho \dot{e}$ gives the total rate of change of internal energy in a given volume of the material. r is the heat source per unit mass, and when multiplied by the mass density ρ , it represents the total heat generation per unit volume. This could come from internal heating sources such as chemical reactions or radiative sources within the material. Next, $\boldsymbol{\sigma}$ is Cauchy stress tensor, representing the internal stresses within the material, $\dot{\boldsymbol{\epsilon}}$ is strain rate tensor, describing the rate of deformation in the material while the term $\boldsymbol{\sigma} : \dot{\boldsymbol{\epsilon}}$ represents the rate of mechanical work per unit volume (or power per unit volume). The term $\operatorname{div} \mathbf{q}$ is divergence of the heat flux vector, representing the rate at which heat is being transferred out of or into a given volume.

Moreover, the second law of thermodynamics must also be incorporated alongside this law. The second law of thermodynamics serves to limit the conversion of heat into mechanical work. Similarly, it dictates the direction of heat flux, allowing it to flow only from hot to cold and not

the other way around. The global form of the second law states that the rate of change of entropy in a system is the sum of entropy generation within the system and the entropy flux across the system's boundaries due to heat transfer. The term $\int_{\mathcal{B}} \rho \dot{\eta}$ is always positive and ensures that the entropy generation due to irreversible processes is always non-negative, in line with the second law. In its most common form, it can be written as:

$$\frac{dS}{dt} = \int_{\mathcal{B}} \rho \dot{\eta} dV + \frac{1}{\theta} \int_{\partial \mathcal{B}} \mathbf{q} \cdot \mathbf{n} dS \quad (3.12)$$

where $\frac{dS}{dt}$ is the total rate of change of entropy in the system, $\rho \dot{\eta}$ is the entropy generation rate in the local form, which is always non-negative due to the irreversibility of natural processes ($\int_{\mathcal{B}} \rho \dot{\eta} \geq 0$), θ is the absolute temperature, \mathbf{q} is the heat flux vector, \mathbf{n} is the outward-pointing normal vector at the boundary $\partial \mathcal{B}$ and $\int_{\partial \mathcal{B}} \mathbf{q} \cdot \mathbf{n} dS$ represents the entropy flux through the boundary of the domain.

Furthermore, for the infinitesimal setting, the following equations could be written [87]:

$$D = \rho \dot{\eta} - \rho r + \operatorname{div} \mathbf{q} - \frac{1}{\theta} \mathbf{q} \cdot \nabla \theta \geq 0, \quad (3.13)$$

where divergence of heat flux

$$\operatorname{div} \left(\frac{\mathbf{q}}{\theta} \right) = \frac{1}{\theta} \operatorname{div} \mathbf{q} - \frac{1}{\theta^2} \mathbf{q} \cdot \nabla \theta \quad (3.14)$$

was used. This equation defines how the heat flux spreads and how its behavior changes with respect to the temperature field. Now $\rho \dot{\eta}$ is again entropy a quantity that is always non-negative due to the irreversible nature of real-world processes. ρr is internal heat source and \mathbf{q} is heat flux vector, which describes the direction and magnitude of heat flow in the system. $\operatorname{div} \mathbf{q}$ represents the divergence of the heat flux vector, which captures how heat is spreading or dispersing within the system. This inequality can be separated into two constraints in terms of dissipation [87]:

$$D_{\text{loc}} = \rho \theta \dot{\eta} - \rho r + \operatorname{div} \mathbf{q} \geq 0, \quad (3.15)$$

$$D_{\text{con}} = -\frac{1}{\theta} \mathbf{q} \cdot \nabla \theta \geq 0, \quad (3.16)$$

$$D = \rho \theta \dot{\eta} = D_{\text{loc}} + D_{\text{con}} \geq 0. \quad (3.17)$$

where D_{loc} local (internal) dissipation and D_{con} is dissipation due to heat conduction.

Local dissipation represents the internal generation of entropy due to heat sources and flux within the material. The terms reflect how internal heat sources and heat distribution contribute to overall entropy production. Conductive dissipation on the other hand describes the entropy production due to heat conduction, where heat flows from regions of high temperature to regions of low temperature. The negative sign in Eq. (3.16) indicates that heat flows in the direction opposite to the temperature gradient, generating entropy in the process. After establishing the general framework for infinitesimal strain, it is necessary to specify the constitutive behavior particular to thermoplasticity.

The internal energy e is typically characterized in terms of the following variables (strain ϵ , entropy η and internal variables α (e.g., isotropic/kinematic hardening)):

$$e = e(\epsilon, \eta, \alpha). \tag{3.18}$$

A suitable choice of observable variables includes the strain ϵ and the temperature θ , as directly measuring entropy is a significantly complex task. Therefore, the Legendre transform, which relates the internal energy e to the Helmholtz free energy ψ , can be applied

$$e(\epsilon, \eta, \alpha) = \psi(\epsilon, \theta, \alpha) + \theta\eta, \tag{3.19}$$

where $\theta\eta$ is remaining energy which represents the portion of the internal energy that accounts for entropy in the system (e.g., thermal contribution to the internal energy which cannot be converted directly into mechanical work). Furthermore, the Helmholtz free energy is expressed in terms of temperature, making it a more suitable choice for describing the constitutive behavior of the material. The Helmholtz free energy plays a significant role in TMA as it provides a measure of the energy available in a system to perform work. In the context of TMA, Helmholtz free energy is particularly useful because it describes the coupling between thermal and mechanical effects in materials.

The internal variables should capture and characterize the hardening state of the material. Considering this, and based on the earlier discussions and the strain tensor additive decomposition, the internal variables for thermoplasticity include $\alpha = \{\epsilon_p, \alpha_i, \alpha_k\}$. Here, α_i is a scalar defining isotropic hardening, and α_k is a second-order tensor defining kinematic hardening. Usually, one tensor suffices, but multiple tensors ($\alpha_k^{(j)}, j = 1, \dots, n$) might be needed for com-

plex hardening. Anyhow, in this research, kinematic hardening will not be of interest since cyclic loading is not applied, thus, the Helmholtz free energy ψ now depends on:

$$\psi(\boldsymbol{\epsilon}, \theta, \boldsymbol{\epsilon}_p, \alpha_i). \quad (3.20)$$

However, the strain tensors $\boldsymbol{\epsilon}_p$ and $\boldsymbol{\epsilon}$ are inherently linked by the constraint of additive decomposition as described in Eq. (3.4). As a result, the variables within the Helmholtz free energy are redefined using different interpretation:

$$\psi(\boldsymbol{\epsilon} - \boldsymbol{\epsilon}_p, \theta, \alpha_i) = \psi(\boldsymbol{\epsilon}_{te}, \theta, \alpha_i). \quad (3.21)$$

It should be noted that Eq. (3.21) later serves for the calculation of stresses (e.g., the supplied energy is later used for stresses, heat, and other effects).

This suggests that the free energy can be formulated in terms of the thermoelastic strain $\boldsymbol{\epsilon}_{te}$, analogous to the thermoelastic constitutive behavior. For thermoplasticity, the Helmholtz free energy of a thermoelastic material is extended by including contributions from the hardening variable α_i .

The internal energy evolution is characterized by its rate, which is determined using Eq. (3.18):

$$\dot{e} = \dot{\psi} + \dot{\theta}\eta + \theta\dot{\eta}, \quad (3.22)$$

while the specific selection of state variables in Eq. (3.21) gives the Helmholtz free energy rate (e.g., derivation of Helmholtz free energy in time):

$$\dot{\psi} = \partial_{\boldsymbol{\epsilon}_{te}} \psi : \dot{\boldsymbol{\epsilon}}_{te} + \partial_{\theta} \psi \dot{\theta} + \partial_{\alpha_i} \psi \dot{\alpha}_i. \quad (3.23)$$

Now, with the internal energy rate established, the local energy balance, following certain rearrangements (Eqs. (3.22) and (3.11)) becomes:

$$\rho\theta\dot{\eta} - \rho r + \operatorname{div} \mathbf{q} = \boldsymbol{\sigma} : \dot{\boldsymbol{\epsilon}} - \rho\theta\dot{\eta} - \rho\dot{\psi}. \quad (3.24)$$

This outcome can now be utilized within the framework of the second law of thermodynamics (Eqs. (3.13) and (3.23)) and after some transformations the following equation could be obtained:

$$D = \boldsymbol{\sigma} : \dot{\boldsymbol{\epsilon}} - \rho\theta\dot{\eta} - \rho\dot{\psi} - \frac{1}{\theta}\mathbf{q} \cdot \nabla\theta \geq 0, \quad (3.25)$$

or:

$$D = (\boldsymbol{\sigma} - \rho\partial_{\boldsymbol{\epsilon}_{te}}\psi) : \dot{\boldsymbol{\epsilon}}_{te} + \boldsymbol{\sigma} : \dot{\boldsymbol{\epsilon}}_p - \rho(\eta + \partial_{\theta}\psi)\dot{\theta} - \rho\partial_{\alpha_i}\psi\dot{\alpha}_i - \frac{1}{\theta}\mathbf{q} \cdot \nabla\theta \geq 0. \quad (3.26)$$

The latter form is now employed to establish relationships between the Helmholtz free energy ψ and variables corresponding to the state variables. Consider the following particular scenarios of thermodynamic processes:

- Solid with a uniform temperature field ($\theta = \text{const.}$), yielding $\nabla\theta = \mathbf{0}$. Assume that the temperature remains unchanged over time, i.e., $\dot{\theta} = 0$. This process is purely mechanical, operating under the assumption that no plastic strains develop, resulting in all strain hardening variables being zero. The process is entirely reversible. This simplifies Eq. (3.26), revealing that the stress tensor corresponds to the infinitesimal thermoelastic strain tensor:

$$(\boldsymbol{\sigma} - \rho\partial_{\boldsymbol{\epsilon}_{te}}\psi) : \dot{\boldsymbol{\epsilon}}_{te} = 0 \quad \Rightarrow \quad \boldsymbol{\sigma} = \rho\partial_{\boldsymbol{\epsilon}_{te}}\psi. \quad (3.27)$$

- Purely thermal problem with constant strain and strain hardening variables: Assume the temperature field varies, i.e., $\dot{\theta} \neq 0$. The entropy term follows from Eq. (3.26) as the negative of the first derivative of the Helmholtz free energy function concerning temperature:

$$-\rho(\eta + \partial_{\theta}\psi)\dot{\theta} = 0 \quad \Rightarrow \quad \eta = -\partial_{\theta}\psi. \quad (3.28)$$

Now, the stress-like hardening variable could be introduced as:

$$q_i = -\rho\partial_{\alpha_i}\psi, \quad (3.29)$$

that is conjugate to α_i – internal state variables that describe how a material deforms or evolves under stress and temperature over time. These variables are used to capture both elastic and plastic deformations, as well as any hardening effects within the material. Variable α_i is used to describe the internal resistance to plastic deformation. As a material undergoes plastic deformation, it often hardens, meaning it becomes more resistant to further deformation.

Finally, after some rearrangement, the dissipation (Eq. (3.13)) consists of two parts:

$$D_{\text{loc}} = \boldsymbol{\sigma} : \dot{\boldsymbol{\epsilon}}_p + q_i \dot{\alpha}_i \quad (3.30)$$

$$D_{\text{con}} = \frac{1}{\theta} \mathbf{q} \cdot \nabla \theta \quad (3.31)$$

$$D_{\text{loc}} - D_{\text{con}} \geq 0. \quad (3.32)$$

Particularly significant for the present formulation is the concept of local dissipation. D_{loc} represents the internal irreversible processes occurring in the material, such as plastic deformation ($\boldsymbol{\sigma} : \dot{\boldsymbol{\epsilon}}_p$) which captures the energy dissipation due to plastic strain rate, which is the permanent deformation the material undergoes under stress and hardening ($q_i \dot{\alpha}_i$) represents the dissipation due to changes in the hardening variables, which describe how the material becomes more resistant to further plastic deformation as it undergoes straining. It will be shown later that D_{loc} could be replaced with the experimental form of the equation which includes TQC.

To fully determine the thermodynamic state throughout the solid, the evolution of the internal variables, as established above, must be described. However, other important considerations remain. Notably, plastic strains only develop when a specific stress threshold ($q_0(\theta)$), known as the yield stress, is reached at the given temperature. This threshold is referred to as the yield condition and it is a function of the specific material. The function ϕ that defines the yield condition is given by:

$$\phi(\boldsymbol{\sigma}, q_i; \theta) = \phi'(\boldsymbol{\sigma}, q_i; \theta) - q_0(\theta) \leq 0, \quad (3.33)$$

where $\phi'(\boldsymbol{\sigma}, q_i; \theta)$ contains an equivalent scalar representation of the current stress state (e.g., equivalent stress like von Mises or alike) at the point including work hardening effects, while $q_0(\theta)$ is a stress threshold.

The stated condition can be understood as follows: the yield surface is described by $\phi(\boldsymbol{\sigma}, q_i; \theta) = 0$. A point $(\boldsymbol{\sigma}, q_i; \theta)$ that satisfies this equation lies on the yield surface, indicating a state where plastic strains develop. When $\phi(\boldsymbol{\sigma}, q_i; \theta) < 0$, the stress state remains elastic, meaning the point is located within the elastic domain. In contrast, values of $\phi(\boldsymbol{\sigma}, q_i; \theta) > 0$ are not permissible within the scope of the classical plasticity theory considered here.

The temperature θ within the yield function ϕ governs the material's softening due to an increase in temperature and potential temperature-related changes in plastic hardening properties. In this context, θ is treated as a parameter, not a variable.

The yield stress q_0 at temperature θ generally varies linearly with temperature:

$$q_0(\theta) = q_{y,0}(\theta_0) [1 - \omega_y(\theta - \theta_0)], \quad (3.34)$$

where $q_{y,0}(\theta_0)$ represents the yield stress at the reference temperature θ_0 , and ω_y is the material parameter that dictates the degree of softening. The same linear temperature dependence can be applied to other hardening parameters in the model. Additional examples of yield functions incorporating combined linear-exponential hardening can be found in [87].

Considering the yield condition described earlier, it is clear that this condition must be integrated into the flow laws governing the evolution of internal variables. This is accomplished by applying the principle of maximum plastic dissipation, which states that the local dissipation, as defined in Eq. (3.32), must be maximized during plastic flow, subject to the constraint imposed by the yield condition. In optimization terms, it should be made sure that the energy dissipation is "optimized" or maximized under certain constraints. The idea is that the dissipation should be maximized but still obey the material's yield condition (i.e., the point at which the material starts to deform plastically). Such optimization problems are typically addressed by introducing the Lagrangian:

$$\mathcal{L}(\boldsymbol{\sigma}, q_i, \lambda; \theta) = -D_{\text{loc}} + \lambda\phi(\boldsymbol{\sigma}, q_i; \theta). \quad (3.35)$$

To align the local dissipation with the minimization framework, its sign is adjusted to minus because the goal is to maximize dissipation and the optimization technique framed to minimize something. Here, λ is referred to as the plastic multiplier. The flow rules are derived from the stationarity conditions. Utilizing D_{loc} results in:

$$\partial_{\boldsymbol{\sigma}}\mathcal{L}(\boldsymbol{\sigma}, q_i, \lambda; \theta) = -\dot{\epsilon}_p + \lambda\partial_{\boldsymbol{\sigma}}\phi(\boldsymbol{\sigma}, q_i; \theta) = 0 \quad \Rightarrow \quad \dot{\epsilon}_p = \lambda\partial_{\boldsymbol{\sigma}}\phi. \quad (3.36)$$

Similarly, the evolution of isotropic strain-like variables is determined as:

$$\partial_{q_i}\mathcal{L} = 0 \quad \Rightarrow \quad \dot{\alpha}_i = \lambda\partial_{q_i}\phi, \quad (3.37)$$

which must be complemented by the Karush–Kuhn–Tucker conditions

$$\lambda \geq 0, \quad \phi(\boldsymbol{\sigma}, q_i; \theta) \leq 0, \quad \lambda \phi(\boldsymbol{\sigma}, q_i; \theta) = 0. \quad (3.38)$$

Note that since the temperature is considered a parameter, it is excluded from the stationary conditions. Experimental research have noticed the D_{loc} as described in Eq. (3.30) overestimates the heat production. For this reason, the TQC is introduced:

$$D_{\text{loc}} = \beta \boldsymbol{\sigma} : \dot{\boldsymbol{\epsilon}}_p, \quad (3.39)$$

where β is TQC which determines how much of plastic work is converted into heat. This form of equation is often used for simplification while TQC is usually experimentally determined.

Now, all necessary quantities to compute the temperature evolution have been defined. Firstly, the definitions for stress, entropy, and stress-like terms can be incorporated into the rate of free energy, after some transformations resulting in:

$$\dot{\psi} = \frac{1}{\rho} \boldsymbol{\sigma} : \dot{\boldsymbol{\epsilon}}_{te} - \eta \dot{\theta} - \frac{1}{\rho} q_i \dot{\alpha}_i \quad (3.40)$$

Note that the entropy rate term in Eq. (3.25) can be written:

$$\rho \theta \dot{\eta} = -\rho \theta \partial_{\theta} \dot{\psi} = -\rho \theta \left(\partial_{\theta \boldsymbol{\epsilon}_{te}}^2 \psi : \dot{\boldsymbol{\epsilon}}_{te} + \partial_{\theta \theta}^2 \psi \dot{\theta} + \partial_{\theta \alpha_i}^2 \psi \dot{\alpha}_i \right) = \rho c_v \dot{\theta} + \rho \mathcal{H}, \quad (3.41)$$

where, specific heat capacity at constant deformation c_v is defined as:

$$c_v = \theta \partial_{\theta} \eta = -\theta \partial_{\theta \theta}^2 \psi, \quad (3.42)$$

and the elastic structural heating is:

$$\mathcal{H} = -\theta \partial_{\theta \boldsymbol{\epsilon}_{te}}^2 \psi : \dot{\boldsymbol{\epsilon}}_{te}. \quad (3.43)$$

Above, it is also assumed that the isotropic hardening is not influenced by temperature, so that the last term in parenthesis in Eq.(3.42) vanishes. The origins of the elastic structural heating term are linked to thermoelastic coupling, due to volume changes which arises from temperature increase.

By introducing the specific heat capacity and elastic structural heating and only the local part of the dissipation, the temperature evolution can be defined as:

$$\rho c_v \dot{\theta} = \rho r - \operatorname{div} \mathbf{q} + D_{\text{loc}} - \rho \mathcal{H}. \quad (3.44)$$

The constitutive model for the heat conduction law is usually Fourier's law of heat conduction:

$$\mathbf{q} = -k \nabla \theta, \quad (3.45)$$

where k is the isotropic coefficient of heat conduction. At the end, it should be noted that thermoelastic coupling, $\rho \mathcal{H}$, is usually neglected as well as in the present research.

Chapter 4

Materials and Methods

4.1	Generation of the RVE microstructure	34
4.2	Dataset Generation	37
4.2.1	Material Properties and Constitutive Model	38
4.2.2	Numerical Simulation Procedure	41
4.3	Overview of the ML Models	60
4.3.1	Data Preprocessing	60
4.3.2	ML Models	61

Chapter 4 provides dataset generation techniques in Section 4.1, an overview of the FEA models in Section 4.2, and ML models applied in this study in Section 4.3. The FEA models, implemented using Abaqus software, capture nonlinear geometry and material behavior. They produce output data, including stress-strain curves and temperature increase-strain curves. Furthermore, the present Chapter explains implementation of Python programming language in employment of automating the simulation process. It explains the data analysis, for which Python is used as well, and generation of inputs to the ML models. The ML models adopted in this study are complex 3D CNNs, which incorporate inputs such as microstructural configurations, temperature, and TQC. A detailed explanation of these models can be found in the present Chapter. In addition, Appendix A deals with the optimization of the ML models and explains the methodology of selecting the optimal ML model for the task at hand. Here, the performances and complexities of different ML models' configurations are presented and compared. A schematic representation of the whole process is shown in Fig. 4.1.

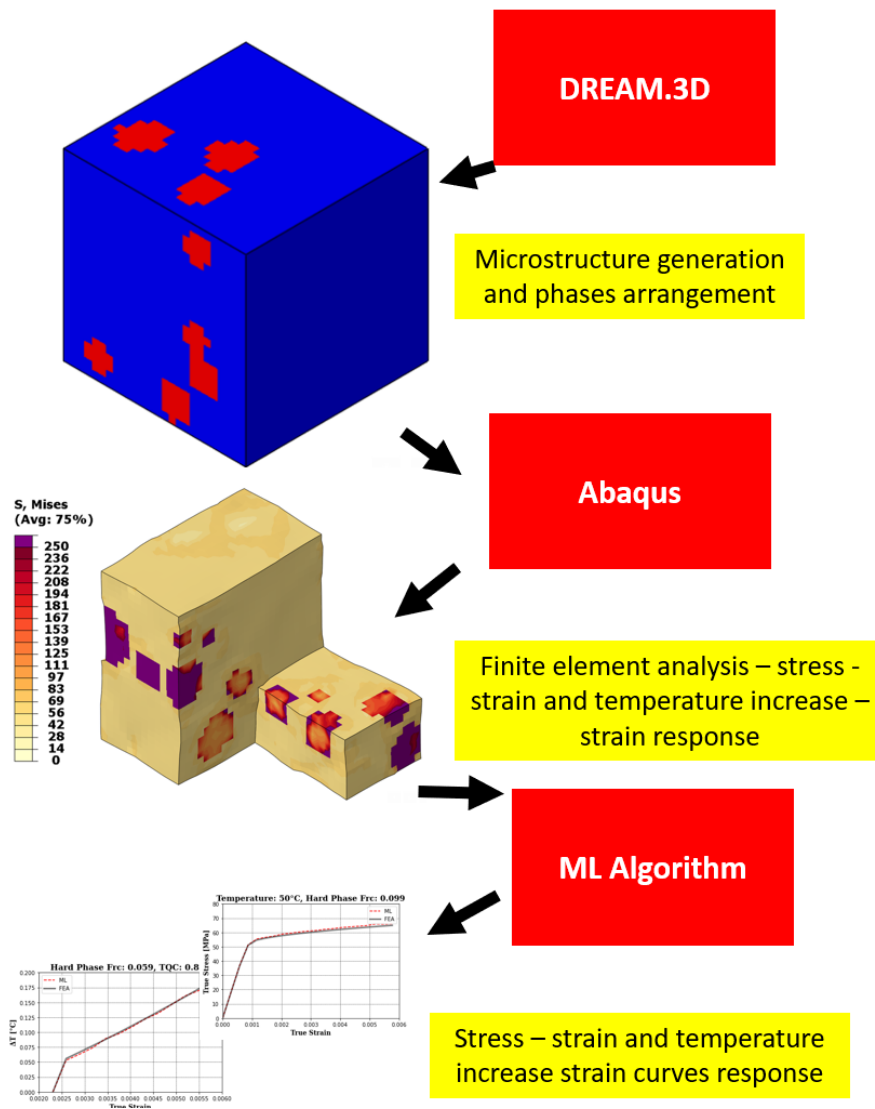


Figure 4.1: Schematic representation of the numerical procedure used in the present research.

4.1 Generation of the RVE microstructure

Obtaining SPR from dual-phase materials is often a complex task, mainly due to the large number of different microstructural variations required for material property evaluation. The focus of the present research is to investigate an equiaxed 3D dual-phase microstructure to derive the specific plasticity responses. To systematically generate RVEs for this study, the open-source software DREAM.3D [90] has been employed, which is often used in problems of this kind, see for example [60, 61]. Each generated RVE is presented in the format of a $26 \times 26 \times 26$ voxel configuration. The choice of configuration was made following an investigation into mesh convergence, as described in Section 4.2.2. The results of this investigation confirm the appropriateness of the chosen voxel dimensions and mesh density for the purpose of the current study. The selection of a $26 \times 26 \times 26$ configuration size is not arbitrary. A critical review of similar studies by other authors, including [60, 61], reveals a commonality in the size and mesh density of the RVEs used. These studies have produced highly reliable and consistent results, further validating the choice of RVE dimensions. Hence, the chosen dimensions of $26 \times 26 \times 26$ are not only consistent with existing research but are also validated by a mesh convergence study. A mesh sensitivity study is performed in Section 5.2.

It is worth noting that a large portion of the scientific community, as represented by numerous authors such as [31–33, 36, 63, 65, 91–93], predominantly prefers 2D FEA models for similar type of studies, mainly due to their computational efficiency. However, the exclusion of the third dimension carries a potential risk of compromising the overall accuracy of the results, which should not be ignored. To overcome this risk and ensure more accurate outcomes, a 3D FEM model is employed for SPR assessment in this study. It is expected that this approach will provide a more accurate representation of the physical material behavior, allowing for a more authentic representation of the phenomena under investigation. However, it is critical to be aware of the challenges associated with this methodological choice. At a 3D scale, the number of microstructural configurations increases exponentially. This fact makes it necessary to generate a significantly larger number of microstructures to ensure a robust study, which in turn expands the range of possible phase arrangements within the microstructure. Consequently, the mechanical properties of the material become increasingly dependent on these configurations. Furthermore, 3D FEA introduces additional computational complexity compared to its 2D counterpart. The computational requirements for simulating a single RVE are significantly higher, further emphasizing the depth and complexity of the current study. Despite these challenges, the

current study strictly follows a detailed 3D analysis, ensuring a more accurate representation of material behavior.

Creating datasets of microstructures is often a very labor-intensive task, therefore, a Python script was used to streamline and entirely automate the creation of the dataset. This approach effectively eliminated the challenges of manual creation and allowed for a more efficient research workflow. It is important to mention at this point that the spatial distribution of phases within the microstructure, as modeled by the DREAM.3D software, depends on a random stochastic process that is guided by a Gaussian random distribution. This feature essentially means that each instance of a microstructure results in a unique, random distribution of phases. This inherent randomness and the resulting implications for analysis are a fundamental aspect of the current study. However, in the present study, the random distribution of phases was not the primary focus of the investigation. Instead, the focus was on controlling the proportion of phases in each RVE. The proportion of the first phase, which was softer in nature, varied from 85% to a maximum of 100%, while the proportion of the second phase, a stronger material, varied from a minimum of 0% to a maximum of 15%. Thus, the main objective of this research was to systematically investigate the strengthening of a relatively weaker material by introducing a small proportion of a strong material.

Even though this research is predominantly academic in its nature, and the intent was not to replicate any particular real-world material, the insights gained from this study may be relevant to materials such as metal matrix composites (MMCs), as indicated in the work of Mortensen [94]. To ensure simplicity and clarity of the microstructure generation process, all other parameters remained constant during the study. Emphasis was placed on the effects of variation in phase fractions, hence allowing for a better understanding of this aspect within the larger microstructural landscape.

The study and characterization of microstructure in Dream.3D involves many different parameters, although the following description includes only a brief summary. The characterization of the grain size within the microstructure is mainly explained using the values attributed to the lognormal grain size distribution as well as the standard deviation of this lognormal distribution. For the present study, a value of 3 was chosen for the lognormal grain size distribution and a corresponding standard deviation of 0.25. The reader is referred to the study in reference [90] and DREAM.3D documentation. In an effort to maintain a minimum level of simplicity in the generation of the microstructure, the auxiliary parameters were kept constant throughout. The

above settings configured within the Dream.3D software resulted in the creation of hard phase particles in the range of 1 to 15 and a corresponding size range between 2 mm to 3 mm. The distribution of hard phase particles in the microstructure was of a stochastic nature.

Additional statistical properties of the hard phase were determined as follows: The mean value through both datasets was 0.067, while the standard deviation through both datasets was measured as 0.036. With respect to the crystal structure, both phases were identified as hexagonal close-packed. Any additional information regarding the preparation of this dual-phase material are described in detail in reference [90]. An example representation of a simulated microstructure can be found in Fig. 4.2. As a result of this process, the generation of the two datasets yielded a total of 2977 and 3474 distinct RVEs, respectively. The dataset with 2 977 RVEs will be used to predict temperature-dependent true stress-true strain curves while the dataset with 3 474 RVEs, on the other hand, is intended for the prediction of curves for temperature increase-strain curves.

Given the complexity of the topic at hand, it is important to emphasize that the present study is not primarily aimed at designing a precise mathematical representation of a particular real-world material. This approach is not uncommon in the field of such studies, as there is a lot of analogous studies that follow a similar methodology [60, 64, 65, 71]. A significant portion of these studies base their analyses and investigations on synthetic (i.e. artificial) microstructures that do not necessarily reflect the complex configurations of materials found in the real-world scenarios. Therefore, the primary focus of this study is to develop a reliable computational procedure that can handle existing microstructural configurations and provide insight into the behavior of diverse material systems, regardless of whether it is synthetic or derived from real-world material. To broaden the academic foundation of this research, it is important to emphasize that the microstructures synthesized solely for the objectives of the study can be compared to real material systems. Such a parallel can be drawn to metal matrix composites [94], where a greater portion of weaker base material is reinforced by a small portion of material with stronger mechanical properties. However, the versatility and broad applicability of the proposed computational method would essentially allow any microstructural configuration of a typical real-world material to be addressed without significant drawbacks.

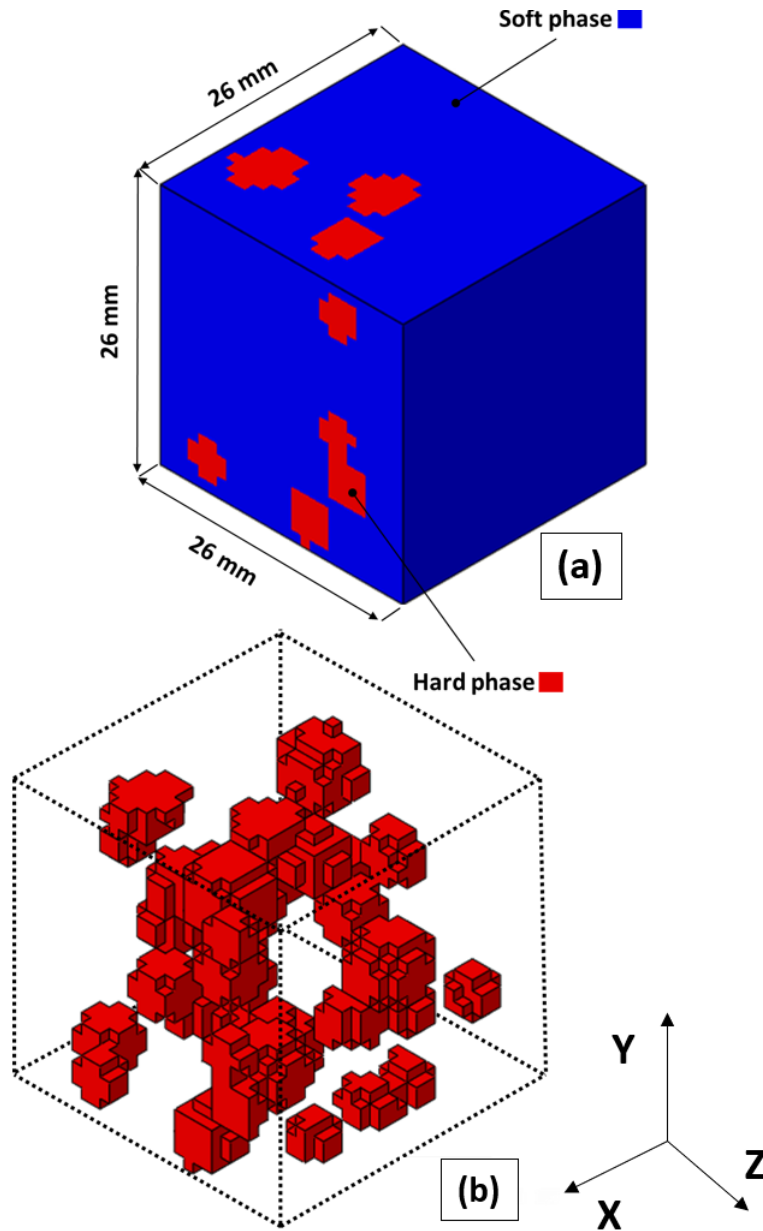


Figure 4.2: An example of unique RVE configuration: RVE size and a random microstructural configuration: (a) arrangement of the hard and soft phases (spatial distribution) within the RVE framework and (b) visualization of the arrangement of the hard phase within the RVE discarding the soft phase.

4.2 Dataset Generation

In an effort to investigate and understand the nature of both the temperature-dependent stress-strain curves and plastic deformation-induced heat generation, a consistent computational methodology has been utilised across these tasks. This methodological approach allows obtaining comparable and insightful data, enhancing the robustness of the present findings. The first step in the computational process involved the use of the Dream.3D software, an open-source microstruc-

ture generation software. In this software, a stochastic arrangement of the first and second phases was generated within an RVE explicitly defined by a dimension of $26 \times 26 \times 26$ voxels. Each voxel is $1 \times 1 \times 1$ mm, therefore, the dimensions of the RVE are $26 \times 26 \times 26$ mm. Following this microstructural simulation, these properties were transposed onto a corresponding finite element mesh sharing the same dimensions and size as the RVE. This alignment and correspondence between the finite element mesh and Dream.3D's RVE output ensures accurate and precise mapping of properties. This 1:1 correspondence is essential to the accuracy of subsequent calculations and simulations. As can be seen from Fig. 4.2, the resulting finite element mesh clearly illustrates the distribution of soft and hard phases as given by the Dream.3D output.

4.2.1 Material Properties and Constitutive Model

The first and second phases were assigned Young's modulus of 50 GPa and 500 GPa, respectively, indicating the different hard and soft phase stiffness. In addition, the Poisson's ratio of 0.33 was used for all materials considered in this study. To increase the simplicity of the analysis, the constancy of these constitutive properties was maintained – Young's modulus and Poisson's ratio – was kept constant across all temperature variations. To investigate the relationship between stress and strain under varying temperature conditions in more detail, the material properties affected by these temperature dependencies are visually represented through piecewise linear plots of true stress and true strain diagrams, as shown in Fig 4.3. Within the framework of this constitutive model, the effect of increasing temperatures is given special consideration. As a result the effects of increasing temperatures are evident in a consistent decrease in the tensile strength and yield strength values, i.e. material softening with the temperature increase.

As with comparable studies in the existing literature [60, 64, 65, 71], the RVE microstructural configuration as well as material properties employed in this study are generic by design. As already mentioned, the present study is not an attempt to simulate the real-world materials, but rather to provide a framework for understanding the fundamental interactions between microstructural configuration and material properties. However, it is worth noting that the properties of the softer phase are similar to those of an aluminum or magnesium alloy, while the properties of the harder phase could be compared to those of a ceramic-like material or a high-strength steel. This comparison emphasizes the potential of the present model to represent the mechanical properties of metal matrix composites, as the properties of the individual phases as well as the RVE microstructural configuration may belong to a similar cluster of such materials.

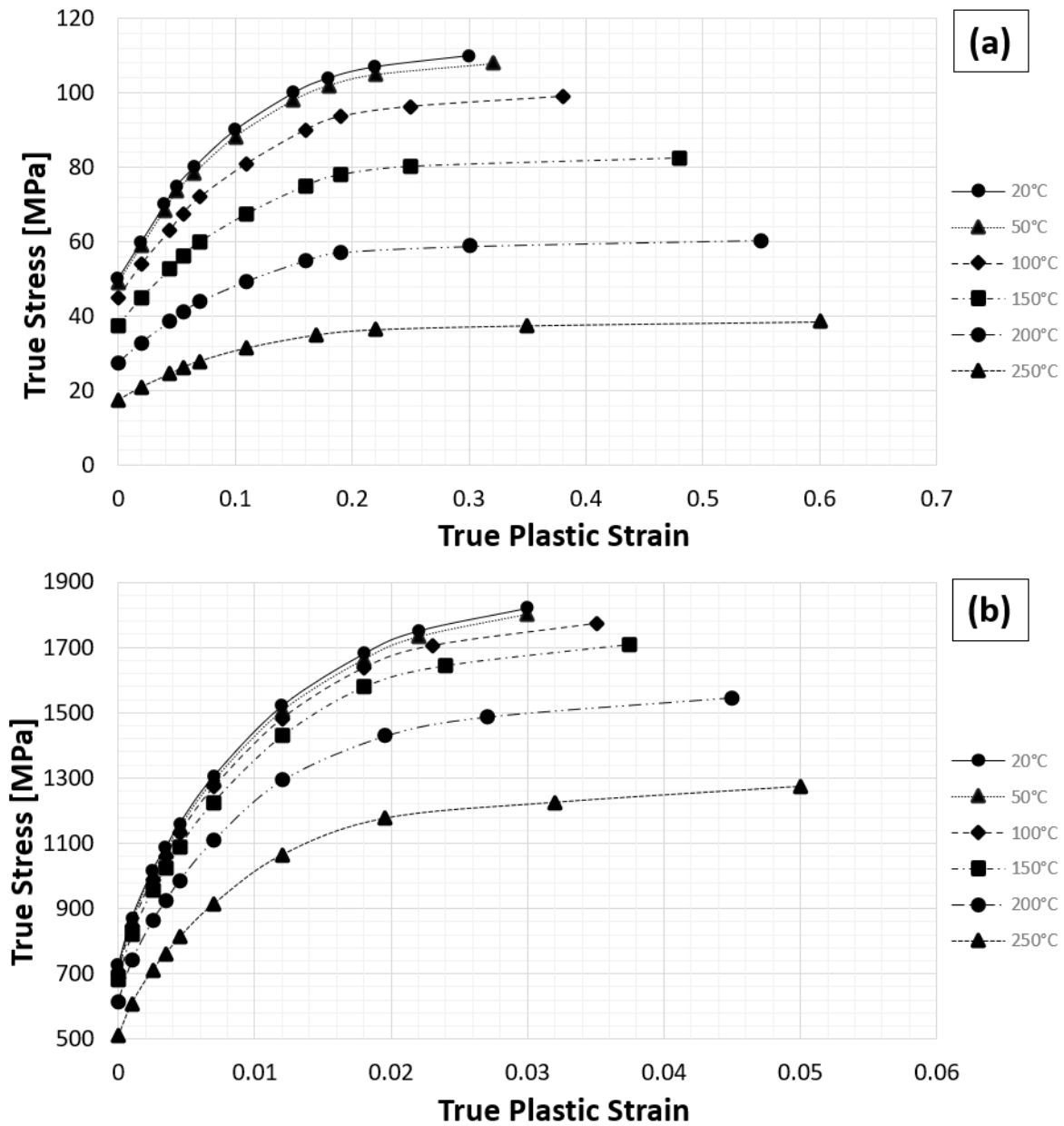


Figure 4.3: Representative mechanical properties and their variations based on the temperature-true stress and true plastic strain for (a) the soft phase and (b) the hard phase – stress-strain curves dataset. The symbols indicate the values used in the constitutive model.

In evaluating the phenomenon of deformation-induced heat generation, the material properties are again modeled as piecewise linear true stress-true strain curves, as shown in Fig. 4.4. While these properties exhibit similarities to the previous task, a key difference is that for deformation-induced heat generation the effect of temperature on these properties has been intentionally omitted. This simplification is supported by evidence suggesting that deformation-induced heat generation does not result in a significant increase in temperature (see Chapter 5), so the integrity of the data and their subsequent interpretation is not significantly affected. Other

than this exclusion, the remarks from the stress-strain dataset are still applicable to the material properties. In essence, the material studied remains consistent across both tasks, except for the elimination of the temperature-related effects in the current scenario.

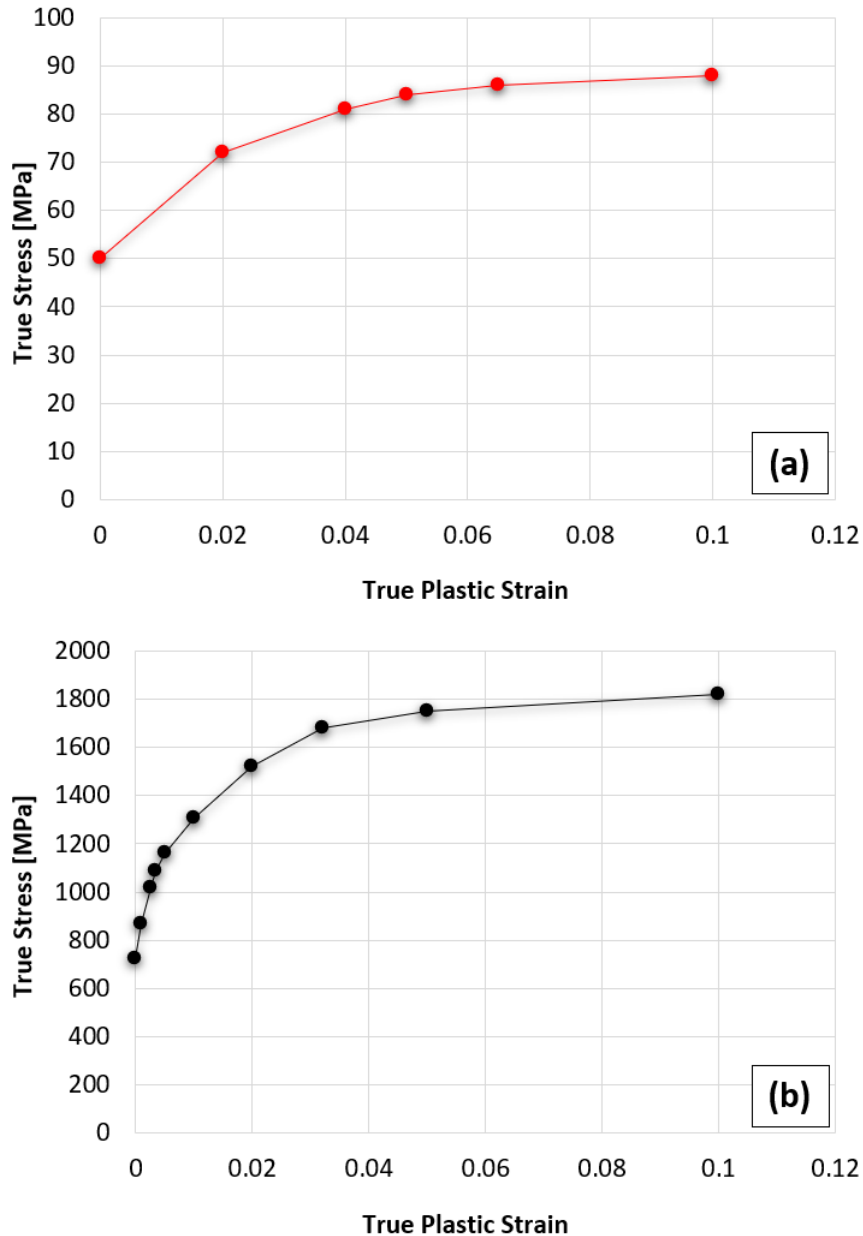


Figure 4.4: Representative mechanical properties – true stress and true plastic strain for (a) the soft phase and (b) the hard phase – deformation-induced heating (TQC) dataset. The dots indicate the values used in the software constitutive model.

s Therefore, the numerical procedure is also completely the same for both datasets except for this detail of temperature. The influence of temperature on the mechanical properties is not taken into account for the deformation-induced heating dataset. For the generation of both datasets, the numerical analysis of the RVEs is performed in the DSS Simulia Abaqus Standard

software version 2021. Isotropic yielding has been defined by the von Mises yield surface such that the value of the uniaxial yield stress is given as a function of the uniaxial equivalent plastic strain and temperature. This means that the constitutive model is specified as a set of points with the equivalent plastic strain, yield stress, and temperature as coordinates, which is illustrated in Figs 4.3 and 4.4. As mentioned earlier, the temperature effect is not considered for the deformation-induced heating dataset. The mesh is discretized using first-order hexahedral continuum incompatible modes C3D8I linear elements consisting of four integration points and eight nodes. These elements were selected from the Abaqus standard element library. The elements were chosen to overcome the locking issues associated with plasticity in metals while at the same time maintaining much better computational efficiency in contrast to second-order elements. Abaqus Standard software provides a variety of elements in its element library. However, the most commonly used hexahedral elements are C3D8I (incompatible modes), C3D8 (full integration), and C3D8R (reduced integration). It is important to note that elements such as C3D8 and C3D8R can suffer from so-called problems such as hourglassing, shear locking, and volumetric locking. This problem is especially pronounced in bending-dominant problems. Although this problem could be successfully solved by using second order elements, this would drastically increase computational efficiency. Therefore, the problem is solved by using C3D8I elements with incompatible modes to maintain computational efficiency. The connection of the hard and soft phases within the finite element mesh is done in such a way that adjacent elements shear neighboring nodes.

4.2.2 Numerical Simulation Procedure

Periodic Boundary Conditions

In this microscopic approach to modeling and simulating multiphase material, consisting of inclusions within a matrix, the concept of 3D Periodic boundary conditions (PBC) is employed according to [95]. To homogenize data from a 3D microstructure to a 3D meso or macrostructure under the periodicity assumption, appropriate 3D PBC must be utilized. The use of PBC necessitates two primary conditions: first, the geometric periodicity of the microstructure, and second, a very small and limited number of inclusions relative to the targeted macrostructure. PBCs are advantageous as they enable the simulation of an infinite material by repeating a finite representative volume element, thereby reducing computational costs. Moreover, PBC ensures that the simulated mechanical responses are more representative of the actual material behavior

by mitigating edge effects inherent in finite-sized models. Next, a short theoretical background of PBC is given.

Consider a periodic structure composed of an array of recurring unit cells subjected to macroscopic strain. The displacement field for this periodic structure can be represented as follows:

$$u_i(x_1, x_2, x_3) = \epsilon_{ij}^0 x_j + u'_i(x_1, x_2, x_3). \quad (4.1)$$

In the equation above, ϵ_{ij}^0 denotes the macroscopic strain tensor of the periodic structure. The first term on the right-hand side, $u^0 = \epsilon_{ij}^0 x_j$, represents a linear displacement field (i.e., in the case where the structure is homogeneous). The second term, $u'_i(x_1, x_2, x_3)$, is the periodic function that accounts for modifications to the linear displacement field resulting from the heterogeneous composition of the structure (i.e., considering multiphase material which is not homogeneous). Since the periodic array of unit cells forms a continuous physical body, two continuity conditions must be satisfied at the boundaries of neighboring unit cells. First, the displacements must be continuous; hence, adjacent unit cells cannot detach or interpenetrate at their boundaries post-deformation. Second, the traction distributions must remain consistent across the parallel boundaries of the unit cells. To maintain the continuity of the physical body, the BC of a unit cell must match. Thus, each unit cell integrates seamlessly into the continuous structure. The displacement field assumption from Eq. (4.1) does not directly apply to the boundaries due to the unknown periodic component $u'_i(x_1, x_2, x_3)$. For any given unit cell, boundary surfaces form parallel pairs, with displacements on these surfaces expressed as:

$$u_i^{k+} = \epsilon_{ij}^0 x_j^{k+} + u'_i, \quad (4.2)$$

$$u_i^{k-} = \epsilon_{ij}^0 x_j^{k-} + u'_i. \quad (4.3)$$

Here, k^+ and k^- denote the k -th pair of opposite parallel boundary surfaces of a unit cell. Given the periodic nature, $u'_i(x_1, x_2, x_3)$ remains constant across these parallel boundaries. For this periodic model to work, the displacements at the boundaries of each unit cell must match up with the displacements of the neighboring cells. This ensures no gaps or overlaps occur, maintaining a continuous deformation throughout the material. Consequently, the difference between the displacements at these boundaries is:

$$u_i^{k+} - u_i^{k-} = \epsilon_{ij}^0 (x_j^{k+} - x_j^{k-}) = \epsilon_{ij}^0 \Delta x_j^k. \quad (4.4)$$

Since Δx_j^k are constants for each pair of parallel boundary surfaces, and given a specified ϵ_{ij}^0 , the right-hand side becomes a constant. This formulation simplifies the application of these equations as nodal displacement constraints in FEA. Fig. 4.5 illustrates a schematic representation of a 2D unit cell under macro strain with PBC.

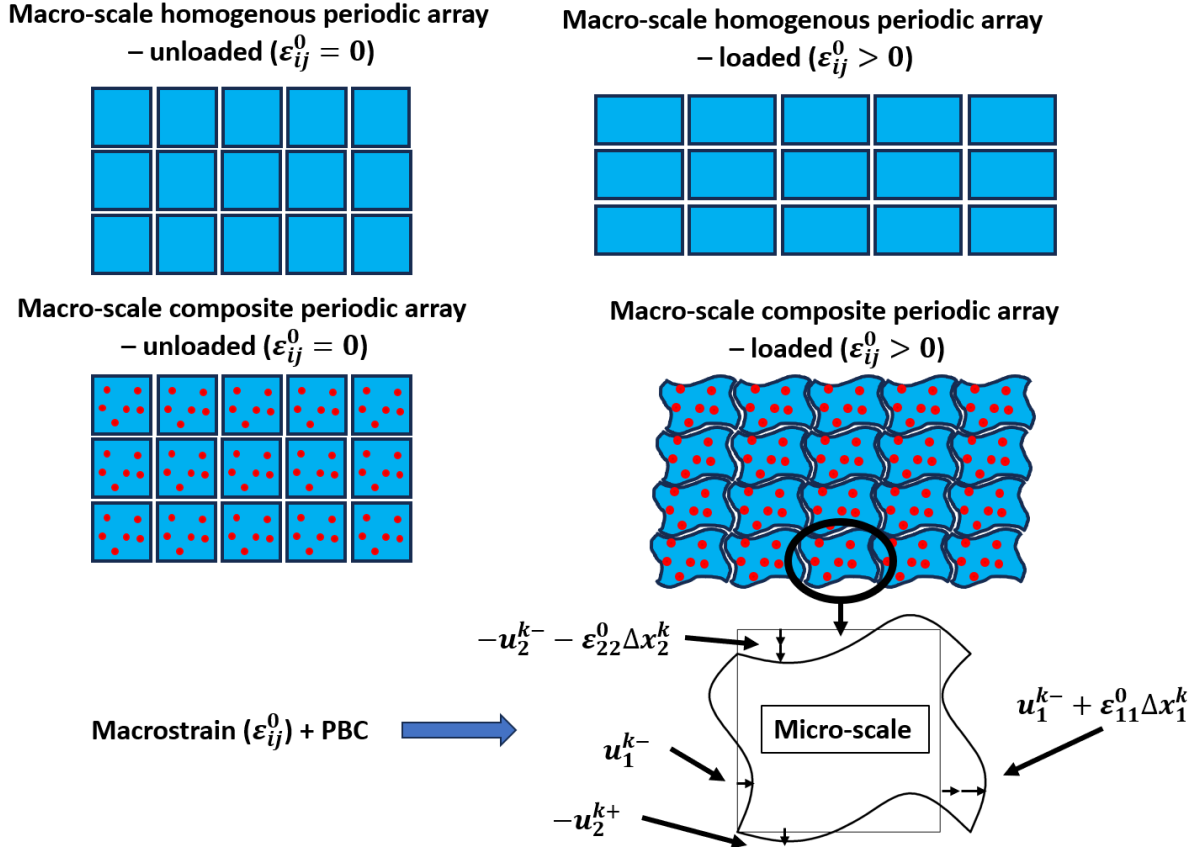


Figure 4.5: Illustration of a 2D unit cell under macro strain with PBC [95].

Eq. (4.4) represents a specific type of displacement BC. Rather than specifying known boundary displacements, it defines the displacement differences between opposing boundaries. This approach ensures the continuity of the displacement field. However, displacement-difference BC, as given in Eqs. (4.2), (4.3) and (4.4), may not be entirely comprehensive and may fail to ensure the continuity of traction. The conditions for traction continuity are expressed as follows:

$$\mathbf{t}^+ - \mathbf{t}^- = 0, \quad \text{where } \mathbf{t} = \boldsymbol{\sigma} \mathbf{n}. \quad (4.5)$$

The terms \mathbf{t}^- and \mathbf{t}^+ represent the tractions at the corresponding parallel boundary surfaces,

respectively. Fig. 4.6 displays a graphical representation of the traction continuity condition of a unit cell.

For general periodic boundary value problems, Equations (4.4) and (4.5) provide a set of BC, excluding rigid body motion. In the illustrative examples presented in Fig. 4.5, when analyzing a unit cell using a displacement-based finite element method, the application of Eq. (4.4) alone ensures the uniqueness of the solution, thereby automatically satisfying Eq. (4.5). Consequently, it is not necessary to explicitly apply the latter BC in the analysis.

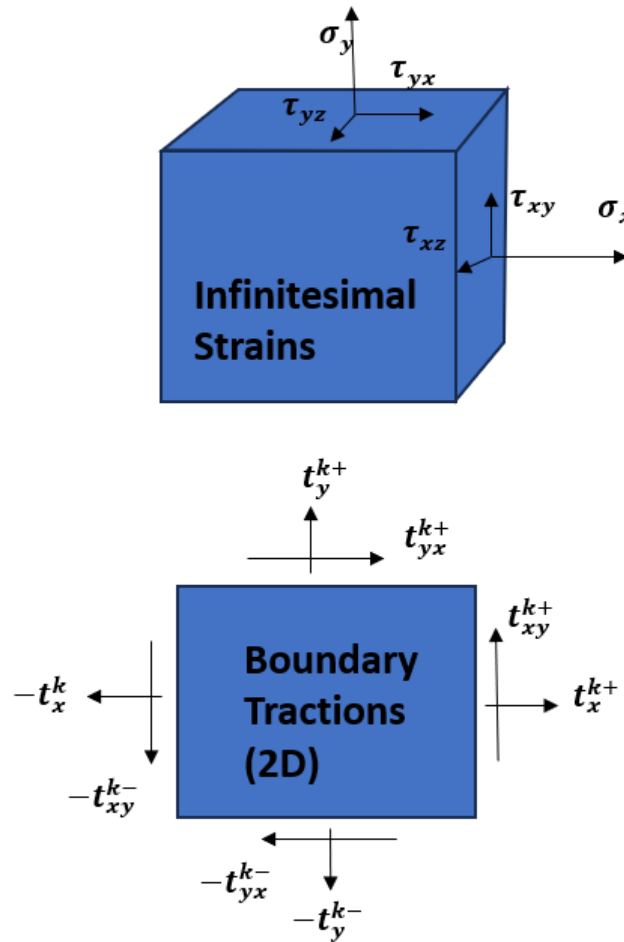


Figure 4.6: Traction continuity condition on the boundary cell [95].

A detailed description of the procedure for applying PBC is provided in [95], where the numerical implementation on a 3D scale using Abaqus software is explained in detail.

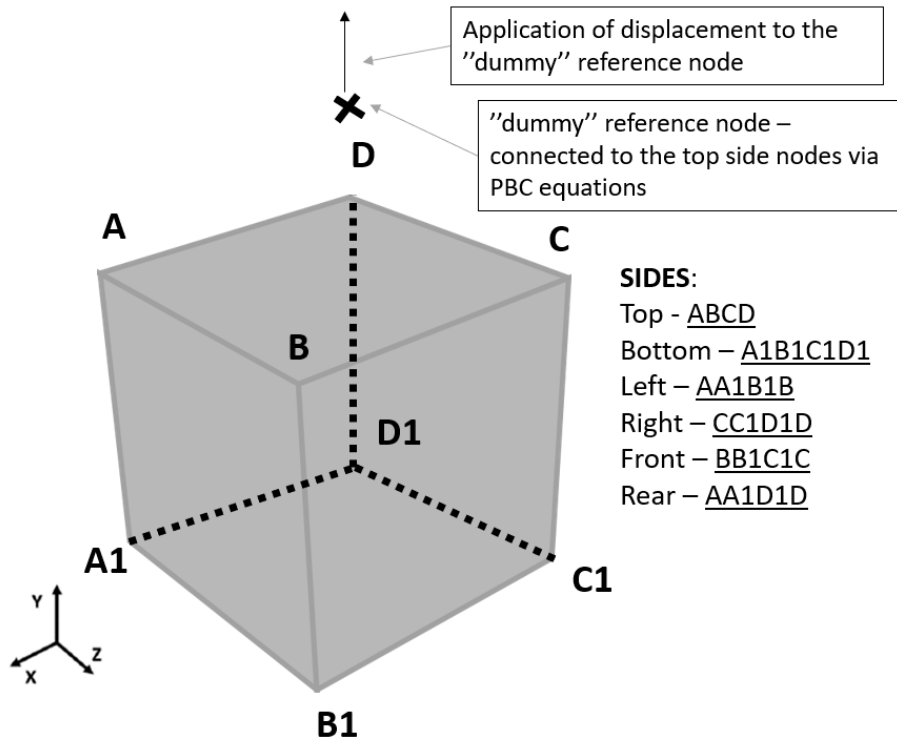
Simulation Procedure and Constitutive Model

Regarding the numerical procedure, all numerical simulations are computed in the same way using 20 evenly spaced time increments. PBC were applied to the RVE according to the pro-

cedures described in [95–97] as already explained in the previous subsection. Displacement loading was used and it was applied to the reference node in the Y direction. It should be noted that this reference node is connected to each boundary node on the adjacent side of the RVE and that the boundary nodes are connected to each other by equation constraints in Abaqus. The loading was applied in the form of a strain magnitude of 0.57% as a displacement loading. The application of loading and PBC are displayed in Fig 4.7. Thus, the BC represents the stress-strain state of the material as in uniaxial tensile loading. A fixed time increment, in contrast with an automatic time increment, is used to ensure that the outputs of all analyses are, equally spaced and synchronized. This could later simplify using the ML model which requires a consistent input.

Uncoupled thermomechanical analysis method (static general step) was used, while for stress-strain dataset, the information on temperature was obtained in the form of the predefined temperature field used in Abaqus. Moreover, for the dataset used to determine the temperature increase during plastic deformation, the temperature effect was excluded from the simulation and it was assumed that the simulations were performed at 20 °C. Therefore, that analysis was solved with a constant temperature assuming heat generated from displacement is small enough to not influence mechanical properties. All analyses were calculated using an implicit Abaqus Standard solver, and the average calculation time per simulation was about 15 minutes. It should be noted that higher temperatures were associated with a lower slope of the true stress-true strain curves, which made it more difficult to achieve convergence. Therefore, higher temperatures were associated with longer simulation runs. Thus, the simulation time for room temperatures was shorter than average, about 7 minutes, while the simulation time for the highest temperatures (stress-strain dataset) was actually increased to 32 minutes.

Even though the simulation time was mostly associated with the temperature, the RVE arrangement also affected it a little, but this was of minor importance. Furthermore, this problem could be solved by automatic time incrementing in Abaqus, however, this is avoided to keep the input to the ML model constant. This problem could also be overcome by decreasing the default convergence criteria of Abaqus [98], but this is also avoided as it could affect the accuracy of the results. Therefore, the default implicit solver criteria were used. The creation of the two datasets in this study was achieved through a process of FEA that took nearly 980 hours. Using a personal desktop computer equipped with an Intel®Core™ I7-4970 CPU, each simulation was solved using a single processor core.

**Application of PBC:**

RVE sides are interconnected via PBC equations (opposite node to node):
 Top side to bottom, left to right and rear to front. Nodes on the edges and ends of the cube are also interconnected according to the procedure in [95]

Figure 4.7: Simplified visualization – application of PBC to the RVE [95].

This study was conducted under the constraint of computational cost, which necessitated a conservative approach to applied load in the form of strain. During the development phase of the method, tests were conducted at various strain levels, but the increase in strain resulted in convergence problems, that posed a considerable challenge to the progress of the research. Attempts were made to mitigate these convergence issues by employing a smaller time increment. While this approach resulted in improved convergence, it also had a significant drawback: a substantial increase in computational cost. This substantial increase is largely related to the principle of computational physics, where reducing the time increment potentially improves convergence and accuracy, but leads to a corresponding increase in computational cost.

Another possible strategy to resolve the convergence problem was to introduce automatic time incrementation. However, to maintain consistent input to the ML model (e.g., equally spaced output of the analysis), this solution was not considered. This constant input is crucial to control variability and limit possible biases in the model. Under the conditions of extended simulation time and the need for a smaller time incrementation, the selection was made for an optimal load magnitude. Accordingly, a total simulation time of slightly more than one month

was determined as the maximum reasonable limit. Any attempt to go beyond this threshold would result in excessive demands on computational resources and exceed the acceptable time frame.

An alternative technique considered was the use of an explicit solver capable of solving the convergence issues. However, this method presented a number of problems, most notably a significant increase in computational cost, resulting in individual simulation times of over an hour. This added complexity further complicated the delicate balance between available computational resources and the requirements. Given the constraints of available computational resources, it was unfeasible to deepen the problem at higher strain magnitudes while maintaining a reasonable simulation time. This trilemma of computational cost, convergence issues, and simulation time required a careful approach that would ensure the generation of reliable and reproducible results without exceeding the computational budget. Therefore, the strain magnitude of 0.57% was chosen.

Furthermore, despite the lack of empirical experimental data, the numerical simulation results were considered an accurate representation of the material's behavior. This assumption finds justification in the wealth of previous work that has shown reliable comparisons between FEA and experimental tests, as outlined in Chapter 2. However, it is important to interpret the results within the limitations of this approach, and to be aware of the approximations and assumptions underlying the numerical simulations.

To create the dataset for determining the true stress-true strain curves, analyzes were calculated at six different temperatures: 20 °C, 50 °C, 100 °C, 150 °C, 200 °C, and 250 °C. An initial number of 500 simulations were performed for each temperature level, but not all of them achieved a convergent solution within the specified number of fixed time increments. The simulations that achieved convergence and whose results were used in the present study are listed in Table 4.1. Thus, as can be seen from the table, in the end, 2977 different simulations were considered for training the ML model. This size of the dataset as well as the size of the RVE can be compared with similar studies involving 3D scale [60–62]. Different arrangements of the microstructures are shown in Fig 4.8 considering a random RVE for each temperature level. An attempt was made to choose a variety of microstructures to visualize RVEs involving various proportions of the hard and soft phases. This allows the reader to get an idea of how randomly generated microstructures with a lower and a higher fraction of the hard phase look like. In addition, for each RVE in the figure, the simulation results are shown in terms of true von Mises

Table 4.1: Number of simulations performed for different temperature levels.

Temperature	No. of sim.
20 °C	496
50 °C	496
100 °C	495
150 °C	497
200 °C	499
250 °C	494

stress, total displacement, and true equivalent plastic strain for the last simulation increment in Figs. 4.9, 4.10, 4.11, 4.12. In all figures, a deformation scale of $25\times$ is used to better visualize the deformed state of the RVE.

The plastic deformation of the RVE is described by a "PEEQ" output in Abaqus and corresponds to the true equivalent plastic strain (see [98]). It can be seen that lower average stress values are associated with higher temperature levels as well as a lower fraction of the hard phase. This is logical because assigned material properties generally degrade at higher temperatures, whereas the hard phase consists of a significantly stronger material than soft phase. On the other hand, a higher variance of displacement within the RVE is associated only with a higher fraction of hard phase. This also makes sense since the difference in yield strength and stiffness between soft and hard phase is about $10\times$ which makes the variance so strong. In addition, a higher value of equivalent plastic strain is also associated with a higher fraction of hard phase. It should be noted that almost all of the equivalent plastic strain is induced in the soft phase, which makes sense since the soft phase is associated with lower yield curves.

To establish understanding of the heat generation caused by plastic deformation, the second dataset was created and a methodology similar to that used in the formulation of the first dataset has been employed. Similar material properties are again assigned to hard and soft phase, Fig. 4.4. However, the effects of temperature fluctuations were not accounted for during the simulation of this secondary dataset and it was considered that temperature is fixed at 20 °C. The temperature increase is rather small (see Chapter 5), therefore, the temperature dependency of material properties for the secondary dataset are neglected. To visualize the phenomenon in question, three additional RVEs were shown. These RVEs have different phase fractions. The microstructure patterns of these additional RVEs are illustrated in Fig. 4.13.

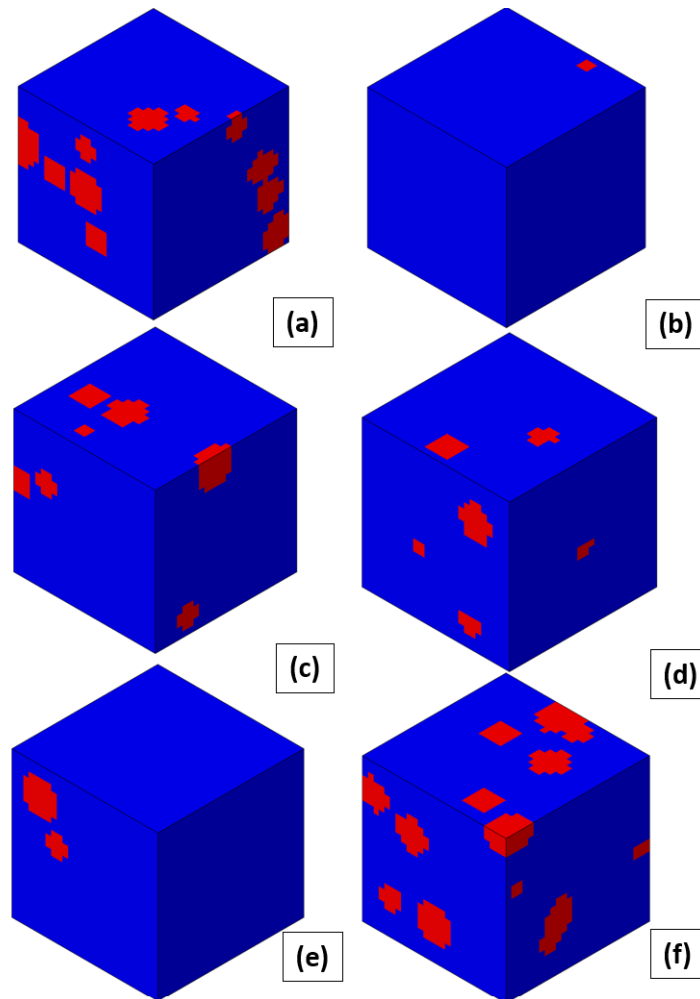


Figure 4.8: A random microstructure configuration of phases for an RVE including all six temperature levels and different fractions of phases (i.e., higher and lower phases fraction): (a) Temp = 20 °C hard ph. frct. = 0.143, (b) Temp = 50 °C hard ph. frct. = 0.008, (c) Temp = 100 °C hard ph. frct. = 0.078, (d) Temp = 150 °C hard ph. frct. = 0.072, (e) Temp = 200 °C hard ph. frct. = 0.038, (f) Temp = 250 °C hard ph. frct. = 0.110.

To facilitate consistency and comparison with the initial dataset, the true von Mises stress, total displacement, and true equivalent plastic strain for these new RVEs are also visualized in Figs. 4.14, 4.15, 4.16, and 4.17. To ensure clear visualization, the deformation scale remains consistent with the $\times 25$ scale as used in the previous figures. In addition, for this particular dataset, a section of each RVE has been intentionally removed to visualize microstructural areas inside the RVEs. The observations derived from this dataset appear to be consistent with those from the previous dataset.

For the stress-strain curves dataset, the true stress-true strain of the RVE was observed for the given BC and loading. The average (mean) value of the true stress-true strain response over all integration points of the RVE was used:

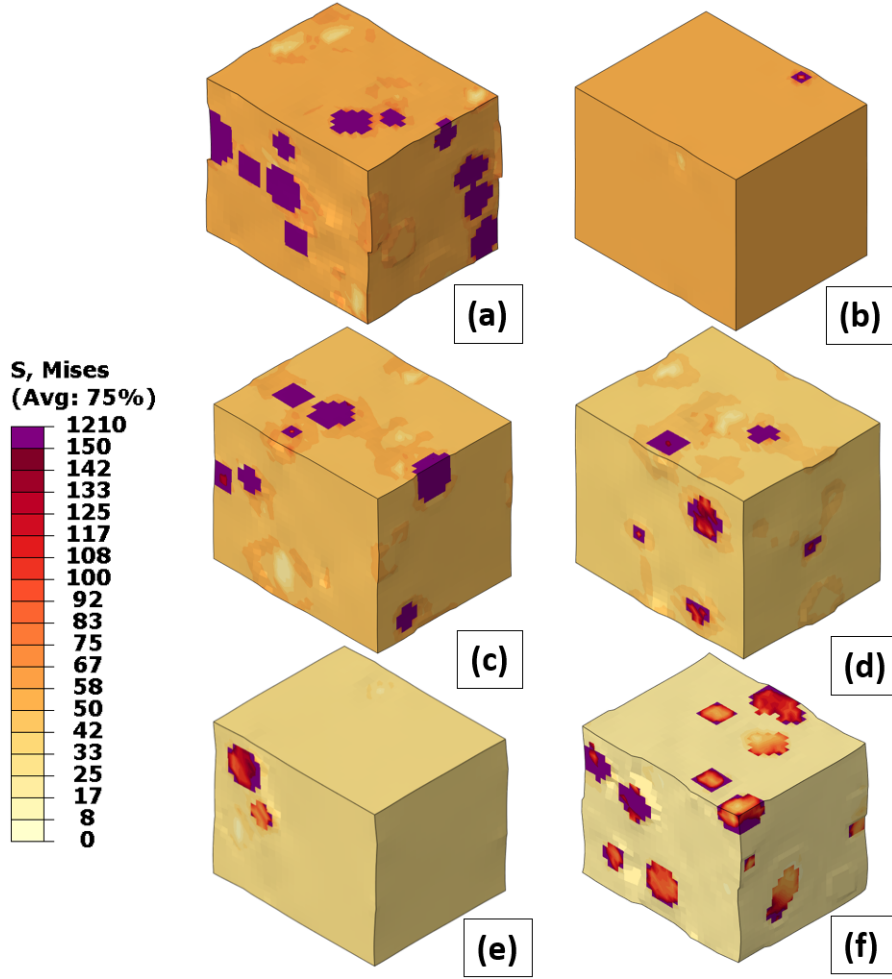


Figure 4.9: Von Mises stress (MPa) at the final simulation increment for the analyzed RVEs shown in Fig 4.8: (a) Temp = 20 °C hard ph. frct. = 0.143, (b) Temp = 50 °C hard ph. frct. = 0.008, (c) Temp = 100 °C hard ph. frct. = 0.078, (d) Temp = 150 °C hard ph. frct. = 0.072, (e) Temp = 200 °C hard ph. frct. = 0.038, (f) Temp = 250 °C hard ph. frct. = 0.110.

$$\sigma_{\text{avg}} = \frac{1}{V} \int_V \sigma(\mathbf{x}) dV, \quad (4.6)$$

where $\sigma(\mathbf{x})$ is the stress at a point \mathbf{x} in the domain, V is the total volume (or area in 2D) of the mesh, and dV is the differential volume element. The corresponding value of stress and strain were captured on each simulation increment. Therefore, the mean response of the true stress-true strain of the RVE was obtained from 20 uniformly spaced increments. The term engineering stress refers to the stress calculated on the original cross-sectional area. During tensile loading, contraction (tearing/necking effects) of the cross-section is not taken into account. However, true stress (i.e., Cauchy stress) is used throughout this study. The true stress, on the other hand is calculated based on the actual cross section of the uniaxial tensile specimen and the contraction

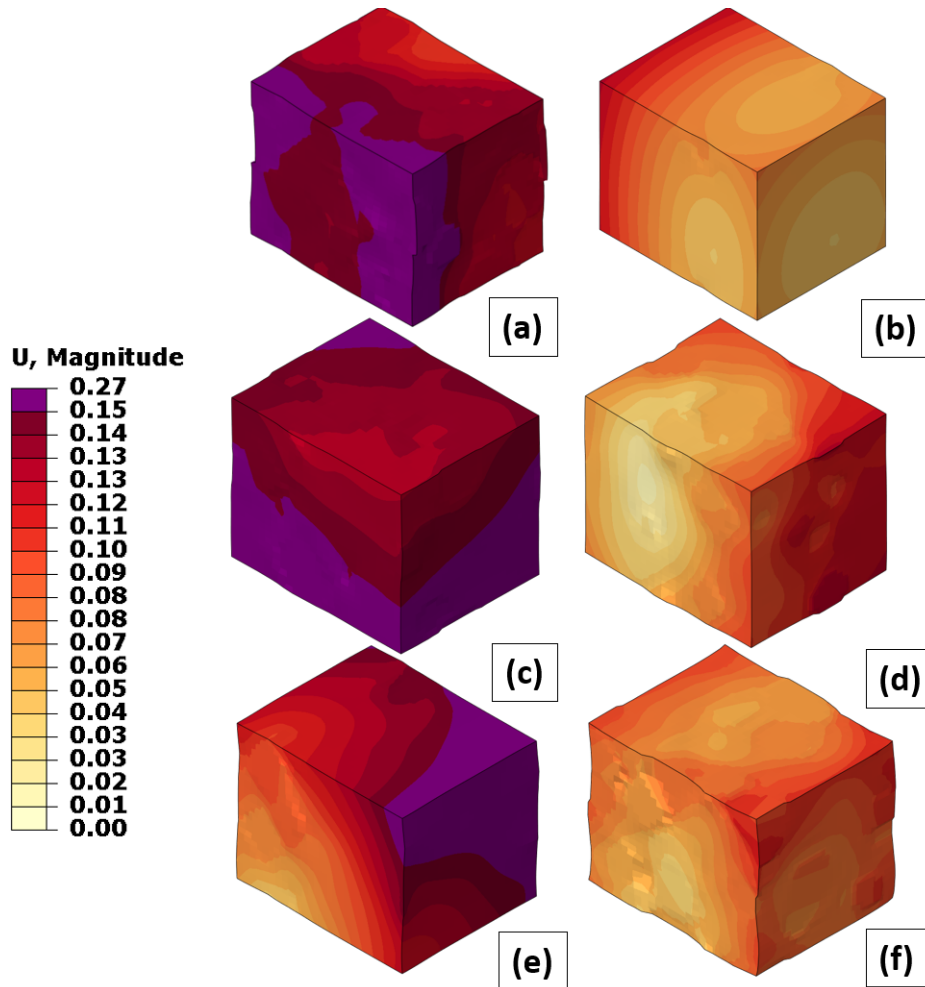


Figure 4.10: Total displacement (mm) at the final simulation increment for the analyzed RVEs shown in Fig 4.8: (a) Temp = 20 °C hard ph. frct. = 0.143, (b) Temp = 50 °C hard ph. frct. = 0.008, (c) Temp = 100 °C hard ph. frct. = 0.078, (d) Temp = 150 °C hard ph. frct. = 0.072, (e) Temp = 200 °C hard ph. frct. = 0.038, (f) Temp = 250 °C hard ph. frct. = 0.110.

during tensile loading is taken into account. For better understanding, a response of the RVE in Fig. 4.2 is visualized in Fig. 4.18. This response corresponds to the temperature of 20 °C. The von Mises stress was used for the equivalent stress, while the strain output corresponds to the strain increment applied during loading. Therefore, the plotted true stress-true strain curve corresponds to the true stress-true strain curve obtained from the macroscopic experimental uniaxial tensile test. In Fig. 4.18, the yield strength is easily noticed. It corresponds to the point where the curve slope begins to change its shape from linear to nonlinear. For a larger number of responses including different temperatures and phase fractions, reader is referred to Chapter 5.

In addition, a mesh sensitivity study is presented to investigate stress convergence with mesh size, even though very similar studies [60–62] could be found considering comparable mesh sizes involving 3D scale on this topic. A random RVE configuration was created to which dif-

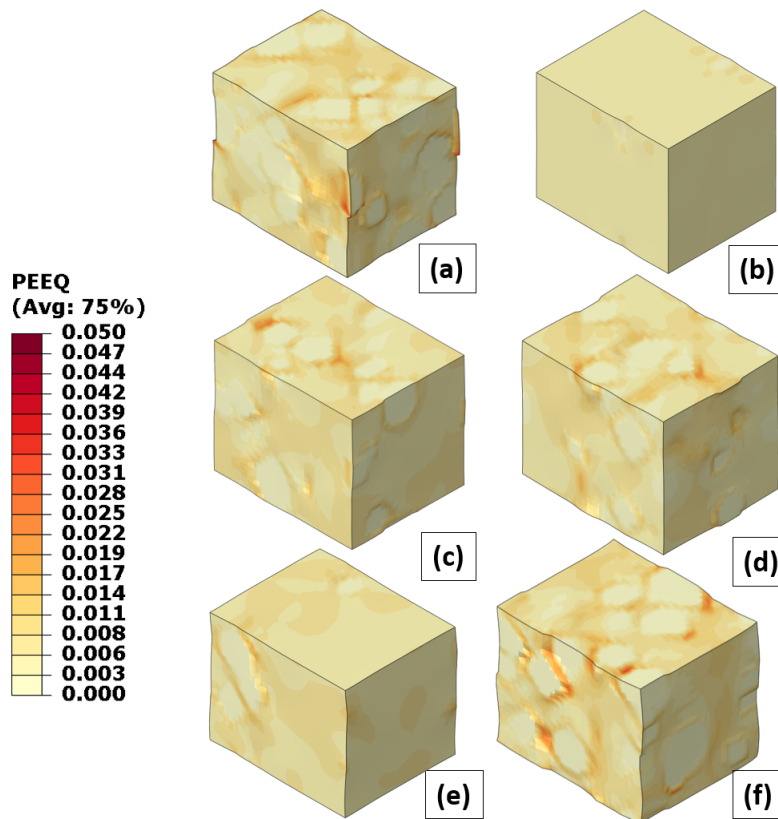


Figure 4.11: Equivalent plastic strain at the last simulation increment for the analyzed RVEs shown in Fig 4.8: (a) Temp = 20 °C hard ph. frct. = 0.143, (b) Temp = 50 °C hard ph. frct. = 0.008, (c) Temp = 100 °C hard ph. frct. = 0.078, (d) Temp = 150 °C hard ph. frct. = 0.072, (e) Temp = 200 °C hard ph. frct. = 0.038, (f) Temp = 250 °C hard ph. frct. = 0.110.

ferent mesh densities were applied. For this study, only the von Mises stress was averaged through the RVE using the procedure explained previously, however, it was averaged through each phase apart. Stress convergence is only checked for 6 different sizes of the mesh densities considering sizes of $10 \times 10 \times 10$, $20 \times 20 \times 20$, $26 \times 26 \times 26$, $30 \times 30 \times 30$, $40 \times 40 \times 40$, and $50 \times 50 \times 50$ finite elements. Convergence of the values of equivalent plastic strain as well as the values of deformation were not investigated in this study. The obtained results for all mesh densities can be visualized in Table 4.2 and Fig. 4.19. The maximum difference in von Mises stress value is less than 6 MPa when both phases are considered. Therefore, the influence of stress concentration can be neglected in this study. Moreover, it was found that convergence for both phases is achieved at a mesh density of $26 \times 26 \times 26$ finite elements. Finally, computational time as well as software (DREAM.3D to Abaqus) compatibility were considered in deciding the mesh size, thus the density of $26 \times 26 \times 26$ was chosen.

Finally, the following section explains how the amount of heat generated during deformation

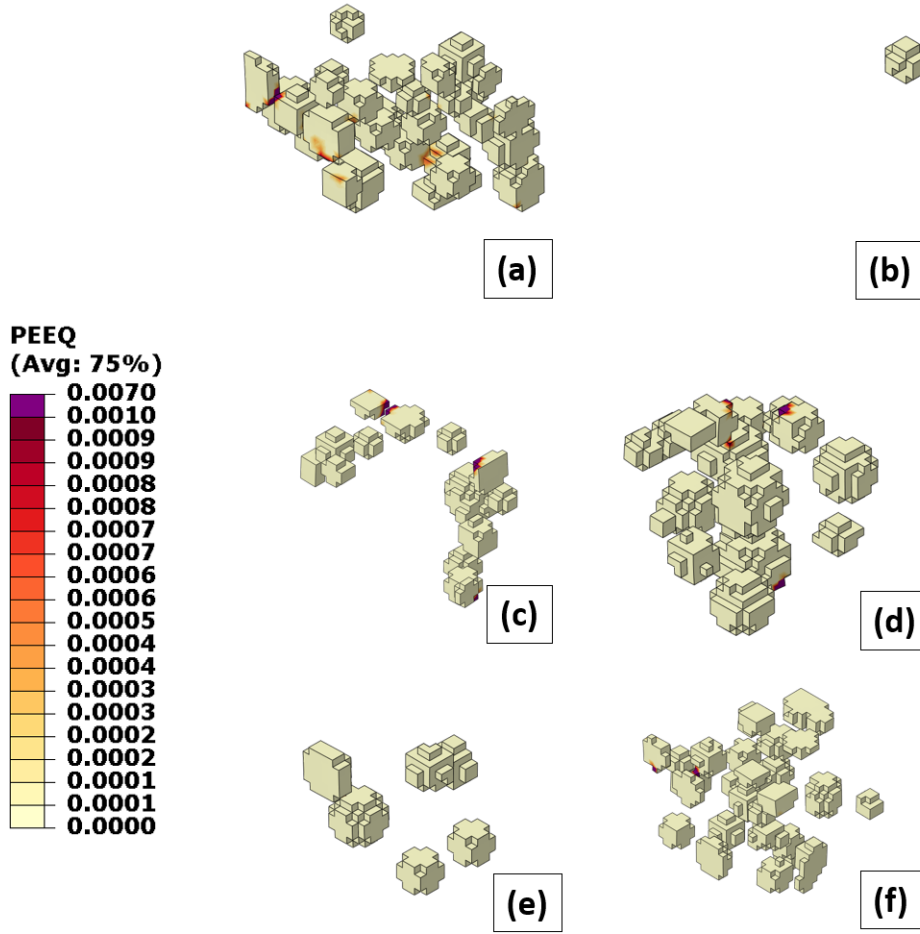


Figure 4.12: Equivalent plastic strain at the last simulation increment for the analyzed RVEs shown in Fig 4.8 (i.e., only the hard phase is shown): (a) Temp = 20 °C hard ph. frct. = 0.143, (b) Temp = 50 °C hard ph. frct. = 0.008, (c) Temp = 100 °C hard ph. frct. = 0.078, (d) Temp = 150 °C hard ph. frct. = 0.072, (e) Temp = 200 °C hard ph. frct. = 0.038, (f) Temp = 250 °C hard ph. frct. = 0.110.

of the RVE was determined. This applies only to the dataset used to determine the deformation-induced heat generation. Thus, while the total amount of plastic deformation is a known variable, the amount of plastic energy can be easily calculated. In either case, the amount of energy is reported in the output of the Abaqus software (see [98]). In addition, the increase in temperature within the RVE during deformation can be calculated using the following equation [87]:

$$\Delta T = \frac{Q\beta}{\rho V c_p}, \quad (4.7)$$

where ΔT is the temperature increase in [K], Q is the total plastic energy of the RVE in [J], β is the TQC, ρ is the mass density in [$\frac{\text{kg}}{\text{m}^3}$], V is the volume of the RVE in [m^3] and c_p is the specific heat capacity at a constant pressure in [$\frac{\text{J}}{\text{kg}\cdot\text{K}}$]. The amount of heat generated and the

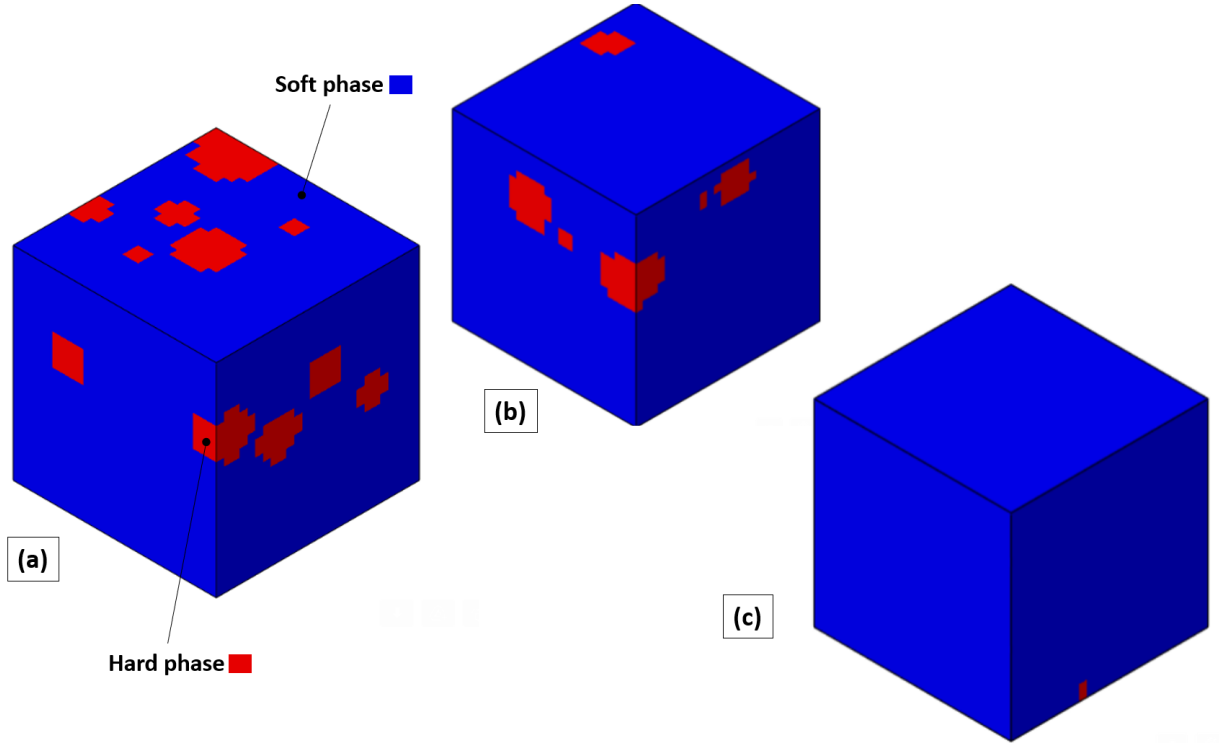


Figure 4.13: A random microstructure configuration of phases for three different RVEs including lower and higher phase fractions: (a) RVE 1: Hard phase fraction = 0.143, (b) RVE 2: Hard phase fraction = 0.082, (c) RVE 3: Hard phase fraction = 0.014.

temperature increase is an average amount through the entire RVE. The equation only applies to the adiabatic conditions. Adiabatic heating conditions generally correspond to higher strain rates because the heat convection and heat conduction do not have enough time to take place in that case. For simplicity, this assumption is adopted for this research. It was therefore assumed that heat generation is uniform through the RVE. The volume of the RVE was obtained from its dimensions, which correspond to $26 \times 26 \times 26$ mm and the volume is $V = 1.7576 \cdot 10^{-5} \text{ m}^3$. As mentioned above, the plastic deformation value information was obtained from the Abaqus output. The mass density and specific heat capacity were both held constant for the dataset and expressed as: $c_p = 500 \frac{\text{J}}{\text{kg}\cdot\text{K}}$ and $\rho = 2500 \frac{\text{kg}}{\text{m}^3}$. For simplicity, equal c_p and ρ were assigned to both of the phases. However, it should not be a major problem to perform similar studies given different c_p and ρ properties for the soft and hard phases. In addition, the TQC was modeled to depend on the value of strain, ranging from 0.7 to 0.886 for each RVE in the dataset. This type of value is common for engineering materials such as metals. The TQC β is designed to change based on the strain level experienced by each RVE in the dataset:

$$\beta = \beta_1(18.86\epsilon + 1). \quad (4.8)$$

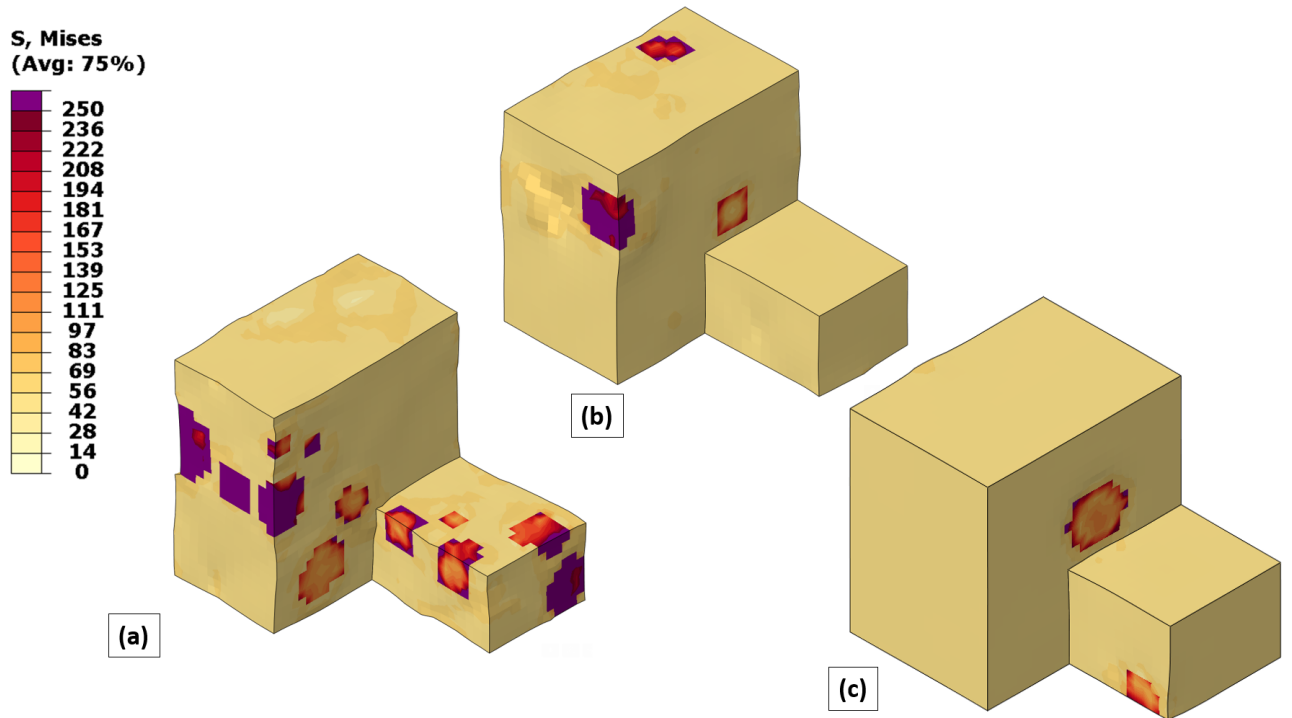


Figure 4.14: Von Mises stress (MPa) at the final simulation increment for the analyzed RVEs shown in Fig 4.14 (i.e., a section of each RVE has been intentionally removed for better visualization): (a) RVE 1, (b) RVE 2, (c) RVE 3.

In each RVE, the parameter β_1 is randomly assigned a value between 0.7 and 0.8. For states of both zero strain and maximum tensile strain (0.57%), when aligned with the controlled displacement, β values have been observed ranging from 0.7 to 0.886. Importantly, Eq. (4.8) is not designed to precisely simulate the true progression of the TQC but is instead formulated to enhance the complexity of the heat generation process while ensuring that the TQC remains within plausible boundaries for commonly used construction materials. Following the presented procedure, the TQC value is a known variable, in contrast with many other research papers where the TQC value is the object of interest. In addition, the plastic deformation induced heating RVE responses were not investigated in this Chapter in contrast with stress-strain responses (e.g., Fig. 4.18), therefore, to investigate the temperature increase-strain curves responses, see Chapter 5.

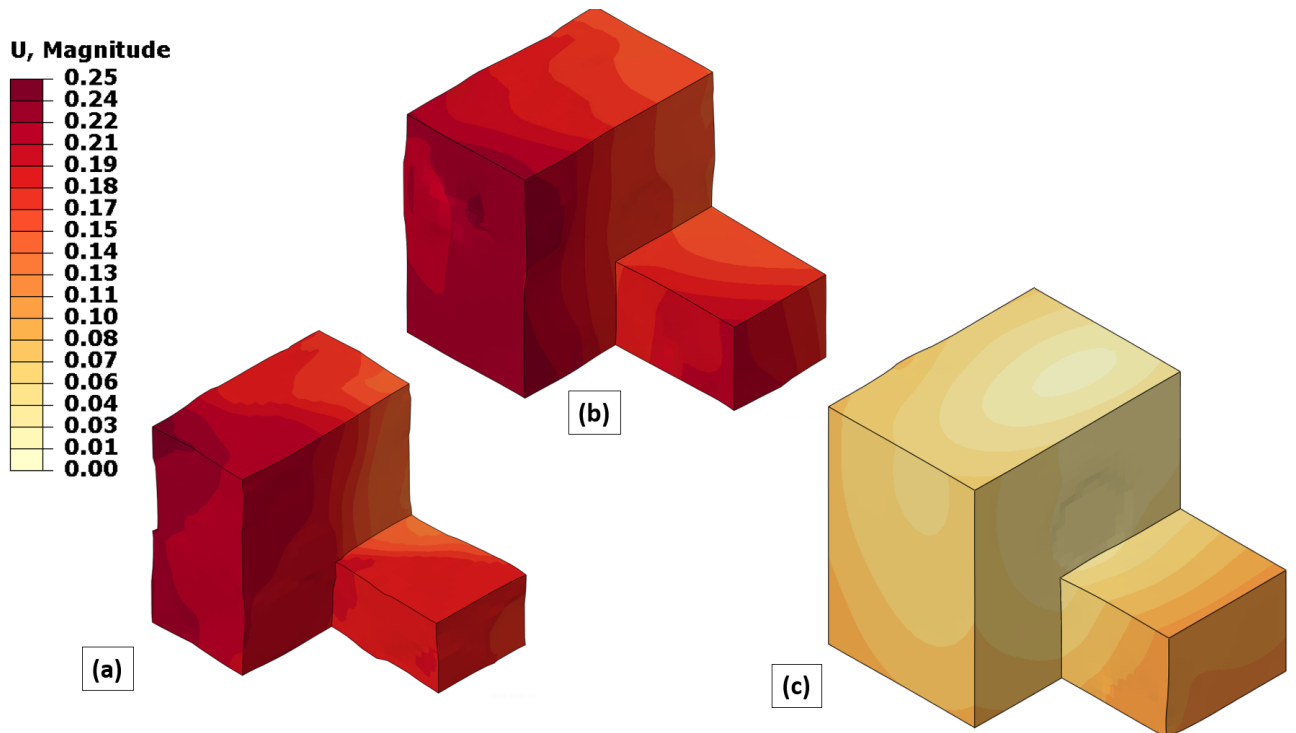


Figure 4.15: Total displacement (mm) at the final simulation increment for the analyzed RVEs shown in Fig 4.15 (i.e., a section of each RVE has been intentionally removed for better visualization): (a) RVE 1, (b) RVE 2, (c) RVE 3.

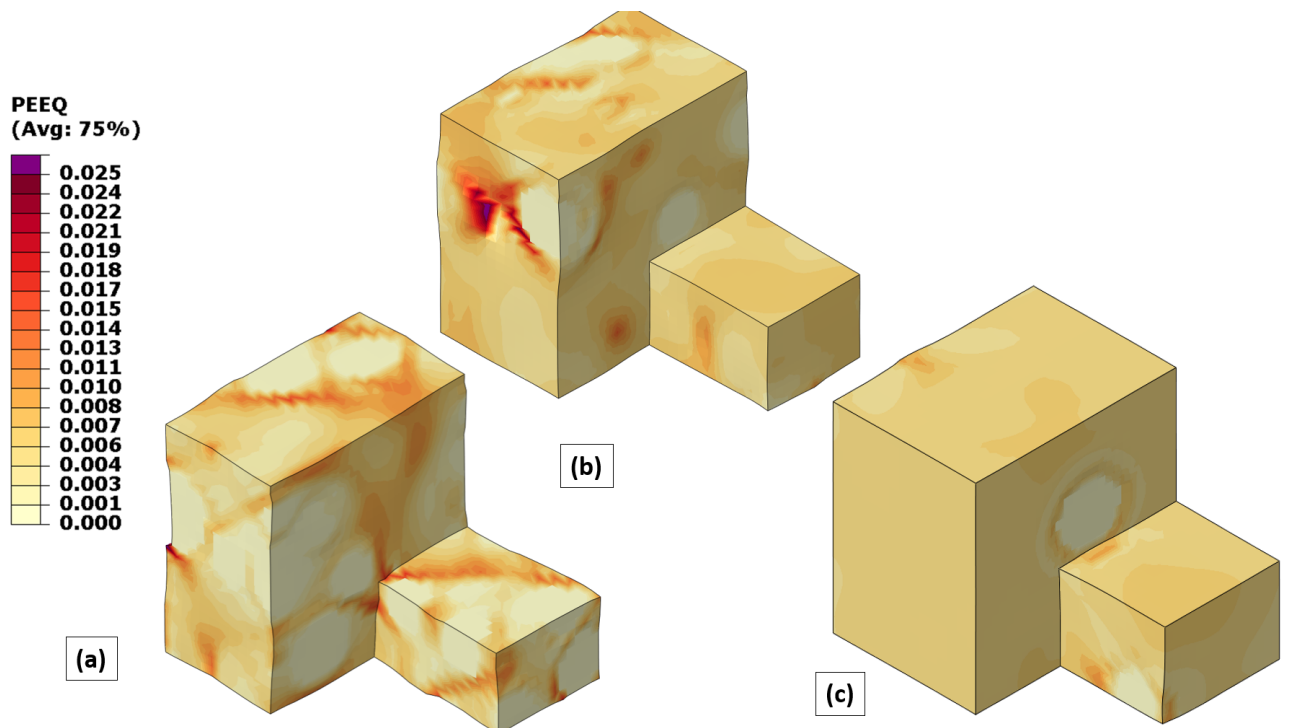


Figure 4.16: Equivalent plastic strain at the final simulation increment for the analyzed RVEs shown in Fig 4.16 (i.e., a section of each RVE has been intentionally removed for better visualization): (a) RVE 1, (b) RVE 2, (c) RVE 3.

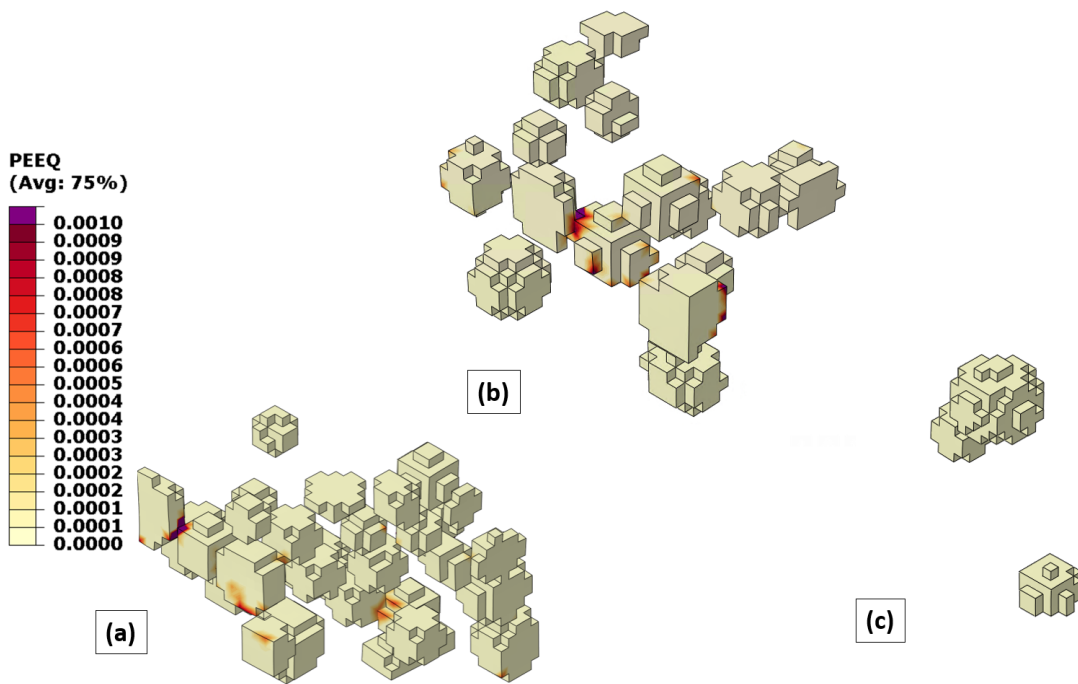


Figure 4.17: Equivalent plastic strain at the final simulation increment for the analyzed RVEs shown in Fig 4.17 (i.e., only the hard phase is shown): (a) RVE 1, (b) RVE 2, (c) RVE 3.

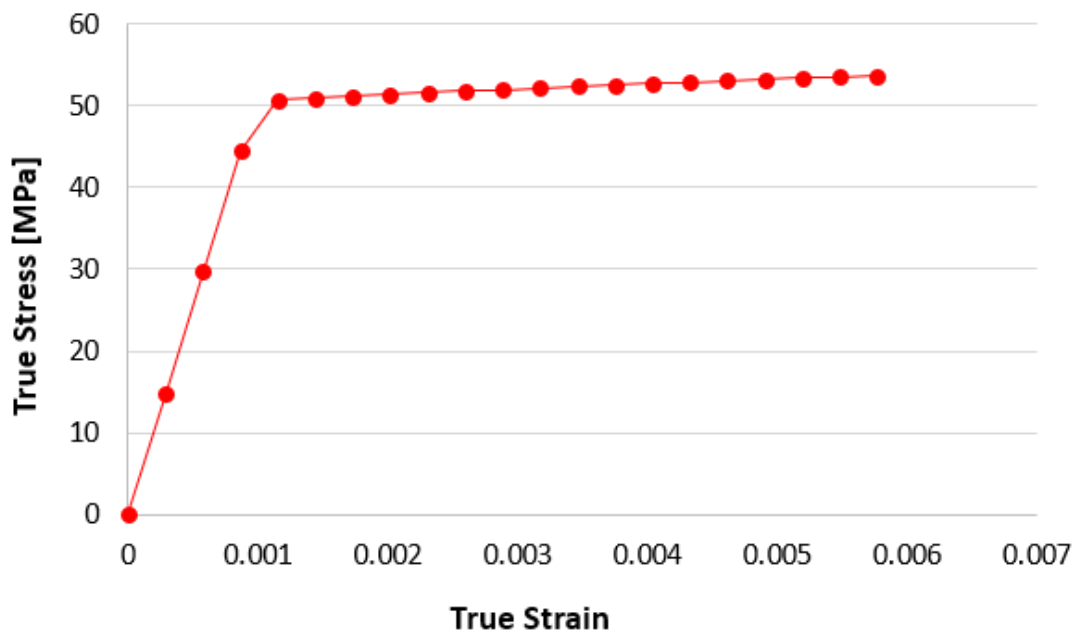


Figure 4.18: An example of the incremental true stress-strain response of the RVE shown in Fig. 4.2. The simulation is performed at ambient conditions of 20 °C. The plotted dots indicate each of 20 increments.

Table 4.2: The von Mises stress convergence analysis for the soft and hard phases under varying mesh densities.

Mesh size	Phase	Stress [MPa]
10×10×10	Soft	31.88
20×20×20	Soft	32.32
26×26×26	Soft	32.43
30×30×30	Soft	32.44
40×40×40	Soft	32.45
50×50×50	Soft	32.45
10×10×10	Hard	135.52
20×20×20	Hard	134.50
26×26×26	Hard	129.72
30×30×30	Hard	129.45
40×40×40	Hard	129.12
50×50×50	Hard	128.78

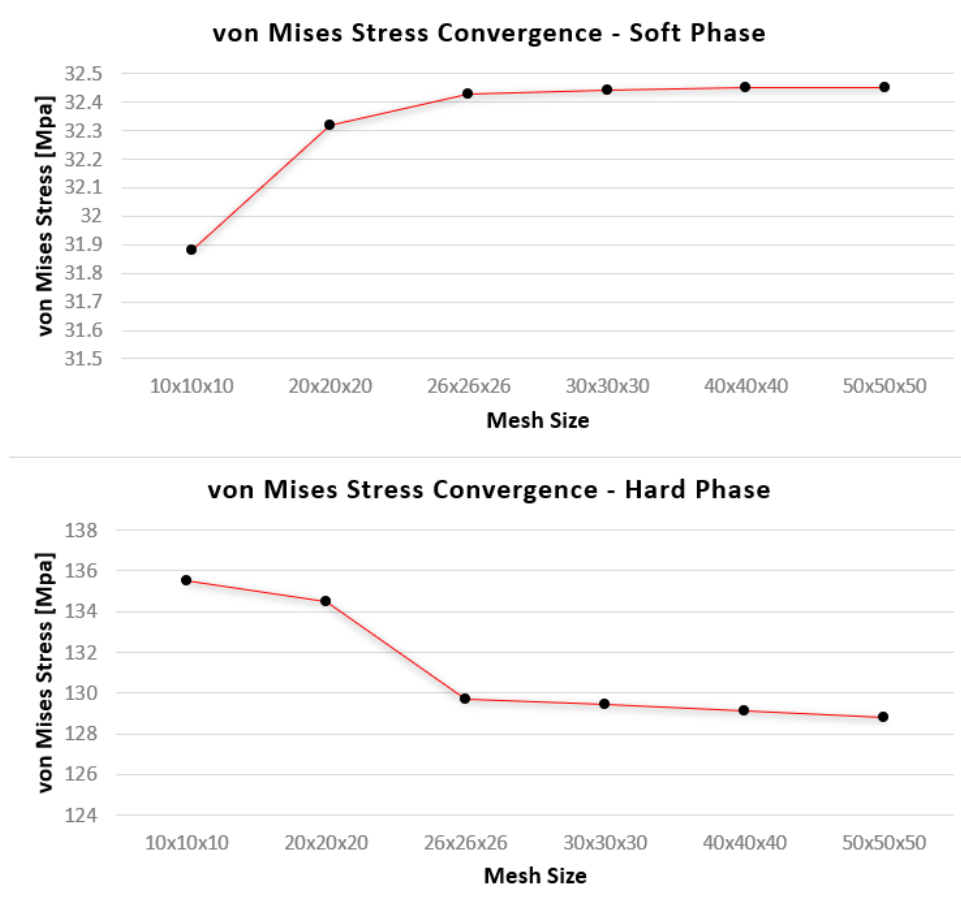


Figure 4.19: Mesh convergence vs von Mises stress for the soft and hard phases under varying mesh densities.

4.3 Overview of the ML Models

4.3.1 Data Preprocessing

In the present study, two quite similar ML models were employed to address the task at hand. Given the complexity of the task, ML models in the form of 3D CNNs seemed appropriate. The first model was dedicated to predicting the true stress-true strain curves, while the second model was tasked with predicting the deformation-induced heat generation. The input for both models was a 3D matrix with dimensions $26 \times 26 \times 26$, reflecting the shape of the RVE. This matrix contained information about the spatial arrangement of the phases. The inclusion of the temperature (for stress-strain curves dataset) and the TQC value (for temperature increase dataset) was achieved by multiplying the matrix by the respective values of temperature and TQC, respectively. The original matrix consisted of zeros representing the soft phase and ones representing the hard phase. The arrangement within the matrix was exactly the same as that of the RVE. Consequently, multiplying the matrix by the TQC and temperature values resulted in a matrix composed of zeros and the magnitude of the assigned variable (i.e., temperature or TQC value). This innovative approach circumvented the need for multiple inputs, such as separate channels for the TQC value and temperature information, as well as phase arrangement information, which would have significantly increased computational costs.

In essence, the ML model input is phase arrangement information and data about temperature and TQC value. The methodology of this approach points out the potential of ML models in predicting complex material behavior, contributing to the broader field of computational mechanics and computational materials science. The approach to representing the input data not only simplifies the architecture of the model, but also improves the efficiency of the calculations – a critical factor in large-scale simulations.

In an effort to develop a robust and reliable ML model for temperature increase dataset, a careful process of data selection was undertaken. This process was guided by the principle of ensuring the relevance and significance of the data used in the training phase. A critical parameter in this selection process was equivalent plastic strain (ϵ_p), which is the source of heat generation and consequently temperature increase. The dataset used for the training of the ML model was carefully tuned to include only those results where ϵ_p exceeded a threshold of 0.00228. This threshold was set based on the observation that it corresponded to the last 12 increments of strain, which were found to be of significant importance in the context of this

study. The first 8 increments, on the other hand, were not used since the plastic strain is non-existing or negligible.

In areas subjected to stress concentration, such as at the interface between the soft and hard phases, ϵ_p values less than 0.00228 were observed. However, the amount of heat generated during these initial increments was considered insignificant, especially when compared to the heat generated during the final 12 increments. Excluding these initial increments from the learning process was found to be beneficial to the convergence of the ML model. This decision was supported by the finding that these points affect the learning process of the model, while their exclusion would result in only a minimal loss of overall accuracy. In contrast, all 20 increments were used for the stress-strain dataset. This difference in approach points out the importance of a context-specific data selection and preprocessing strategy when developing ML models.

4.3.2 ML Models

The developed ML models use the microstructural configuration, temperature, and TQC value as inputs and produce stress-strain and temperature increase-strain curves as outputs. Schematic representations of these processes can be found in Figs. 4.20 and 4.21. These schematics provide a visual representation of the data flow within the models, and show the complex interactions between inputs and outputs.

The architecture of the CNNs was designed with a sequential network that allows for structured and ordered processing of input data [99]. Starting with a 3D convolutional layer, the CNNs captured complex spatial relationships in the data, which were then passed through a Parametric Rectified Linear Unit (PReLU) activation function [100] to improve the stability of the CNNs and improve the convergence. Batch normalization was implemented following the PReLU activation. Subsequently, a max-pooling layer [101, 102] was then integrated to reduce the spatial dimensionality of the output while maintaining salient features.

The architecture then included a unique structure referred to as a flattening. This component acted as a bridge between the convolutional layers and the fully connected layers, providing a transition from feature extraction to classification. A sequence of fully connected layers with decreasing neuron counts (512, 256, 128, 64, and 20) served as the primary regression component of the CNNs. In each layer, batch normalization and PReLU activation were consistently applied ensuring the stability of the learning process. The final stage of the CNNs' architecture was a set of logistic output neurons that generated the strain-temperature increase and stress-strain

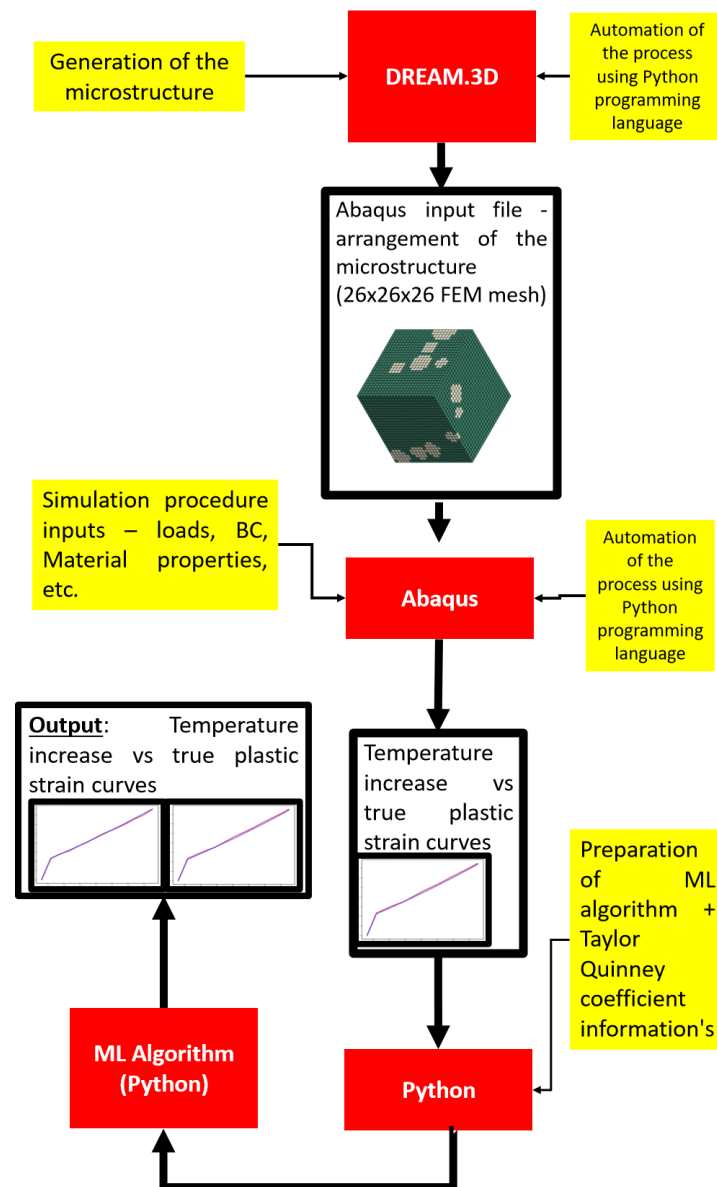


Figure 4.20: Detailed schematic representation of the ML process employed for utilizing the temperature increase-strain dataset.

curves. In the stress-strain curve task, 20 neurons output 20 uniformly distributed intervals, whereas in the temperature increase-strain task, 12 neurons output 12 uniformly distributed intervals. Schematic representations of these CNN models can be found in Figs. 4.22, 4.23. The detailed design of the models was made to optimize the balance between model complexity, performance and computational time. Optimization of ML models and methodology of choosing optimal CNN configuration is presented in Appendix A.

Both CNNs were trained using Python software, specifically the TensorFlow and Keras libraries. These libraries provide a robust platform for complex computations and are well-

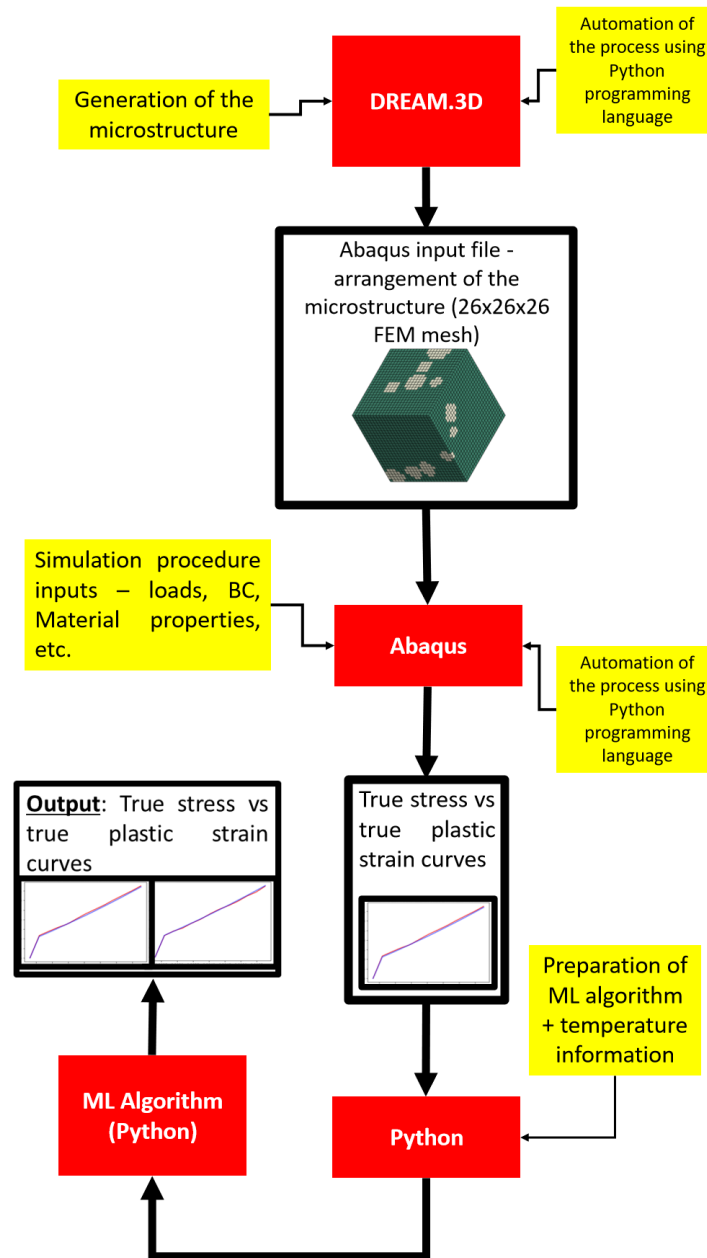


Figure 4.21: Detailed schematic representation of the ML process employed for utilizing the stress-strain dataset.

established in the field of ML. The training process reached convergence after approximately 300 epochs, using Adam optimizer [103], an optimizer known for its efficiency and computational effectiveness. Different datasets, namely the temperature increase-strain curves and the stress-strain curves, required different learning rates, which were set at 0.00025 and 0.0005, respectively. The decay rate was defined as the ratio of the learning rate to the number of epochs, while all other parameters was kept default values in Keras library (β_1 was set to 0.9, β_2 to 0.99, and ϵ to $1 \cdot 10^{-7}$) for both datasets. For further details on the parameters of the Adam

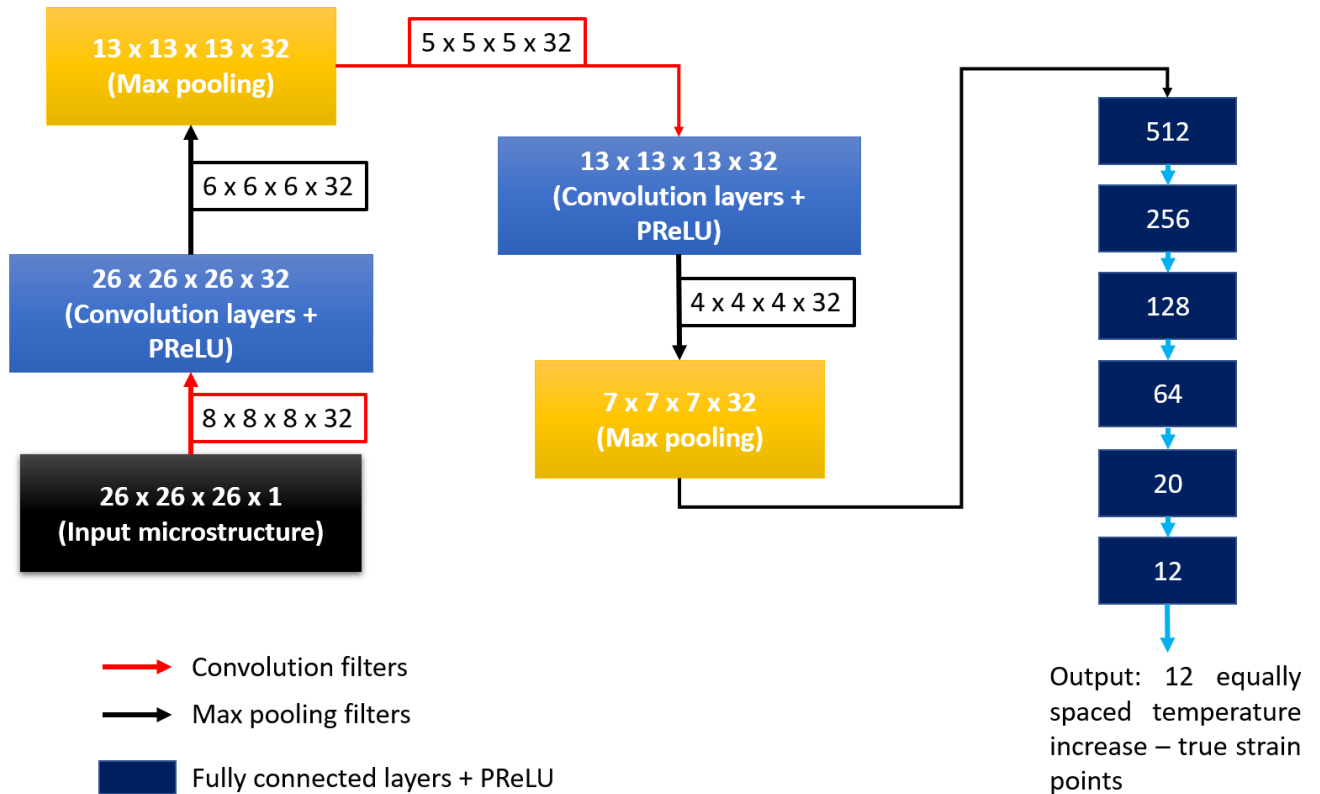


Figure 4.22: Detailed schematic representation of the ML model utilized for correlating the temperature increase-strain dataset.

optimizer, readers are referred to [103] and TensorFlow and Keras documentation. The training was performed on an Nvidia Quadro K2200 GPU. The entire training process was completed in approximately one hour for both datasets.

The datasets for the temperature increase-strain and stress-strain curves were split into training, validation, and test sets. For the temperature increase-strain dataset, a ratio of 70:20:10 was chosen, whereas a ratio of 60:20:20 was used for the stress-strain dataset. This decision was guided by the intent to ensure a balance between learning and validating the model while still maintaining a sufficient amount of data for testing. The training and validation processes were guided by the mean squared error (MSE) as the chosen loss measure. In addition, model weights were recorded for each epoch, and, after training, the set of weights with the best validation score was selected. This approach helped circumvent the issue of convergence instability and ensured that the final model selected was the one that demonstrated the best performance on the validation data.

The models were then subjected to validation using curves obtained from FEA simulations. The models were manually calibrated (see Appendix A), which means that while these models

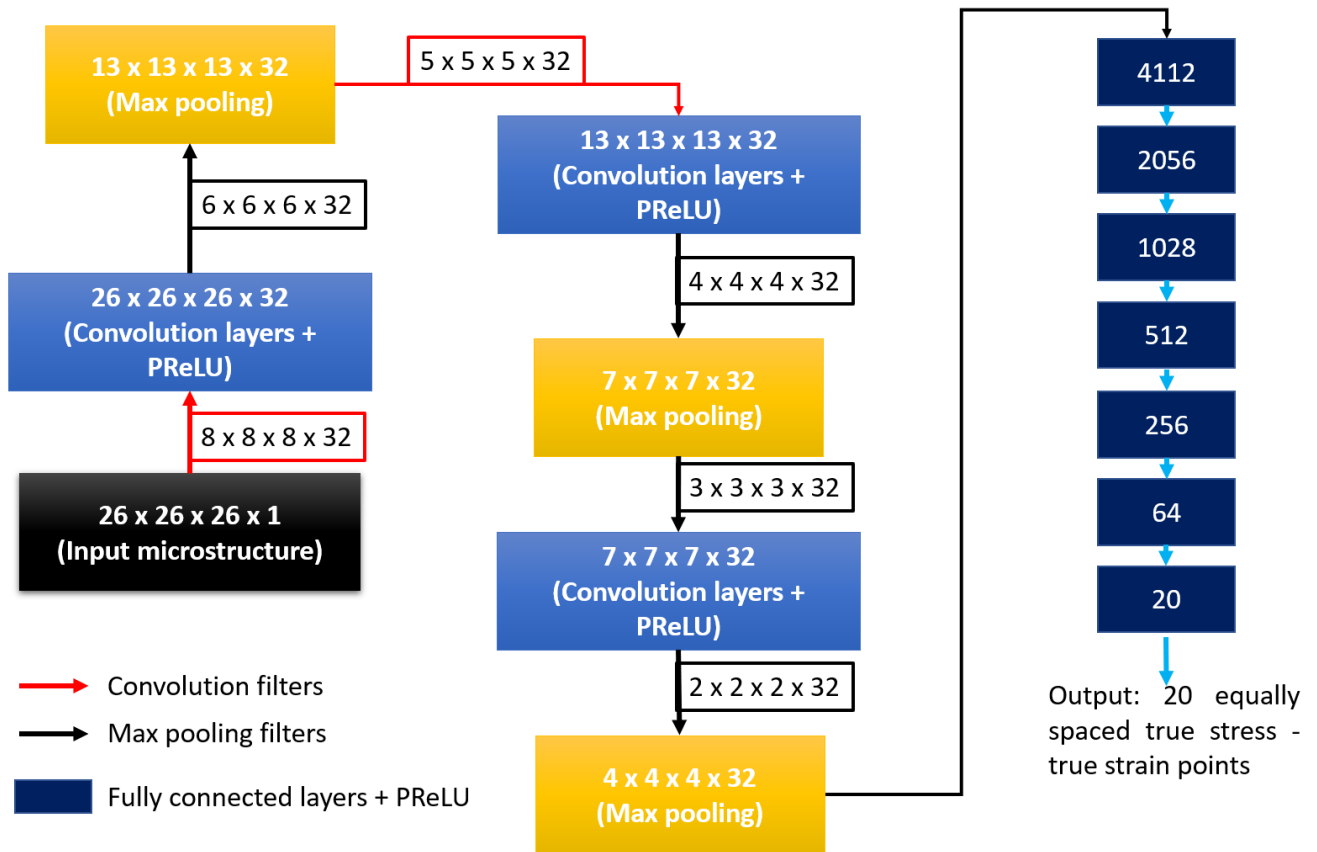


Figure 4.23: Detailed schematic representation of the ML model utilized for correlating the stress-strain dataset.

have shown quite good performance, there may be an alternative model configuration that could provide better results. It is important to note that the choice of model architecture was not motivated by any particular theory or framework. Instead, an initial architecture was chosen in accordance with similar studies [62, 64], and the architecture was manually optimized using trial and error (see Appendix A). Dimensionality reduction techniques such as MDS and PCA, commonly used in similar studies [60, 61, 64, 104] to reduce the complexity of the problem, were intentionally excluded from this study because they can remove important data features in the dataset needed for accurate and reliable model results. Nevertheless, as described in Chapter 5 the training time was considered reasonable and the models attained good results, thus eliminating the need for these dimension reduction techniques.

In summary, microstructure configurations generation was accomplished via an automated process utilizing the Python programming language and DREAM.3D software. This generated microstructural configurations that were converted into an input file for the Abaqus software ensuring accurate representation of the phases within the RVE. A numerical simulation procedure

was then created in Abaqus, which included the assignment of material properties, BC, and definition of the numerical procedure. This entire process was automated using Python software, enhancing the consistency and reliability of the process.

The results included stress-strain and temperature increase-strain curves metrics of the material's behavior. In addition, Python was employed to generate the input parameters for the ML models, including phase arrangements, TQC value, and temperature, along with the mentioned curves. This approach facilitated the creation of a robust dataset enabling data-driven analysis of the microstructural simulation of the material behavior.

Chapter 5

Results and Discussion

5.1 Evaluation of Different ML Models	68
5.2 Results for the Temperature-dependent Stress-strain Curves – Six Specific Temperature Levels	72
5.3 Results for the Temperature-dependent Stress-strain Curves – Random Temperature Levels	80
5.4 Results for the Temperature Increase – Strain Curves	84
5.5 Influence of Phases Distribution – Random Temperature Levels Dataset .	90
5.6 Influence of Phases Distribution – Temperature Increase Strain Curves .	96

Chapter 5 examines the evaluation of different ML models and predictive capabilities of the two ML models created. This examination is divided into six specific Sections, each of which emphasizes a particular part of the overall model result. The first one, Section 5.1 evaluates the different ML models used for optimization. In the second Section, 5.2, the evaluation focuses on the ML model, which was developed for predicting stress-strain curves. The accuracy of this model is evaluated using an independent test dataset.

An additional test dataset is described in Section 5.3. This additional dataset is unique in that it contains simulations performed at temperatures ranging from 20 °C to 250 °C. Unlike the dataset containing the six specific temperature intervals, this particular dataset includes all temperatures randomly generated within the specified interval. The underlying objective of this is to evaluate the ability of the model to handle simulations with random temperature values that were not included in the training data. This decision is based on the desire to improve the

applicability of the model while maintaining its simplicity by only training it at six specific temperature levels. This serves to further validate the generalization power of the ML model under untested conditions, which is of most importance in confirming its practical usefulness. For all of the test datasets used, two important statistical measures, MSE and RMSE, are calculated to quantify the accuracy of the model. These measures provide insight into the deviation of the model's predictions from actual values, calculating the model's performance. The results are then analyzed in depth to highlight the model's strengths, weaknesses, and opportunities for improvement.

Section 5.4 examines the performance of the temperature increase-strain curves ML model. For the purpose of this evaluation, test dataset is again used. This dataset, which is not used to train the model, provides a robust measure of the model's predictive capability, allowing for an evaluation of its accuracy.

Moving forward, the analysis of center of gravity (CoG) distances and their relationship with temperature increase and stress-strain curves are presented in Section 5.5 and Section 5.6. The objective here is to find the impact of hard phase fraction on CoG positioning and its impact on prediction error, stress values and temperature increase. This concludes the Results and Discussion Chapter.

5.1 Evaluation of Different ML Models

An evaluation of the predictive performance of six different CNNs for both stress-strain and temperature-increase dataset is performed. For both datasets, the same CNN2-CNN6 models are utilized for comparison, while the CNN1 model is slightly modified for each problem. An evaluation of the predictive performance of six different CNNs for the stress-strain dataset, summarized in Tab. A.1, is illustrated in Fig. 5.1. From Figs. 5.1 and 5.2, it is evident that similar conclusions explained below can be drawn for both datasets. However, the trend of global error, MSE, and RMSE is slightly lower for stress-strain curves.

For the temperature increase dataset, predictive performance of CNNs summarized in Tab. A.2, is shown in Fig. 5.2. Progressing from the simplest to more complex configurations to evaluate their performance on the present task, the designs of CNN5 and CNN6 are based on relatively simple CNN architectures. Both models share similarities in their simplicity. Unfortunately, they both exhibited very poor performance on this task. Their MSE and RMSE values were sub-

stantially higher than those of the best-performing model, with error margins exceeding 1000 %. This indicates that such basic CNN models are unsuitable for performing this kind of task on this scale. Similar observations could be drawn also for stress-strain dataset, however, as already mentioned the error magnitude is much lower.

Conversely, the CNN4 model features a slightly more complex design. It is notably enhanced by the use of the Adam optimizer instead of the SGD optimizer, and PReLU activation functions rather than standard ReLU functions. This modification led to a significant improvement in performance over CNN5 and CNN6. Despite this improvement, the results still did not meet the required standards for the task. Therefore, it can be inferred that the Adam optimizer combined with PReLU activation functions is more effective than the SGD optimizer paired with ReLU activation functions for this particular task.

Furthermore, the more complex CNN3 model, which utilizes an SGD optimizer and ReLU activation functions, performed worse than the simpler CNN4 model, supporting the previously mentioned conclusion. Generally, it can be concluded that although the more complex CNN3 model's performance may not be adequate for the current task, it still surpasses the simpler CNN6 and CNN5 models that use the same activation functions and optimizers.

The CNN2 model has a configuration similar to the CNN1 model, albeit with slightly less complexity. It is also noteworthy that comparing the CNN2 and CNN1 models reveals that a small proportion of dropout slightly decrease the model's performance. The CNN2 model demonstrated notable performance on both tasks, yet its metrics and global error were inferior to those of the CNN1 model. Additionally, it was observed that increasing the kernel size and max-pooling filter size raised the computation time. As a result, the CNN1 configuration is chosen as the primary one in this study for both datasets.

Thus, it can be concluded that the model's complexity, along with the choice of activation functions and optimizers, are very important for accurately predicting the temperature increase-strain curves as well as stress-strain curves considering SPR task. It is important to note that this study did not explore all possible combinations of activation functions, parameters, and optimizers, instead, it focused on some of the most popular choices. Also, due to the complexity of the task and due to the bad prediction capability of simpler CNN models, some popular shallow learning approaches such as regression trees, ANNs, and others were also not investigated in this study.

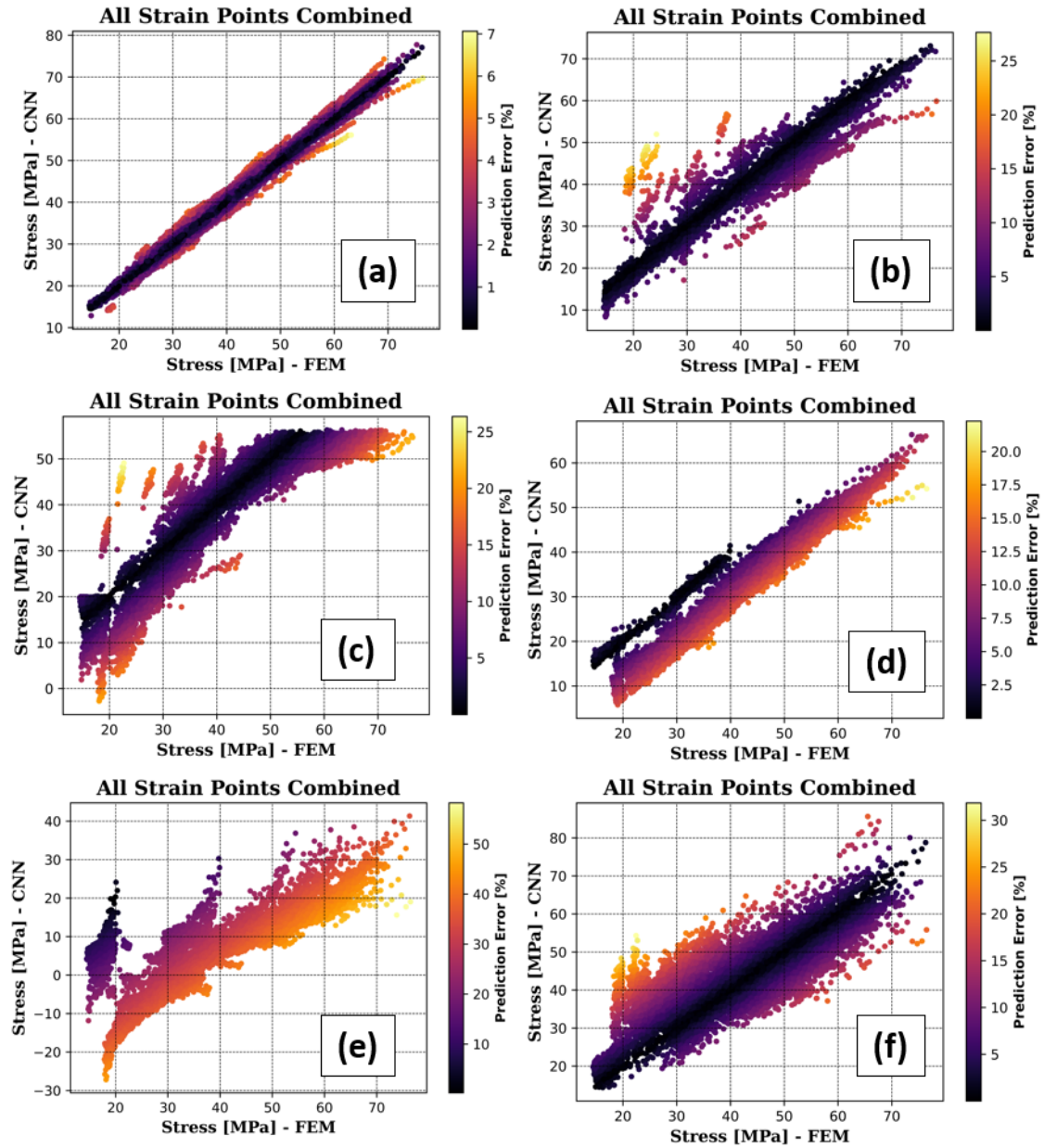


Figure 5.1: Comparison between the calculated (FEA) and the predicted (CNN) value of the stress for all points of the stress-strain curve for: (a) – CNN1 Model, (b) – CNN2 Model, (c) – CNN3 Model, (d) – CNN4 Model, (e) – CNN5 Model, (f) – CNN6 Model in Table A.1.

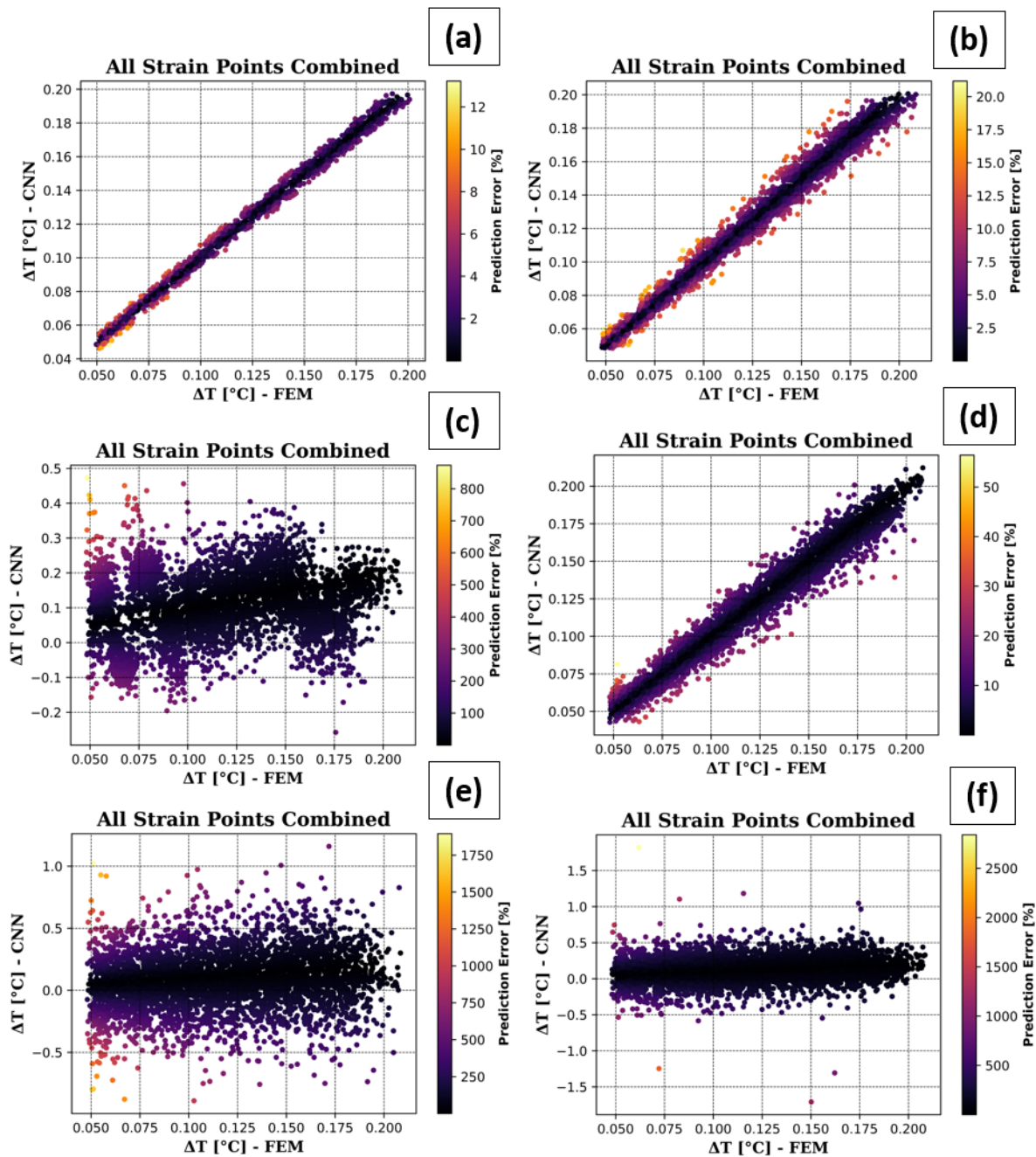


Figure 5.2: Comparison between the calculated (FEA) and the predicted (CNN) value of the temperature increase for all points of the temperature increase curve for: (a) – CNN1 Model, (b) – CNN2 Model, (c) – CNN3 Model, (d) – CNN4 Model, (e) - CNN5 Model, (f) – CNN6 Model in Table A.2.

5.2 Results for the Temperature-dependent Stress-strain Curves – Six Specific Temperature Levels

The first stage of this study involved an evaluation of the CNN1 ML model's performance on a dataset to six specific temperature levels. This examination was conducted using a previously created test dataset of 596 RVEs that had not been used during the training phase of the ML model, thus ensuring a fair evaluation of its predictive ability. The metrics that emerged from this evaluation were quite good. The R^2 value reached a score of 98.5%, indicating a good relationship between the predicted and actual values. The RMSE and MSE values, fundamental indicators of the model's accuracy, were calculated to be 0.99 MPa and 0.98 MPa, respectively, underscoring the model's accuracy in its predictions. Importantly, the model also exhibited very good computational efficiency, making 596 predictions in slightly less than one second.

Fig 5.3 illustrates the comparative analysis of the true stress-true strain curves obtained by the ML model and the FEA simulations. The specific set of curves presented in this comparison for each temperature level includes a different combination of microstructural configurations and hard phase fractions, chosen to ensure a broad spectrum of potential scenarios. All of these varying parameters have a significant impact on the resulting flow curves. The observed trend is intuitive. It appears that higher simulation temperatures and lower hard phase fractions jointly contribute to a decrease in the flow curves. For example, the tensile strength of the RVE simulated at a temperature of 150 °C actually exceeds that of the RVE at 100 °C, which can be attributed to the increased hard phase fraction within the RVE.

In addition, Fig 5.4 provides a detailed comparative analysis of the true stress-true strain curves predicted by the ML model, incorporating variations in temperature and hard phase fractions. It should be noted that for this task, only a randomly selected 150 curves were examined. The figure clearly demonstrates the overall trend of increasing stress magnitude with higher hard phase fractions and lower temperatures. Notably, the tensile strength of some curves at higher temperatures exceeds those at lower temperatures, further confirming the significant contribution of the hard phase fraction to the overall stiffness of the RVE.

Some of the predicted flow curves exhibit minor discontinuities. However, this is a rather expected phenomenon given the inherent variance in the predictions of individual data points associated with a margin of error. These discontinuities reflect a local decrease in stiffness, but could be effectively overcome by well known curve smoothing techniques (see for example

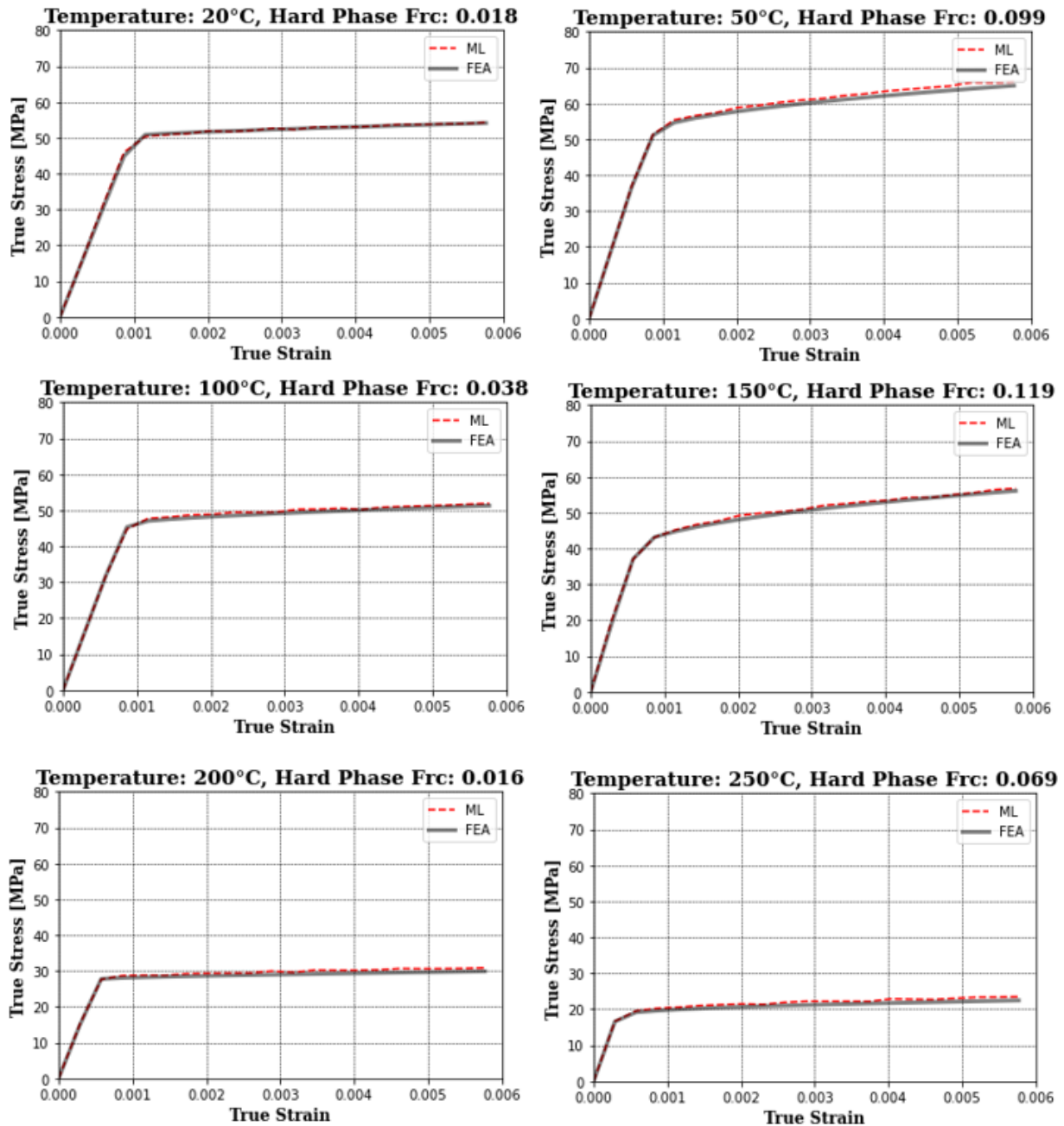


Figure 5.3: Visualization of true stress-true strain curves predicted by the ML model and ones simulated by FEA.

[105, 106]). Despite this potential for further refinement, it is beyond the scope of the present study. Therefore, upon evaluating the results shown, it is clear that the predicted flow curves are significantly affected by three key parameters: the microstructural configuration of the RVE, the hard phase fraction, and temperature. This complex interplay of variables demonstrates the multi-faceted nature of the simulation process and the resulting need for an approach in the development of predictive ML models such as the model employed in this study.

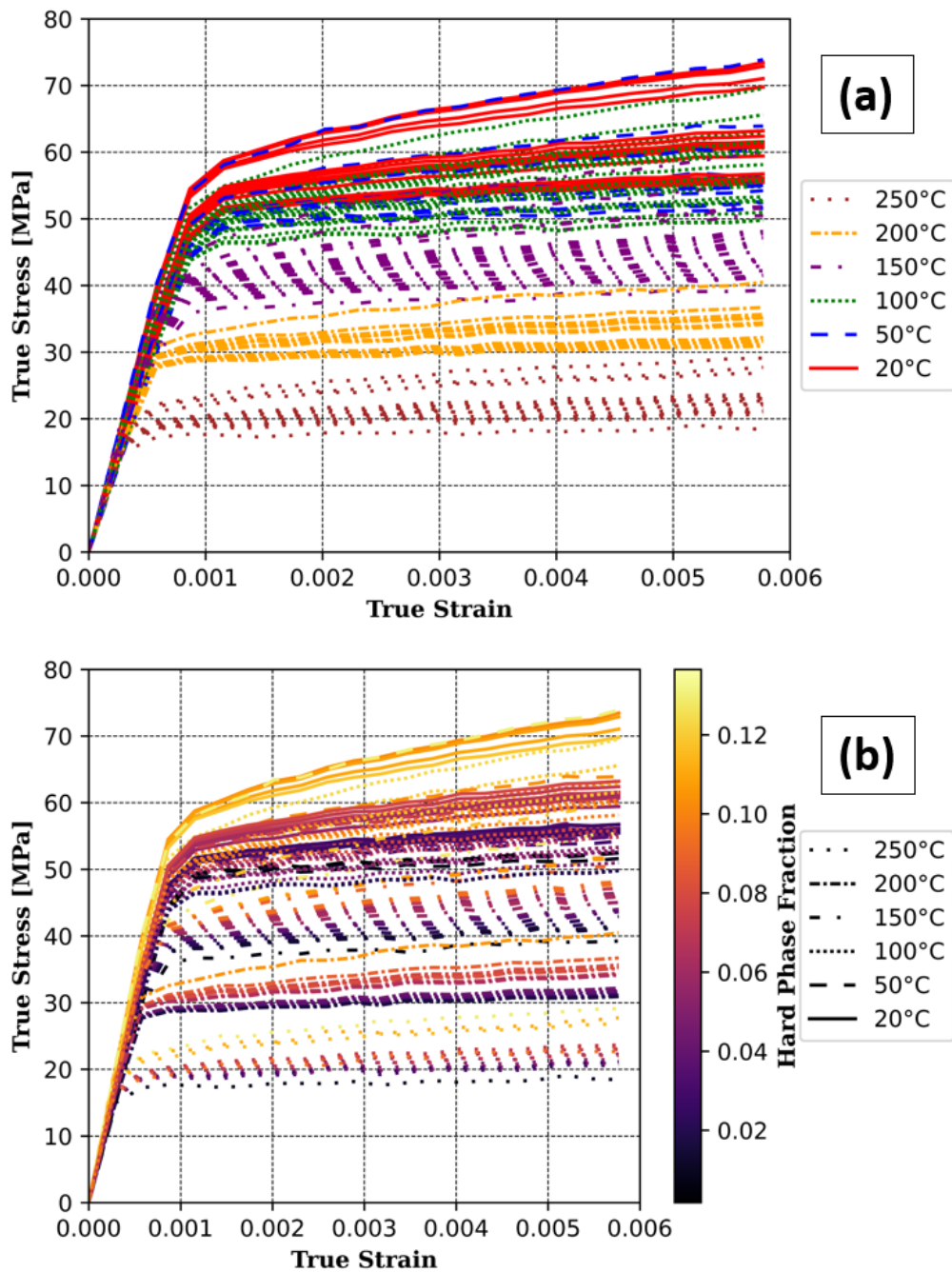


Figure 5.4: Visualization of true stress-true strain curves predicted by the ML model: (a) colored by temperature level and (b) colored by hard phase fraction.

Unlike many traditional approaches, the ML models developed in this study do not include explicit hardening constants. Instead, they rely on the stress-strain curves of the individual phases. This innovative methodology allows the ML models to accurately interpret the hardening behavior of the material by analysing the microstructural configuration and response of the two-phase RVE. The CNN, used in this work, demonstrates a robust capability for predicting the mechanical behavior of various microstructural configurations.

Again, it must be emphasised that under the scope of the present research, these models were trained under the specific constraints of uniaxial tensile tests. Therefore, the accuracy of their application under other BC is yet to be verified. While the predictive power of the models is quite acceptable within their training parameters, extending their application beyond these conditions could lead to inaccurate results.

The verification of the ML model's prediction accuracy also involved a detailed comparison of all stress-strain points with the corresponding results derived from FEA simulations. The first step of this process was an analysis of the first and last four points in the simulation interval. The study determined that other points across the interval exhibited similar behavior to the last four points, and thus, for simplicity, they were not examined. The comparison is visually presented in Figs. 5.5 and 5.6. An important observation in these figures is the tendency for the values to be grouped into two or sometimes even three distinct clusters. This tendency stems from the FEA simulations conducted at higher temperatures (predominantly 200 °C and 250 °C), which invariably resulted in significantly lower flow curves and thus significantly lower values at these particular temperature levels, see also Fig 5.4.

Of particular interest is the positioning of strain point 2, which is located in the elastic region of the curve except for the temperature level of 250 °C. This region of the curve is characterized by a much greater slope (e.g., see Fig. 5.4) when contrasted with the plastic region. Similar characteristics are also evident in strain points 3 and 4, thereby reinforcing the distinct value discrepancy across different temperature levels, with the largest difference being seen at strain point 2.

In the following detailed analysis of the predictive capability of the ML model, its performance was compared with FEA simulation in Fig. 5.7. The ML model predicted the material behavior under various strain points with good accuracy, as shown by the maximum discrepancy of 7.8 MPa or 10.12 %. This discrepancy between the ML predicted value and the FEA calculated value serves as a testament to the reliability of the model, as it is not only minor, but also well within the standard scatter of values typically observed in tensile tests on certain materials such as aluminum or magnesium. Furthermore, the mean (average) difference was 0.7 MPa or in average 0.65 %. Both predicted and calculated values both lie in the range of 14 MPa to 80 MPa, indicating that the model covers the entire spectrum of possible outcomes. When the analysis was confined to the first strain point, the range of these values narrowed down to 14 to 20 MPa, while for the final strain point, the range broadened to span from 20 MPa to approximately 80

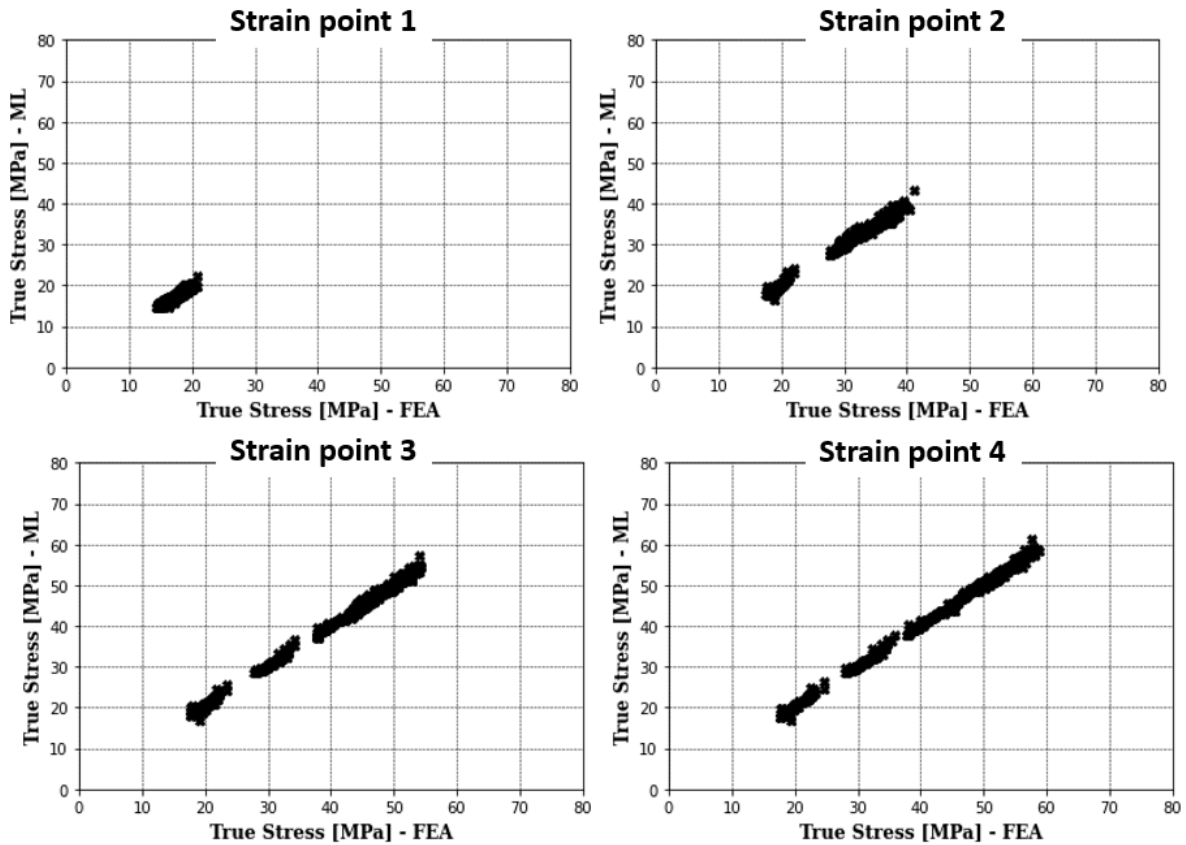


Figure 5.5: Comparison of stress values calculated by FEA with those predicted by the ML model for strain points 1, 2, 3 & 4. The graph includes the true stress-true strain curves calculated for all six temperature levels.

MPa.

In comparing the FEA simulations with the ML model, six discrete temperature levels were systematically analyzed. This examination encompassed all strain points from each RVE in the test dataset, with the results presented in Fig. 5.7. It is evident that higher temperatures generally correlate with lower stress values, suggesting an inverse relationship between the two variables. However, the dataset contains exceptions to this trend. For instance, at 100 °C, some stress values surpass those observed at 20 °C and 50 °C as well as some at 50 °C surpass those at 20 °C. In Fig 5.4 a similar trend could be also noticed, however, not all the curves are included in that graph, therefore, in that case, only some 50 °C are surpassing 20 °C curves. These outliers may be attributed to the stochastic nature of the microstructural configuration. Specifically, the configuration at 100 °C and 50 °C, characterized by a higher hard phase fraction and a stiffer microstructural arrangement, appears to be an anomaly. This stiffer configuration, randomly selected due to inherent system randomness, led to an unexpected increase in stress values despite the higher temperature. Consequently, the relationship between microstructural characteristics,

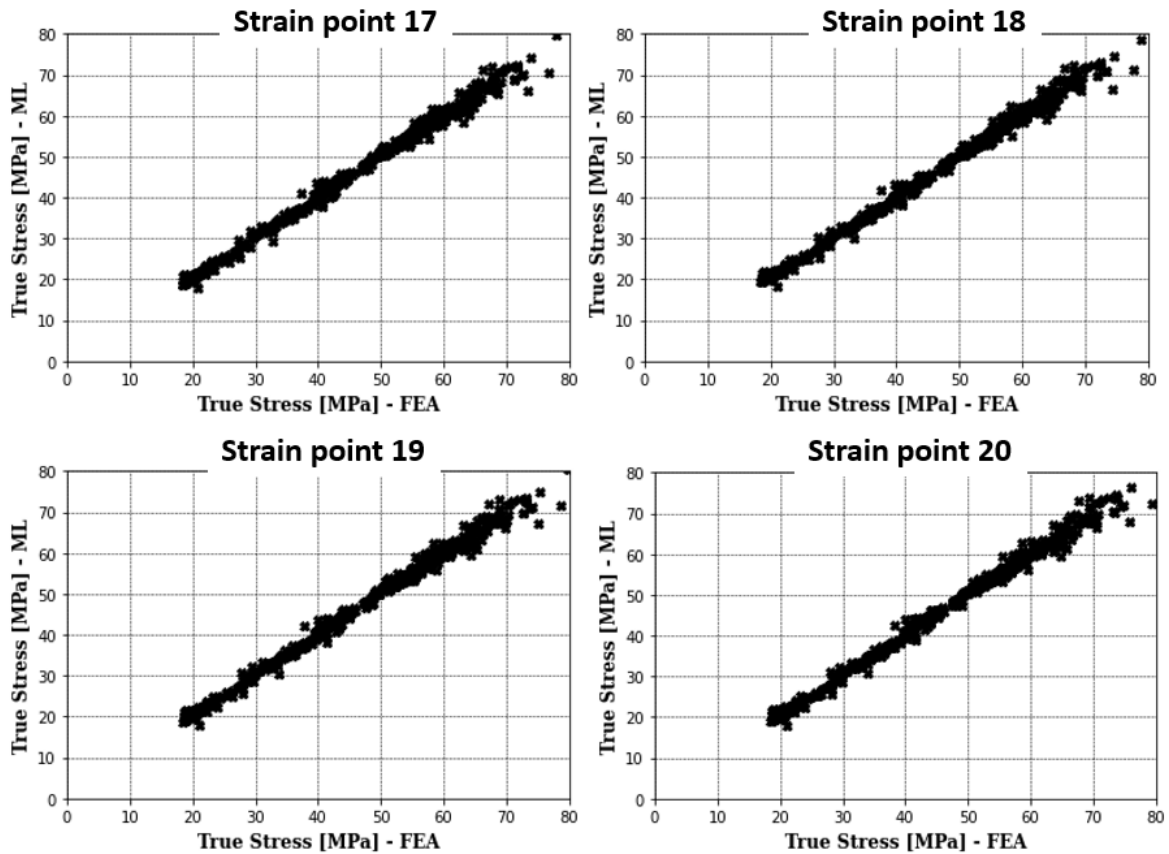


Figure 5.6: Comparison of stress values calculated by FEA with those predicted by the ML model for strain points 17, 18, 19 & 20. The graph includes the true stress-true strain curves calculated for all six temperature levels.

phase fraction, and temperature is complex, deviating from a straightforward inverse relationship between temperature and stress.

Evaluation of the FEA and ML generated stress values provides further insight into the effects of hard phase fraction on the overall results. The comparative analysis, as detailed in Fig. 5.8, shows all strain points to provide an overview of the phenomenon. The dominant trend is that the stress values increase in line with the increase in the hard phase fraction. Another interesting observation made during the analysis is the achievement of a peak stress value of 82 MPa at a hard phase fraction of 0.125. This value occurs rather unexpectedly, as opposed to the expected maximum fraction value of 0.15. However, this could also be attributed to the randomness of the microstructural configuration or temperature. Thus, the particular configuration at a hard phase fraction of 0.125 obviously leads to a stiffer configuration than the configuration at a higher hard phase fraction.

It should also be noted that graphical interpretation of the data could be difficult due to the overlapping values. Nevertheless, the dominant trend is evident. The data presented again con-

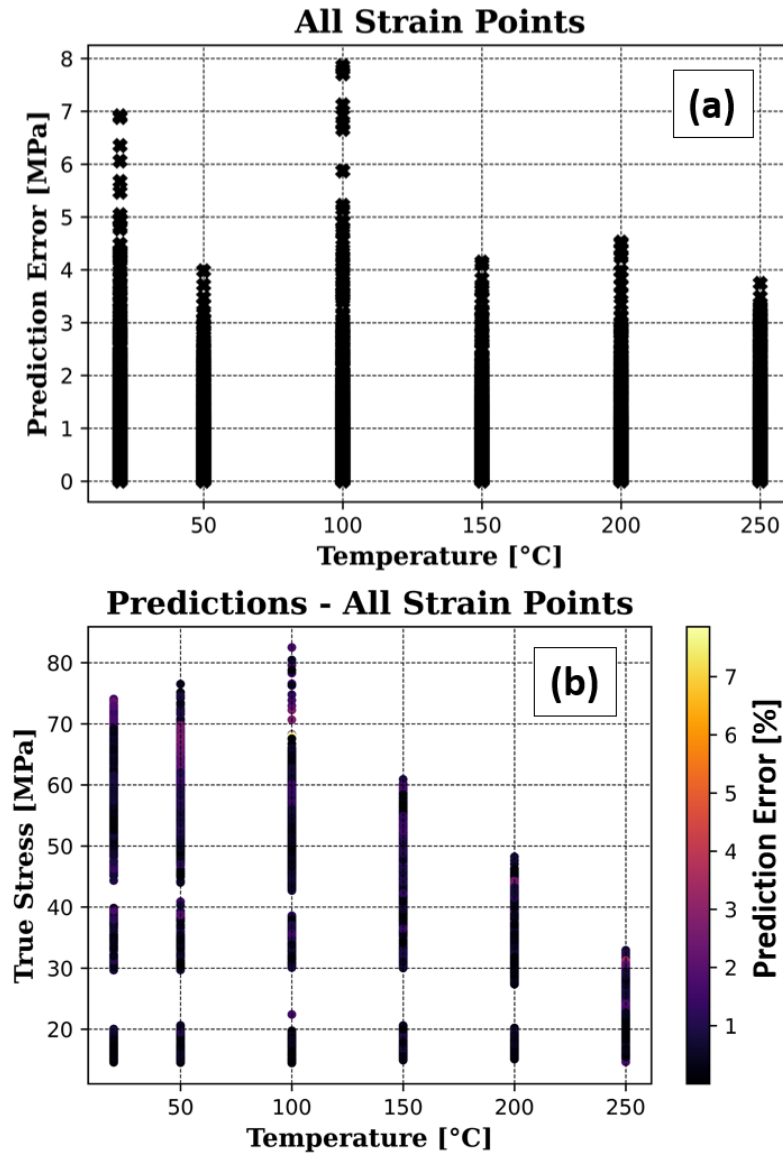


Figure 5.7: Stress values calculated by FEA and predicted by the ML model as a function of different temperatures. Plot includes temperatures from all six temperature levels and all 20 simulation increments of the true stress-true strain curve: (a) prediction error vs. temperature, (b) true stress vs. temperature (prediction error is color-coded).

firmly that the stress-strain response is significantly affected not only by the hard phase fraction, but also by the microstructural arrangement. This underlines the essential role of the microstructural arrangement in determining the mechanical properties of the multiphase material. The potential of the ML model to capture subtle influences, including phase fraction, temperature, and, microstructural arrangement, is thus confirmed. A plausible hypothesis might suggest that the adoption of larger RVEs could potentially reduce the influence of randomness, but such a hypothesis extends beyond the scope of the present study.

Additionally, the investigation also extends to the impact of dataset size on the outcome

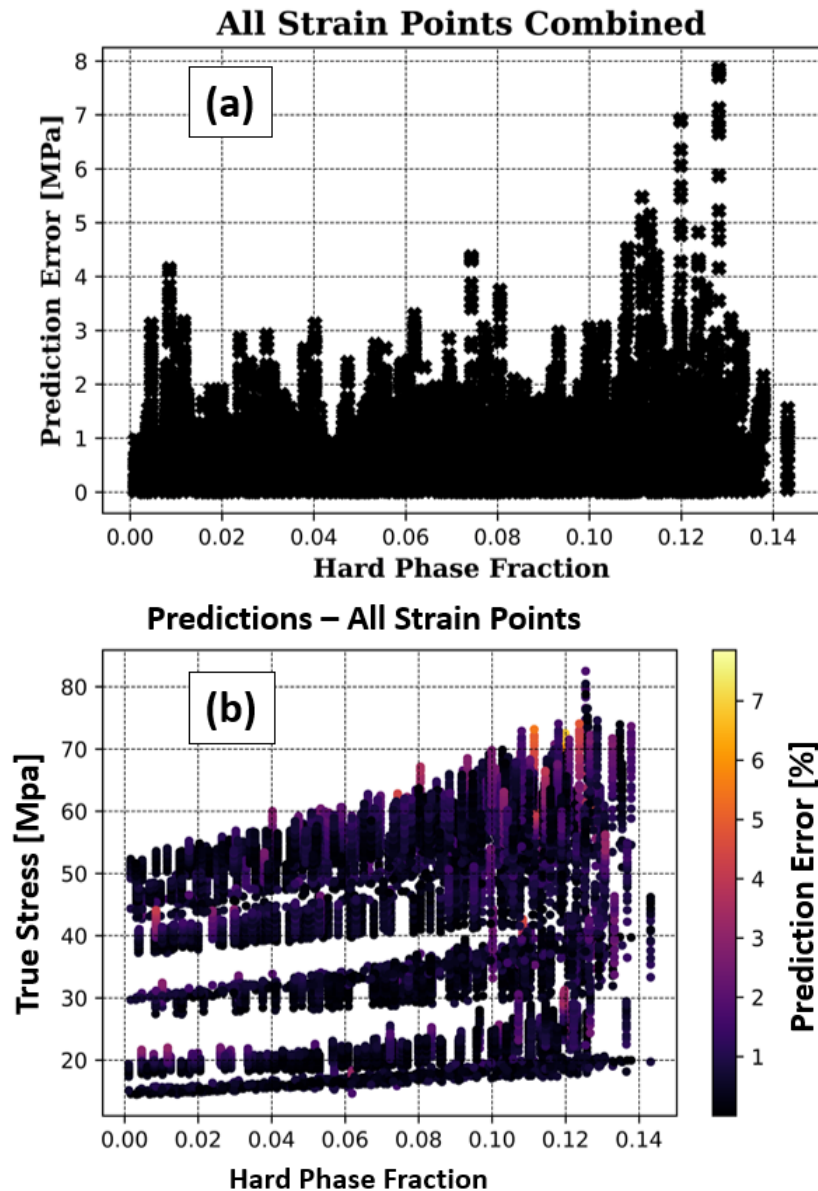


Figure 5.8: Stress values calculated by FEA and predicted by the ML model as a function of different phases fraction. Plot includes temperatures from all six temperature levels and all 20 simulation increments of the true stress-true strain curve: (a) prediction error vs. temperature, (b) true stress vs. temperature (prediction error is color-coded).

metrics, in this case only the MSE. To better understand this relationship, a small study was conducted using subsets of the original dataset. The goal of this exploratory study is to understand how the size of the dataset interacts with the MSE. For the purposes of this investigation, the MSE was examined for ML models trained from test datasets varying in size, namely 80%, 60%, 40%, and 20% of the original test dataset size. To ensure consistent testing parameters, the same ML model configuration that was used to train the entire dataset was used for all of these subsets. The results of this study, shown in Fig. 5.9, show a noticeable trend: as expected,

the performance of the ML model decreases as the size of the dataset size decreases. This is a predictable outcome, but it is noteworthy in the context of the applicability of the model.

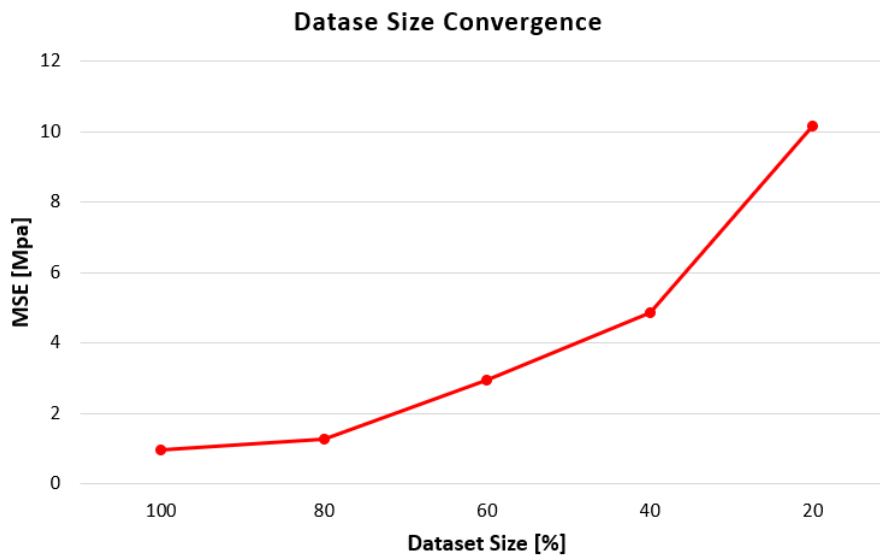


Figure 5.9: Convergence of dataset size vs MSE.

In particular, at dataset size of 80%, the model's performance metrics still remain relatively stable, suggesting that a reasonable reduction in dataset size does not significantly compromise the quality of the model's predictions. Reducing dataset size down to 60%, MSE is increased even more. However, when the dataset size is further reduced to 40% and 20%, the MSE increases significantly. This indicates that the performance of the model decreases significantly with these smaller datasets and thus raises questions about the reliability of the model when trained with substantially limited data. This observation underscores the importance of having a sufficient amount of data to train an effective ML model.

5.3 Results for the Temperature-dependent Stress-strain Curves – Random Temperature Levels

Based on the previous findings, it is necessary to highlight the ability of the ML model to accommodate broader temperature ranges for its practical applications. Due to the simplifications made during the initial training phase, the ML model was trained considering only six discrete temperature levels. However, it should be demonstrated that the ML model performs well for other temperatures as well. For this reason an additional test dataset with random temperatures

was generated. Thus, a smaller but also representative dataset of 492 RVEs was created. This secondary dataset replicates the randomness of the combinations of temperature and microstructural configuration as in the original dataset. Nevertheless, its defining feature is the inclusion of random temperatures within the interval from 20 °C to 250 °C. It should be noted that the software's constitutive model utilizes linear interpolation to determine the properties for curves that do not align directly on the discrete temperature levels (see Fig 4.3). This selective design choice allows for an investigation of the model's performance across a continuous temperature range rather than at discrete temperature levels. The identical creation procedure ensures that the random distribution of microstructure and temperature is the same in both datasets. Again, it should be noted that any combination of temperature and microstructural configuration used during the training was not used during this testing phase of the ML model.

The results of this study confirm the performance expectations for the ML model when subjected to the random temperature dataset. The ML model here also exhibited good results, achieving RMSE of 1.36 MPa, MSE of 1.9 MPa, and R^2 score of 97.9%. These metrics, although on a different dataset, are in the same performance range as those obtained with the original dataset for the six temperature levels. The findings underscore the ability of the ML model to perform optimally whether the temperature is a fixed value or within a specified range. The accuracy of the predictions was compared against FEA simulations. The findings were consistent with observations made for the six temperature levels.

Combined plot, shown in Fig. 5.10, shows the overall performance of the ML model. Upon analyzing the results, it was found that the maximum error between the values predicted by the ML model and those calculated by FEA simulations, taking into account all predictions, was 9.82 % or 7.1 MPa. The average (mean) error between the predictions of the ML model and the FEA simulations was approximately 0.62 % or 1 MPa. Based on these findings, it can be concluded that the use of only six specific temperatures during the training phase of the ML model does not significantly affect the prediction accuracy for temperatures outside the defined levels but it simplifies the training procedure. Therefore, the ML model demonstrates robustness and generalizability, such that it can be used over the entire temperature interval of interest.

A systematic evaluation of the stress-strain metrics, extrapolated from the ML model and those calculated numerically by FEA, under random temperatures, is shown in Fig. 5.11. As previously noted, the continuing trend of decreasing stress values with temperature increase is confirmed, especially under elevated thermal conditions. This trend line points out the reliability

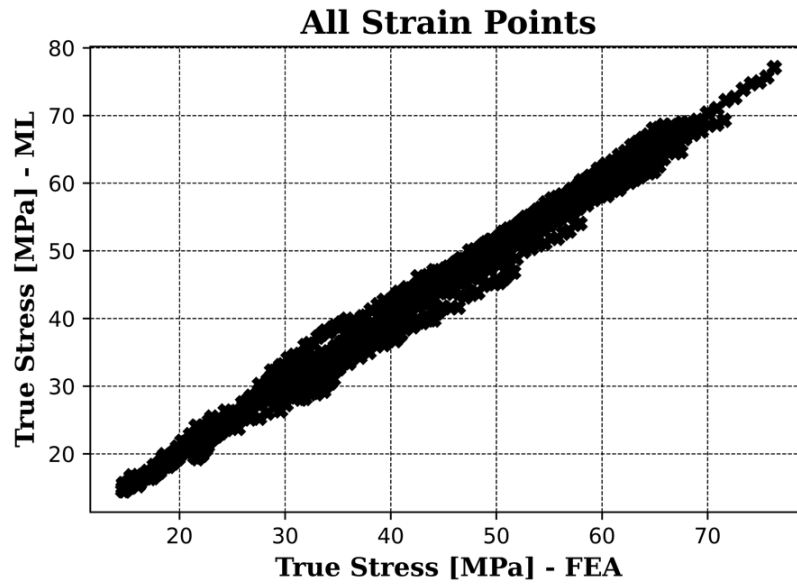


Figure 5.10: Comparison of stress values calculated by FEA with those predicted by the ML model for random temperature levels for different hard phase fractions. The plot includes values from all 20 simulation increments of the true stress-true strain curve

and robustness of the model when considering the complex relationship between stress-strain state and temperature.

In addition, a parallel evaluation is performed to assess the results of the ML model and FEA metrics for varying hard phase fractions, considering all strain points. This comparison is visually shown in Fig. 5.12. As suspected, the trend of increasing stress values with increasing hard phase fraction is evident. This observation supports the ability of the model to handle the complicated interaction between stress-strain state and phase fraction. Again, the maximum stress magnitude is observed for the temperature of around 80 °C and hard phase fraction of around 0.13 which confirms the previous hypothesis that microstructural configuration also affects the stiffness of the multiphase material.

Interestingly, the prediction error of the model remained largely unchanged across the entire temperature range and showed no clear dependence on either temperature or hard phase fraction. However, it is important to note the superposition of values (e.g., overlap of data points at the same coordinates) in both figures, which can obscure the clear presentation of the highest error value. Nevertheless, the underlying trend remains clear and shows the predictive accuracy and reliability of the model.

Again, considering random temperature levels a few statements are confirmed. The ML model effectively accounts for subtle factors, including phase fraction, temperature, and mi-

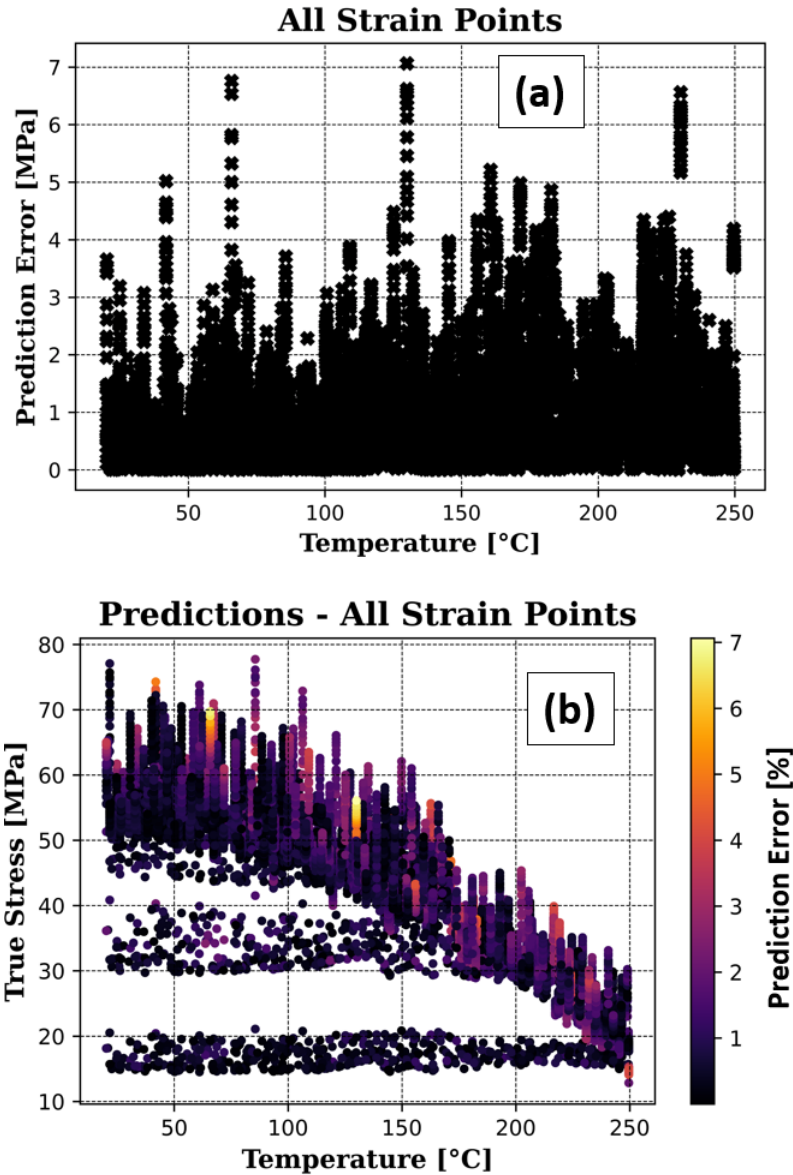


Figure 5.11: Stress values from random temperature dataset calculated by FEA and predicted by the ML model as a function of different temperatures. Plot includes temperatures from all six temperature levels and all 20 simulation increments of the true stress-true strain curve: (a) prediction error vs. temperature, (b) true stress vs. temperature (prediction error is color-coded)

crostructural configuration. The correlation between FEA simulations and model predictions with hard phase fraction or temperature suggests that the 3D CNN accurately captures key parameters like phase arrangement, phase fraction, and temperature.

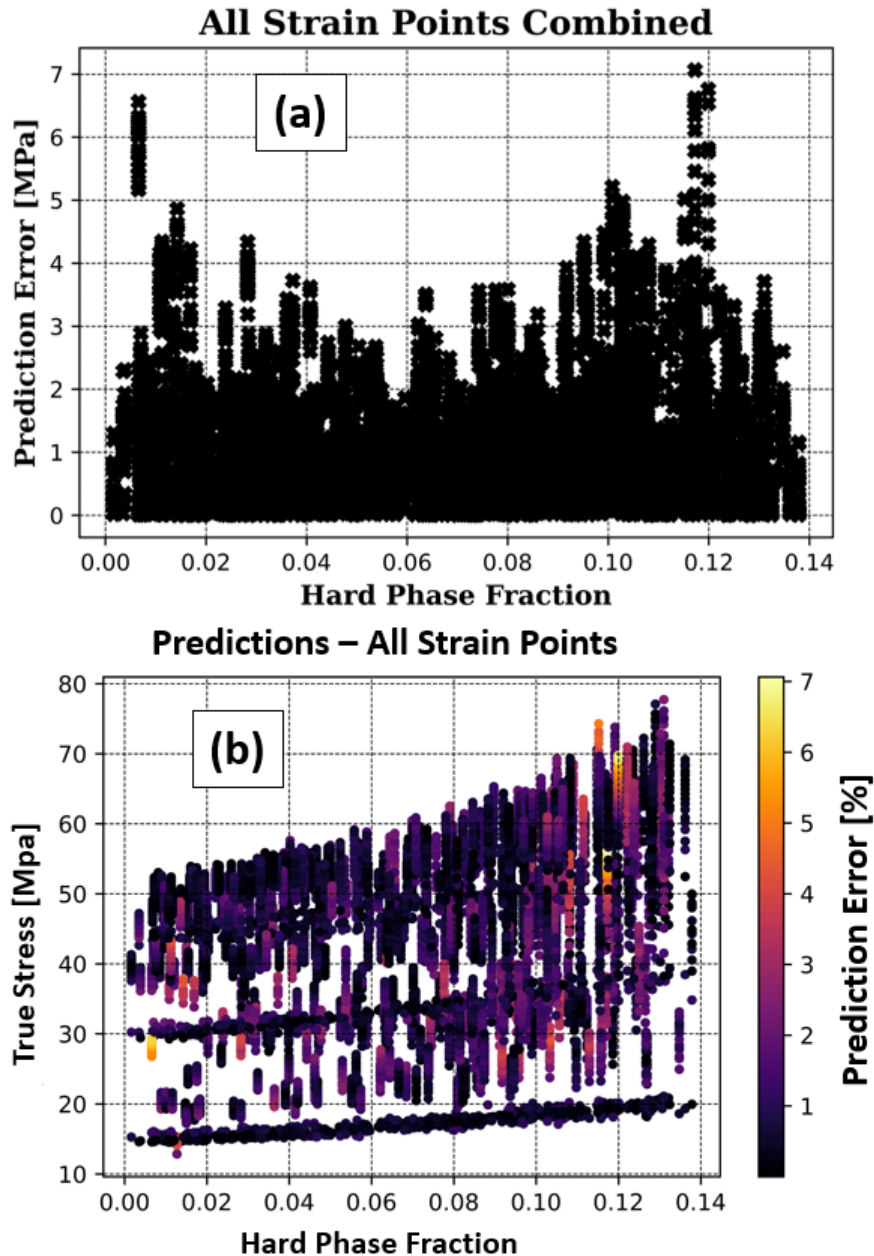


Figure 5.12: Stress values from random temperature dataset calculated by FEA and predicted by the ML model as a function of different phases fraction. Plot includes temperatures from all six temperature levels and all 20 simulation increments of the true stress-true strain curve: (a) prediction error vs. temperature, (b) true stress vs. temperature (prediction error is color-coded)

5.4 Results for the Temperature Increase – Strain Curves

In this Section, an evaluation of the predictive accuracy of the ML model was performed using a test dataset characterized by temperature increase-strain curves. This was a step in validating the effectiveness of the model, and the metrics used to measure accuracy were MSE and RMSE. The MSE and RMSE of the ML model were calculated for the entire test dataset. The resulting

values were $0.004353\text{ }^{\circ}\text{C}$ and $1.9648 \times 10^{-5}\text{ }^{\circ}\text{C}$.

It is important to note that not one combination of microstructural configuration and TQC value employed during the training phase of the ML model was utilized during the testing phase. This approach ensures an unbiased assessment of the ML model's effectiveness. The ML model inference speed was another important observation in this evaluation. The ML model predicted 348 temperature increase-strain curves in about 0.4 seconds. This efficiency is of significant practical importance, especially when compared to a single FEA simulation that takes an average of nine minutes to run.

In examining the predictive capabilities of the ML model against FEA, the focus was placed on the last twelve data points of the projected temperature increase-strain curves. The analysis was performed under various conditions; specifically, different microstructural configurations and TQC values. The detailed graphical representation of this comparison can be found in Fig. 5.13, where four randomly selected curves are displayed. An important observation of the results was the high accuracy with which the ML model reproduced the curves compared to the original curves generated by the FEA methodology. It is important to note that the graph begins at the 8th data point, as the initial eight increments were excluded. This exclusion is due to the minimal temperature increase observed in the first eight increments, which is primarily attributed to stress concentration in the elastic region, leading to a negligible temperature change during these increments. Therefore, the graphs are only focused on the plastic region of the temperature-increase curves which starts at the 8th increment.

Furthermore, it is important to note that the models developed in this research were specifically trained using data from uniaxial tensile tests. Consequently, their use under different BC should be done carefully. Although the models demonstrate promising predictive capabilities within the constraints of their training parameters, applying them to scenarios outside these conditions was not tested and may result in inaccurate predictions. This highlights the necessity of designing future ML models that are specifically tailored to the BC they are intended for.

As can be seen from Fig. 5.13, the change in TQC values has no significant effect on the temperature increase. Upon closer inspection, it can be seen that the increase in temperature is most affected by an increase in the hard phase fraction. Interestingly, the complicated interaction and spatial distribution of the hard and soft phases within the RVE also contribute to the temperature increase. However, this aspect cannot be studied in detail due to the stochastic nature of configuration generation process. Each generated configuration is inherently random

and unique, and thus poses a significant challenge in determining its precise influence on the temperature increase. Current methods do not yet provide a sufficiently reliable approach to accurately investigate this influence. Nevertheless, it is found that the curves replicated by the ML model exhibited a very good agreement with the curves calculated by the FEA methodology. This similarity underlines the validity of the ML model as an alternative to the conventional FEA approach. This means that the ML model successfully accounts for the distribution of hard and soft phases within the microstructure and, consequently, the temperature increase.

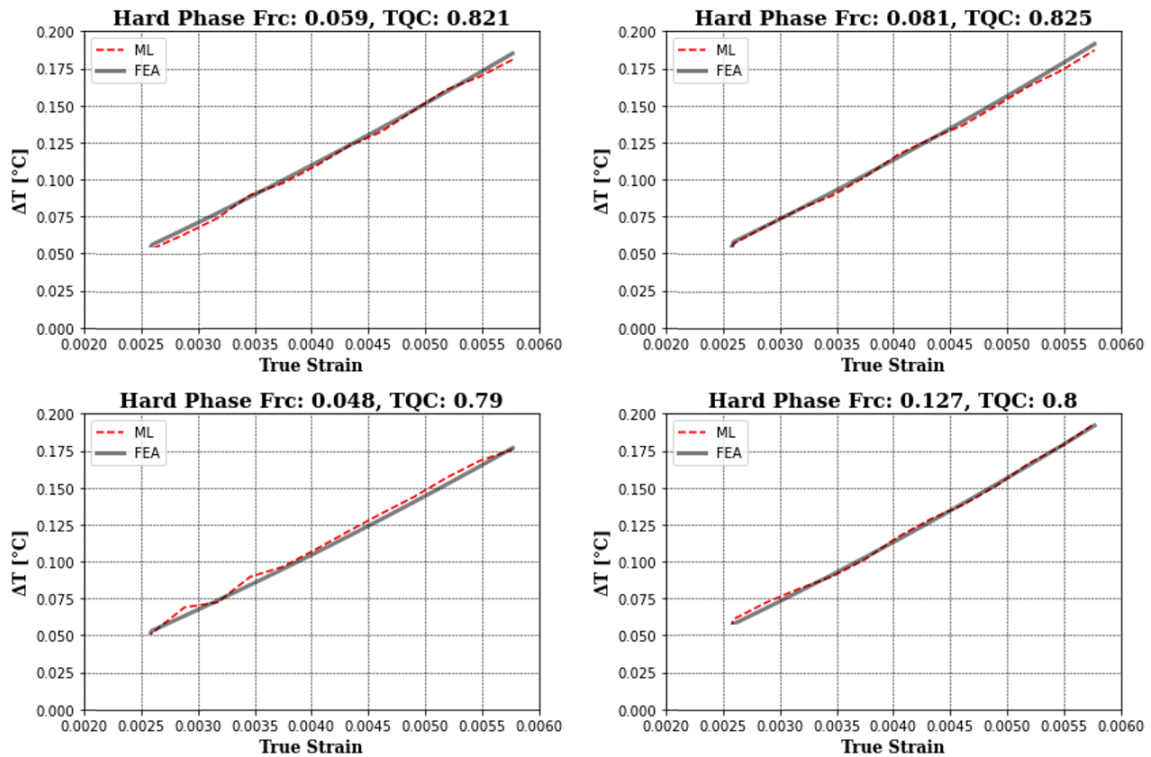


Figure 5.13: Visualization of temperature increase-strain curves predicted by the ML model and simulated by FEA (TQC of the last simulation increment is shown).

An analysis was performed to verify the predictive accuracy of the ML model across all stress points within the intended simulation interval. This approach also provided a more sophisticated understanding of the performance of the model compared to FEA simulations. These comparative outcomes have been visually represented in Fig. 5.14. Throughout the interval of temperature increase, the predictive accuracy of the ML model remained consistent. Another observation was the lack of significant variation in the prediction error across different intervals. Careful examination of the prediction error for individual strain points also revealed that the range of error was relatively small. The maximum error value did not exceed 6.5%.

In the subsequent phase of the analysis, the predictions of the ML model were put to the

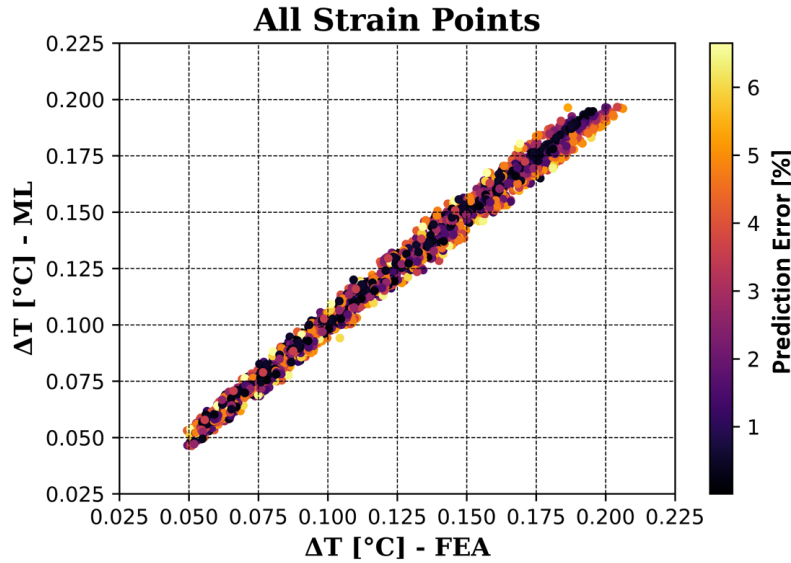


Figure 5.14: Visualization of temperature increase values calculated by FEA and values predicted by the ML model. The diagram contains temperature increase-strain points from all simulation increments – The percentage prediction error is color-coded.

test in comparison with the FEA simulations. The temperature increase across the entire simulation interval ranged from 0.04 °C to 0.2 °C. Furthermore, the maximum error in temperature increase did not exceed 0.012 °C, and indicates the accuracy of the model in predicting temperature. It is important to note that this maximum error is associated with a higher temperature increase, which is due to the previously mentioned maximum prediction error of about 6.5%. As a concluding part of this investigation, the average error in temperature increase prediction was evaluated. The calculated value was found to be $5.87 \cdot 10^{-5}$ °C.

In evaluating the discrepancy between the predictions of the FEA simulations and the ML predictions, an additional investigation was conducted. In this analysis, all TQC values within the specified interval were considered, and each strain point was taken into account. The results are shown visually in Figs. 5.15 and 5.16. One might suspect a correlation between temperature increase and a change (e.g., increase) in TQC value, but as the results show, this correlation is relatively low. The data not only confirmed the low correlation between temperature increase and TQC value, but also confirmed that the prediction error between FEA simulations and the ML model is not related to the TQC value.

Moreover, the prediction discrepancy between the ML model and FEA simulations was shown with respect to certain intervals of the fraction of the hard phase, as shown in Figs. 5.17 and 5.18. The temperature increase tends to increase slightly as higher fractions of the hard phase

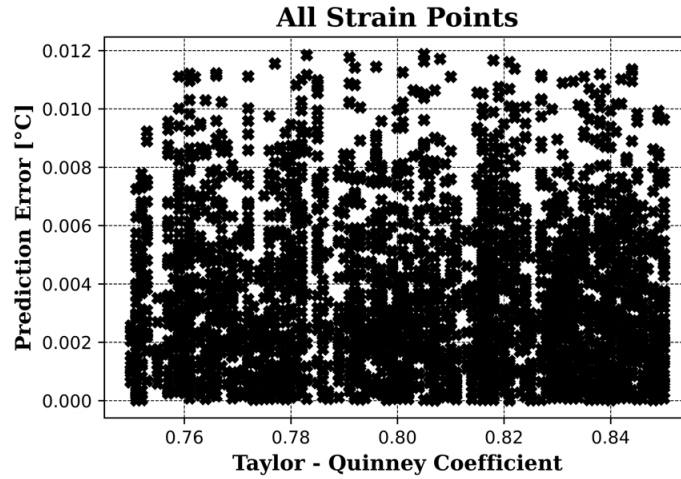


Figure 5.15: Prediction error compared to TQC value. The plot includes values from the all 12 simulation increments. The actual TQC value (β) for the last simulation increment is displayed.

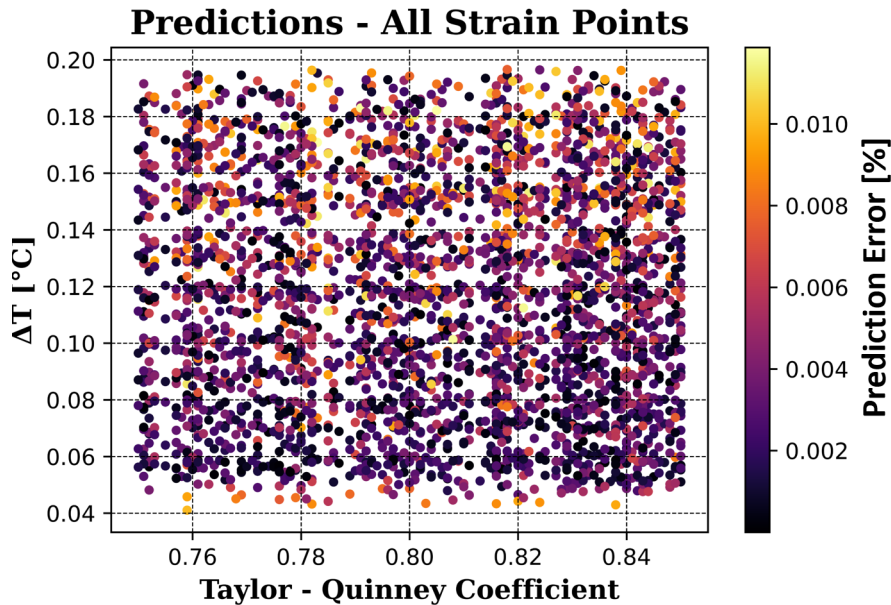


Figure 5.16: Visualization of temperature increase values calculated by FEA for various TQC values including all 12 simulation increments and complete TQC range – The percent prediction error is color-coded, the actual TQC (β) for the last simulation increment is displayed.

are approached. It appears that the temperature increase is also related to the microstructural configuration within the RVE. Of particular note, the most pronounced temperature increases are observed at hard phase fractions of 0.085, 0.118, and 0.135 instead of 0.15. As before, this observation could be attributed to the random scattering of the phases within the RVE, which inadvertently led to the maximum temperature increases. Thus, the highest values of plastic strain coincide with these particular hard phase fractions.

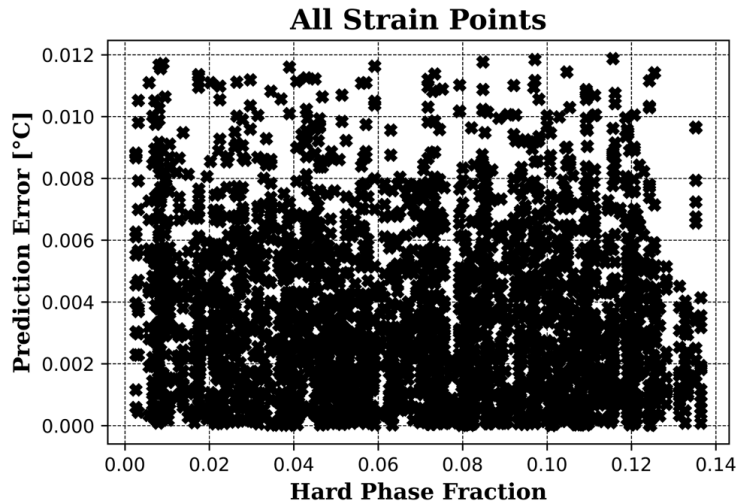


Figure 5.17: Prediction error for the proportion of hard phase. The plot includes values from all 12 simulation increments.

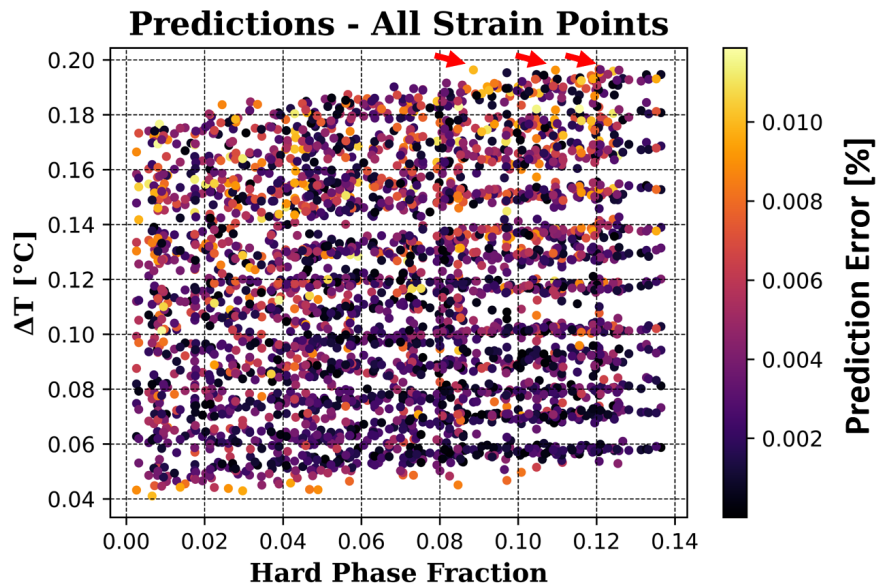


Figure 5.18: Visualization of the values calculated by FEA and those predicted by the ML model for the temperature increase at different proportions of the hard phase. All 12 simulation increments are included – The percentage prediction error is color-coded. The arrows indicate the highest temperature increase.

The ML model employed offers a significant advantage: it captures not only the TQC value and phase fractions but also the microstructural configuration. Finally, it is important to note that the prediction error between FEA simulations and the ML model was found to be independent of the hard phase fraction. This independence indicates that the adopted ML model used has some robustness and provides consistent prediction quality regardless of the phase fraction. The

detailed investigation of the prediction discrepancy between the FEA simulations and the ML model, considering all the TQC values, emphasizes the inherent strengths of the ML model in capturing complex relationships in a system. Furthermore, it points out the potential and adaptability of ML in understanding and predicting complicated material behavior based on multiparametric inputs.

5.5 Influence of Phases Distribution – Random Temperature Levels Dataset

Although it is challenging to precisely quantify the spatial distribution of phases within the RVEs, an attempt is made here by analyzing the relative positions and standard deviations of the CoGs for both the hard and soft phases. The distance between these CoGs and standard deviations shows the uniformity of phase distribution and its effect on the mechanical response. The following sections discuss the observed trends and correlations based on the calculated CoG distances for various hard and soft phase configurations.

Fig. 5.19 illustrates the effect of varying distances between CoGs of hard and soft phases within different RVEs. These CoG positions reflect the distribution uniformity of the hard phase. For each RVE, global CoGs for both phases were calculated, and the distances between these CoGs were measured. Each strain point is depicted in the graph. Generally, a higher hard phase fraction corresponds to a shorter CoG distance. However, some RVEs exhibit much larger CoG distances, often due to a very low hard phase fraction, where few small particles are dispersed far from the RVE center. This dispersion causes the global CoG of the hard phase to deviate significantly, increasing the CoG distance. Typically, both phase CoGs are centered, as DREAM.3D phase generation follows a normal distribution. The soft phase, having a higher fraction, usually has its CoG near the RVE's center. Conversely, an increase in hard phase fraction tends to reduce the CoG distance.

Reexamining Fig. 5.19, the same conclusions could be drawn again. Higher stress values are associated with a higher proportion of the hard phase. Furthermore, no clear connection exists between the prediction error and the CoG distance. It is consistently evident that the predominant factor affecting stress magnitude is the fraction of the hard phase.

Fig. 5.20 shows the distance between the CoGs of the hard phase and the RVE center. Similar observations can be made as in Fig. 5.19. Additionally, it is apparent that the CoG of the soft

phase is near the RVE's CoG center. This is reasonable given the significantly higher fraction of the soft phase compared to the hard phase, as previously mentioned.

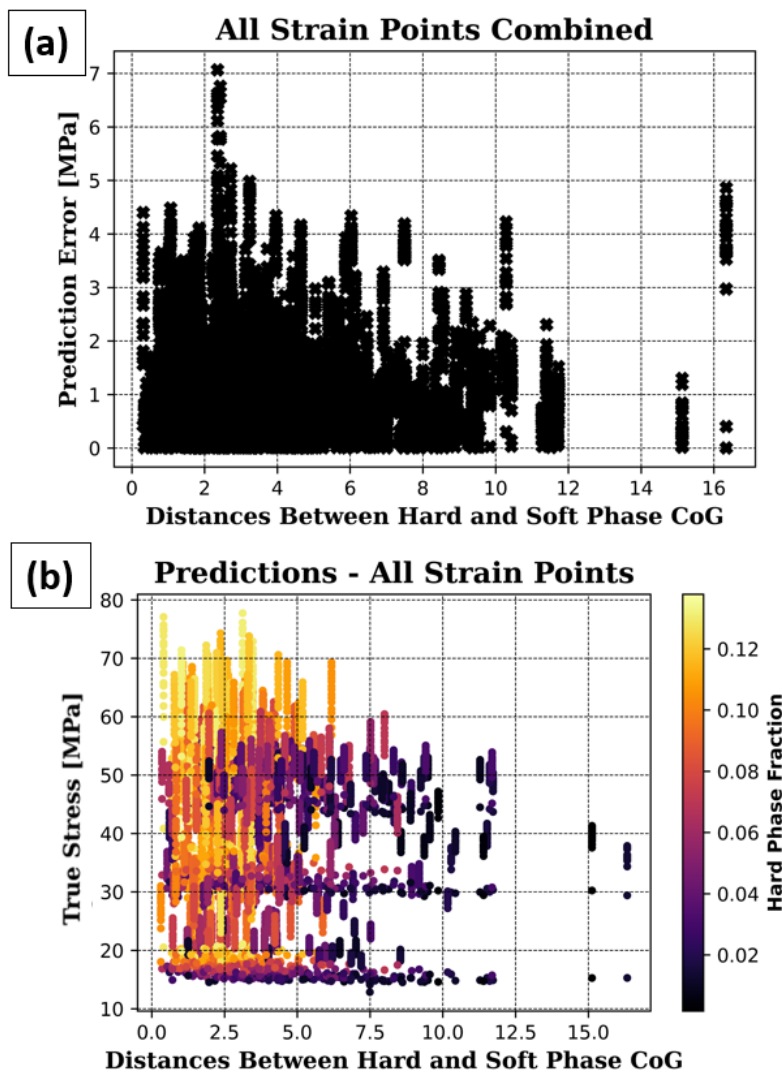


Figure 5.19: Distance between the CoGs of the hard and soft phases for all 20 points on the stress-strain curve: (a) including prediction error, and (b) showing the true stress.

A study was performed to evaluate the impact of the standard deviation of distances between all components in both the soft and hard phases of the RVEs from the center, as shown in Figs. 5.21 and 5.22. The primary objective was to demonstrate that data dispersion variations affect the outcomes. These figures indicate that there is no significant correlation between the error and the proportion of either the hard phase or the soft phase, regardless of the standard deviation values.

The majority of the standard deviation values for the soft phase are mostly clustered around 3.62, with extreme values of 3.75 and 3.45. For the hard phase, standard deviation values are

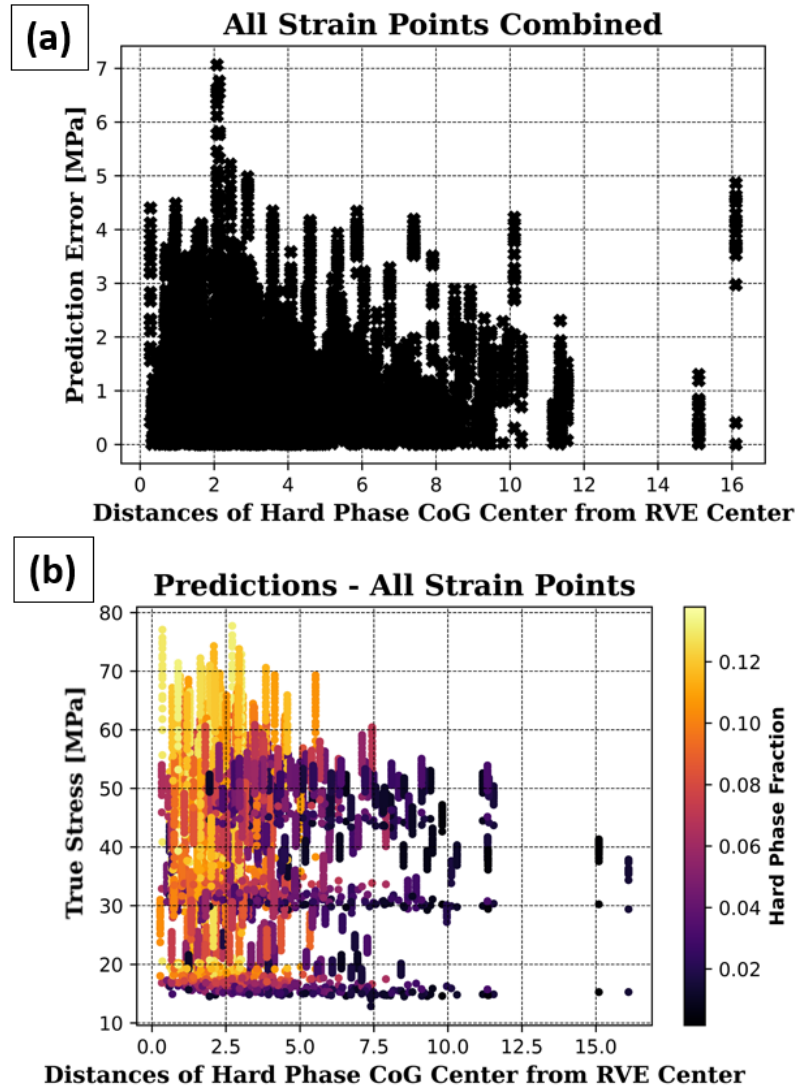


Figure 5.20: Distance between the CoGs of the hard phase from RVE center for all 20 points on the stress-strain curve: (a) including prediction error, and (b) showing the true stress.

concentrated around 3.75, with a minimum of 0.2 and a maximum of 5.85. This variability in the hard phase supports the earlier conclusion that the CoG of the hard phase can vary widely due to the smaller number of particles and their stochastic distribution.

Fig. 5.23 presents a scatterplot illustrating the relationships between various variables, including CoG distances of the hard phase from the center, standard deviation, mean distance of the hard and soft phases from the center, hard phase fractions, and prediction error. For calculating the mean distance, the CoGs of the individual elements within the RVE are determined for each phase, followed by the calculation of the mean distance. The analysis reveals an important pattern: the standard deviation of CoG distances and the mean distance of the hard phase are predominantly clustered within a narrow range around a specific value. Only a small proportion

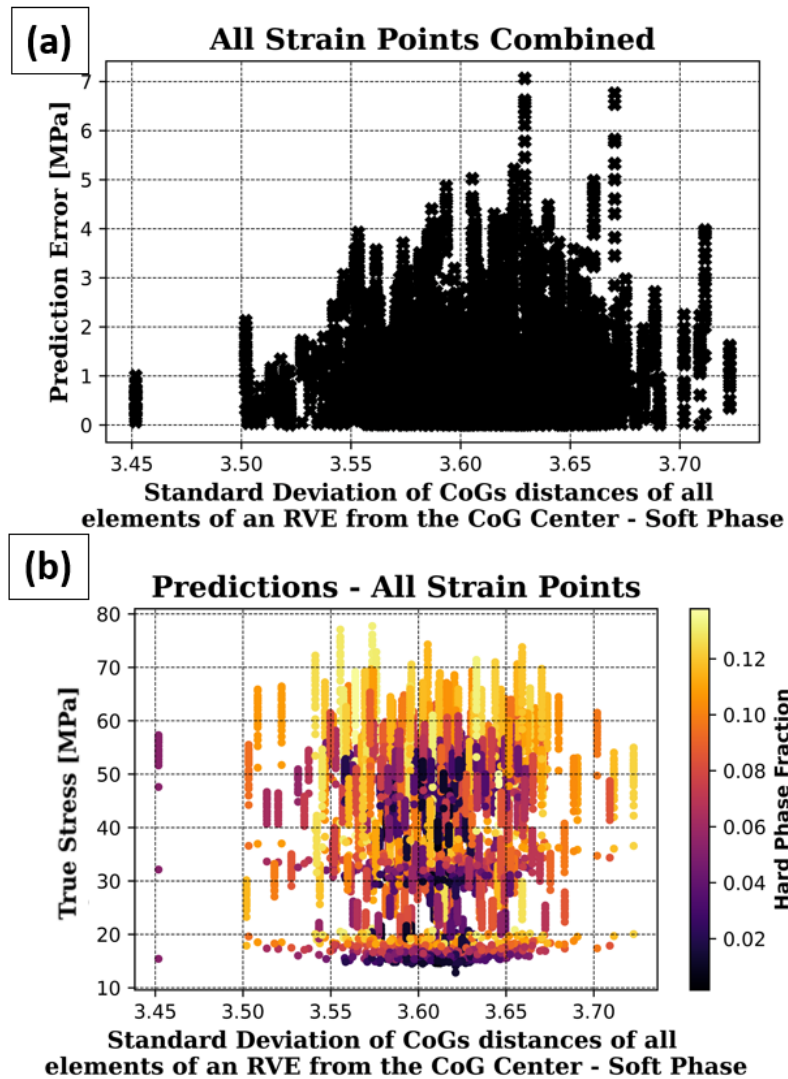


Figure 5.21: The standard deviation of the center of gravity distances for all elements of an RVE from the CoG center across all RVEs for all 20 points of the stress-strain curve for the soft phase is depicted as follows: (a) in relation to the prediction error, and (b) in relation to the true stress.

of RVEs deviate from this range, mainly those with very small hard phase fractions. This pattern corroborates the previous conclusions of a normal distribution of phases within the RVE. The CoG distances are generally centered around smaller values, approximately 3 mm, though some RVEs show higher values up to 15 mm, which mainly correspond to smaller fractions of the hard phase.

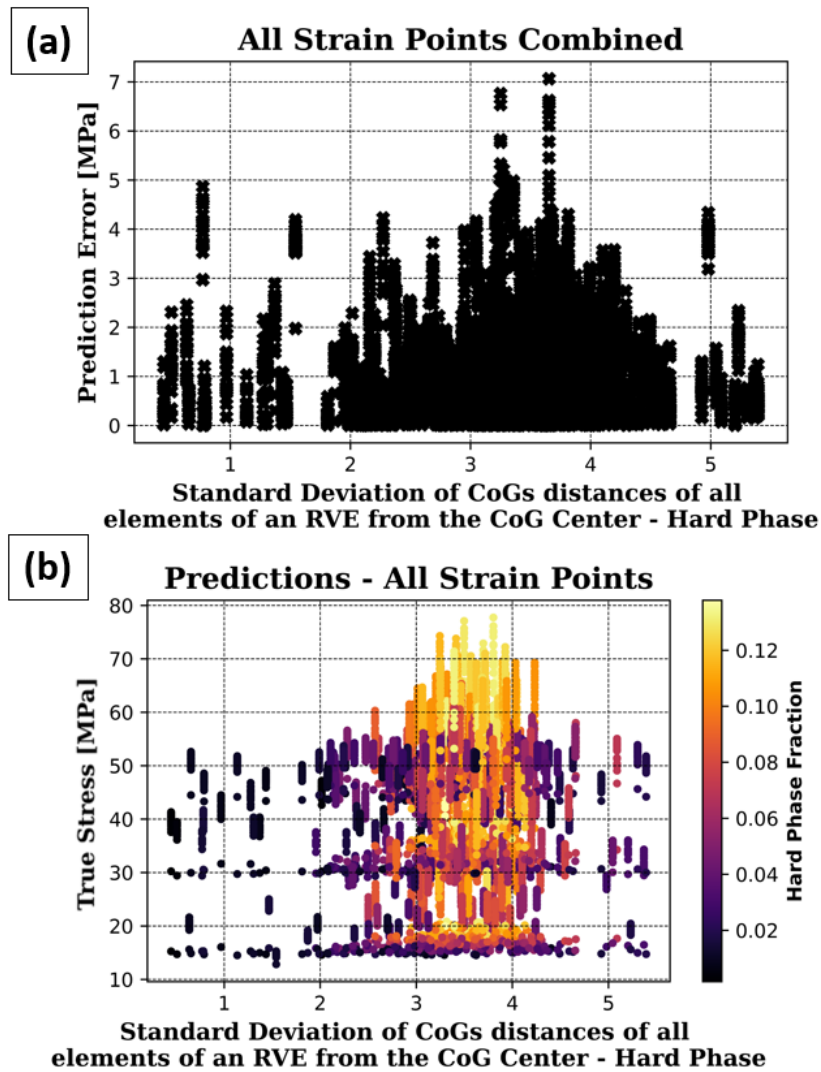


Figure 5.22: The standard deviation of the center of gravity distances for all elements of an RVE from the CoG center across all RVEs for all 20 points of the stress-strain curve for the hard phase is depicted as follows: (a) in relation to the prediction error, and (b) in relation to the true stress.

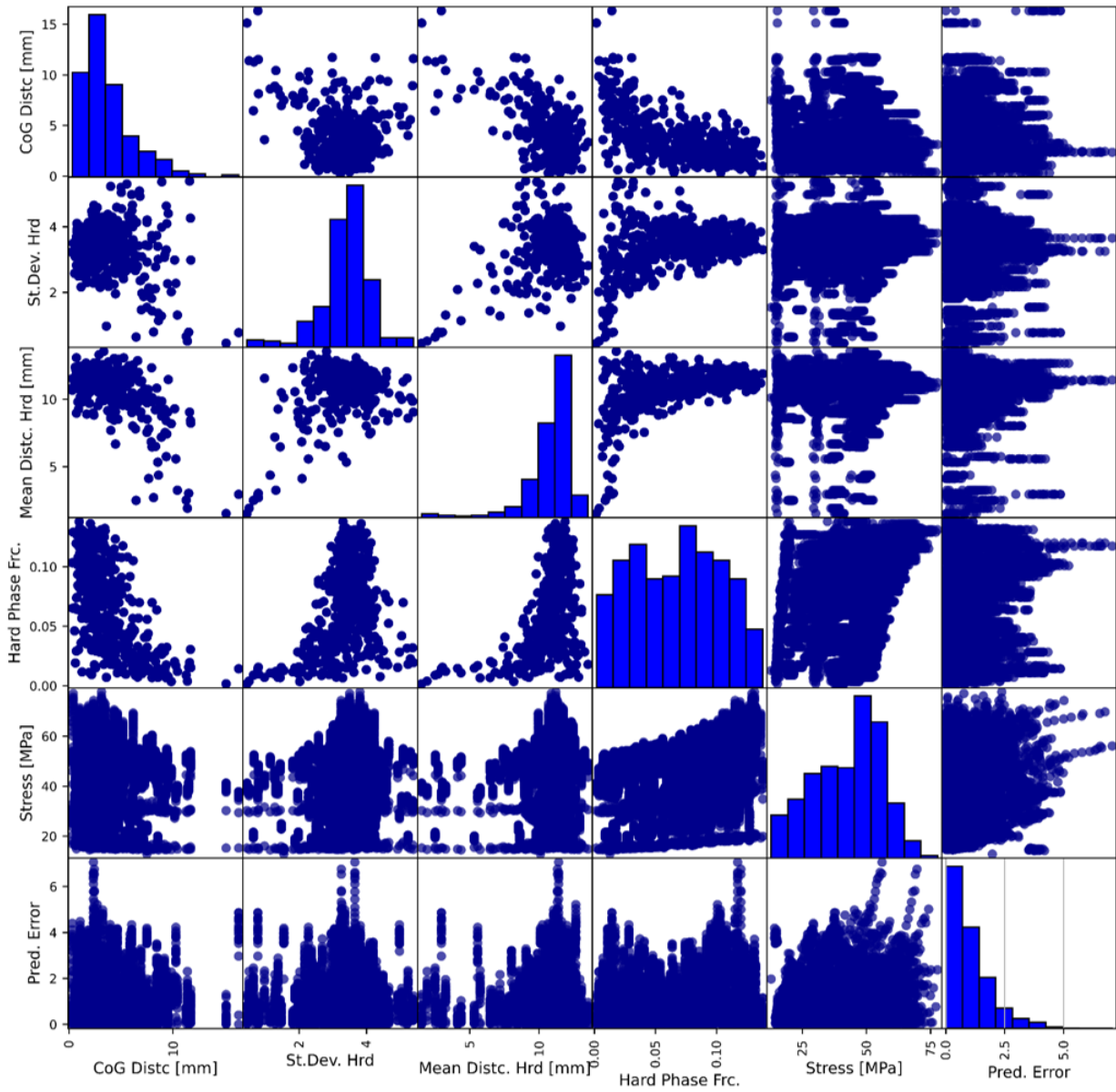


Figure 5.23: Scatter matrix of all 20 points of the stress-strain curve for all RVEs, showing the CoG distances of the hard phase from the center, the standard deviation, the mean distances of the hard and soft phases from the center, the hard phase fractions, and the prediction error.

5.6 Influence of Phases Distribution – Temperature Increase Strain Curves

For the temperature increase-strain curves prediction, similar conclusions could be drawn again. Fig. 5.24 demonstrates the impact of varying distances between CoGs of hard and soft phase within different RVEs. These CoG positions indicate the uniformity of the hard phase distribution. For each RVE, global CoGs were computed for both the hard and soft phases, and the distances between these CoGs were measured, on the same principle as for the stress prediction. Each strain point is represented in the graph. Again, a higher hard phase fraction correlates with a shorter CoG distance. However, a small amount of RVEs show much larger CoG distances than others. This can be again attributed to situations where there is a very low hard phase fraction, resulting in a few small particles being scattered far from the RVE center.

Reevaluating Fig. 5.24 (b) reaffirms a previously made conclusion: a greater increase in temperature correlates with a higher fraction of the hard phase. Additionally, there is no apparent relationship between the prediction error and the CoG distance. Once more, it is evident that the primary factor influencing the temperature increase is the fraction of the hard phase.

In Fig. 5.25, the distance between the CoGs of the hard phase from the RVE center is illustrated. Similar conclusions as before could be drawn again: a greater increase in temperature correlates with a higher fraction of the hard phase. Additionally, it is evident that the CoG of the soft phase is proximate to the CoG center of the RVE. This observation is logical given the significantly higher fraction of the soft phase compared to the hard phase, as previously discussed.

As for the TQC dataset, research was conducted to assess the effect of the standard deviation of the distances between all components in both the soft and hard phases of the RVEs from the center, as shown in Figs. 5.26 and 5.27. The primary aim was to show that variations in data dispersion impact the results. Figs. 5.26 and 5.27 illustrate that there is no substantial correlation between the error and the proportion of the hard phase or the soft phase, irrespective of whether the standard deviation values are high or low.

Similar observations could be drawn again. The majority of the standard deviation values for the soft phase are clustered tightly around the value of 3.62. The extreme standard deviation values of the CoG are 3.71 and 3.45, respectively. For the hard phase, Fig. 5.27 shows that the standard deviation values are concentrated around 3.5, with the minimum and maximum being

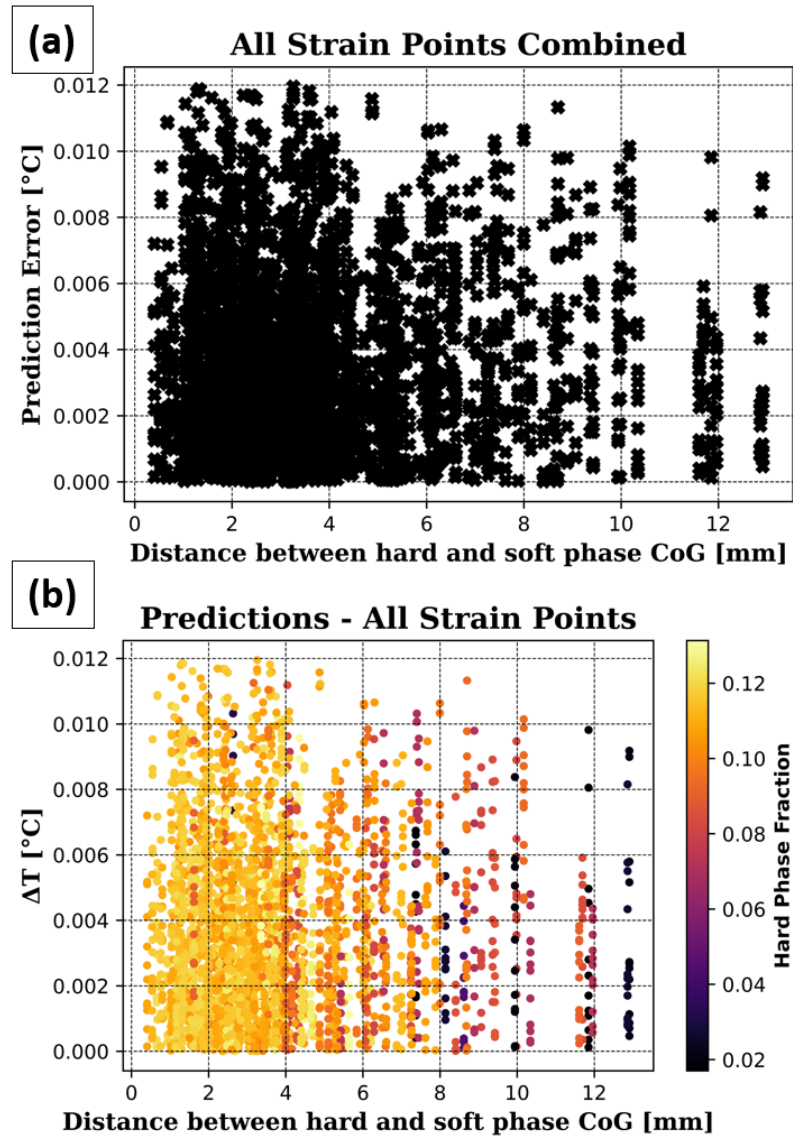


Figure 5.24: Distance between the CoGs of the hard and soft phases for all 12 points on the temperature increase curve: (a) including prediction error, and (b) showing the temperature increase.

0.25 and 5.80, respectively. This supports the earlier conclusion that the CoG of the hard phase can vary widely due to the smaller number of particles and their stochastic distribution.

Fig. 5.28 displays the relationship between various variables through a scatterplot including aspects such as the CoG distances of the hard phase from the center, the standard deviation, the mean distance of the hard and soft phases from the center, the hard phase fractions, and the prediction error. It is important to note that for calculating the mean distance, the CoGs of the individual elements within the RVE are determined for each phase, and then the mean distance is calculated. Analyzing the data reveals a clear pattern: the standard deviation of the CoG distances and the mean distance of the hard phase are mainly clustered within a narrow range

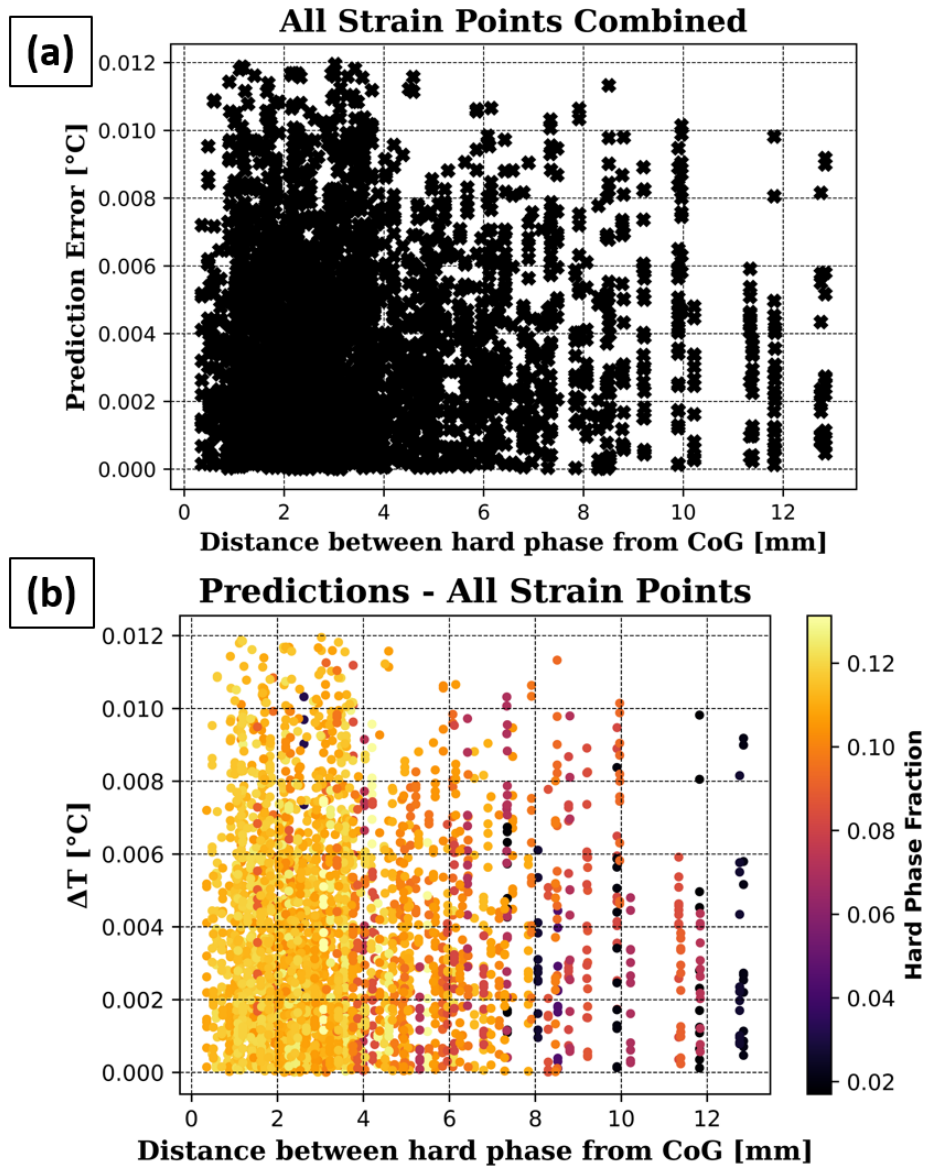


Figure 5.25: Distance between the CoGs of the hard phase from RVE center for all 12 points on the temperature increase curve: (a) including prediction error and, (b) showing the temperature increase.

around a specific value. Only a small fraction of RVEs deviate from this range, particularly those with very small hard phase fractions. This pattern supports the DREAM.3D settings of a normal distribution of phases within the RVE. The CoG distances are generally distributed around smaller values, approximately 3 mm, although some RVEs exhibit higher values up to 15 mm, which predominantly correlate with smaller fractions of the hard phase.

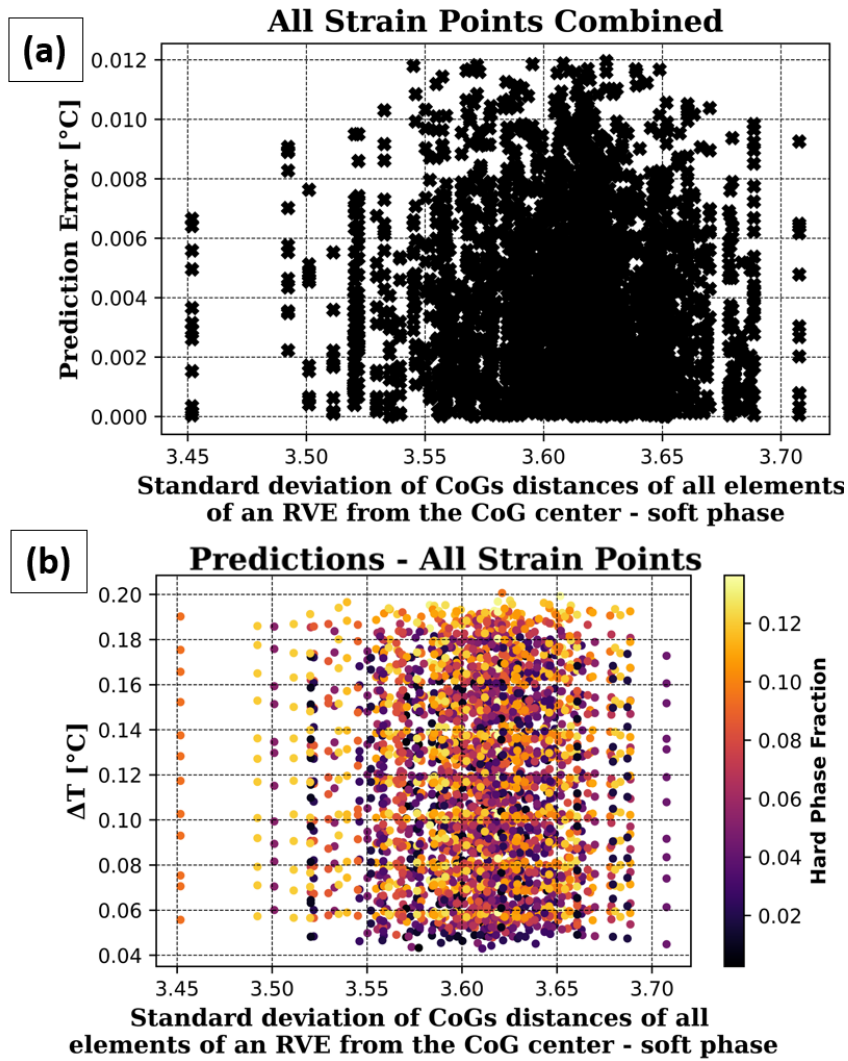


Figure 5.26: The standard deviation of the center of gravity distances for all elements of an RVE from the center of gravity center across all RVEs for all 12 points of the temperature increase curve for the soft phase is depicted as follows: (a) in relation to the prediction error, and (b) in relation to the temperature increase.

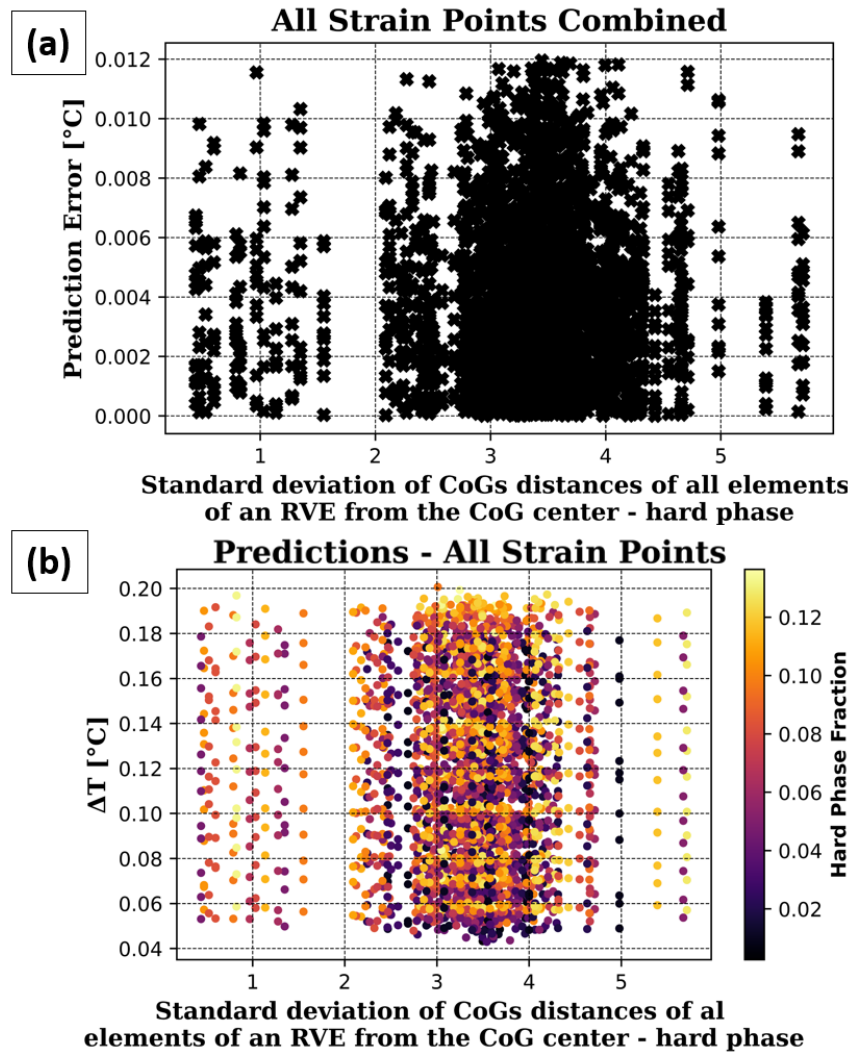


Figure 5.27: The standard deviation of the center of gravity distances for all elements of an RVE from the center of gravity center across all RVEs for all 12 points of the temperature increase curve for the hard phase is depicted as follows: (a) in relation to the prediction error, and (b) in relation to the temperature increase.

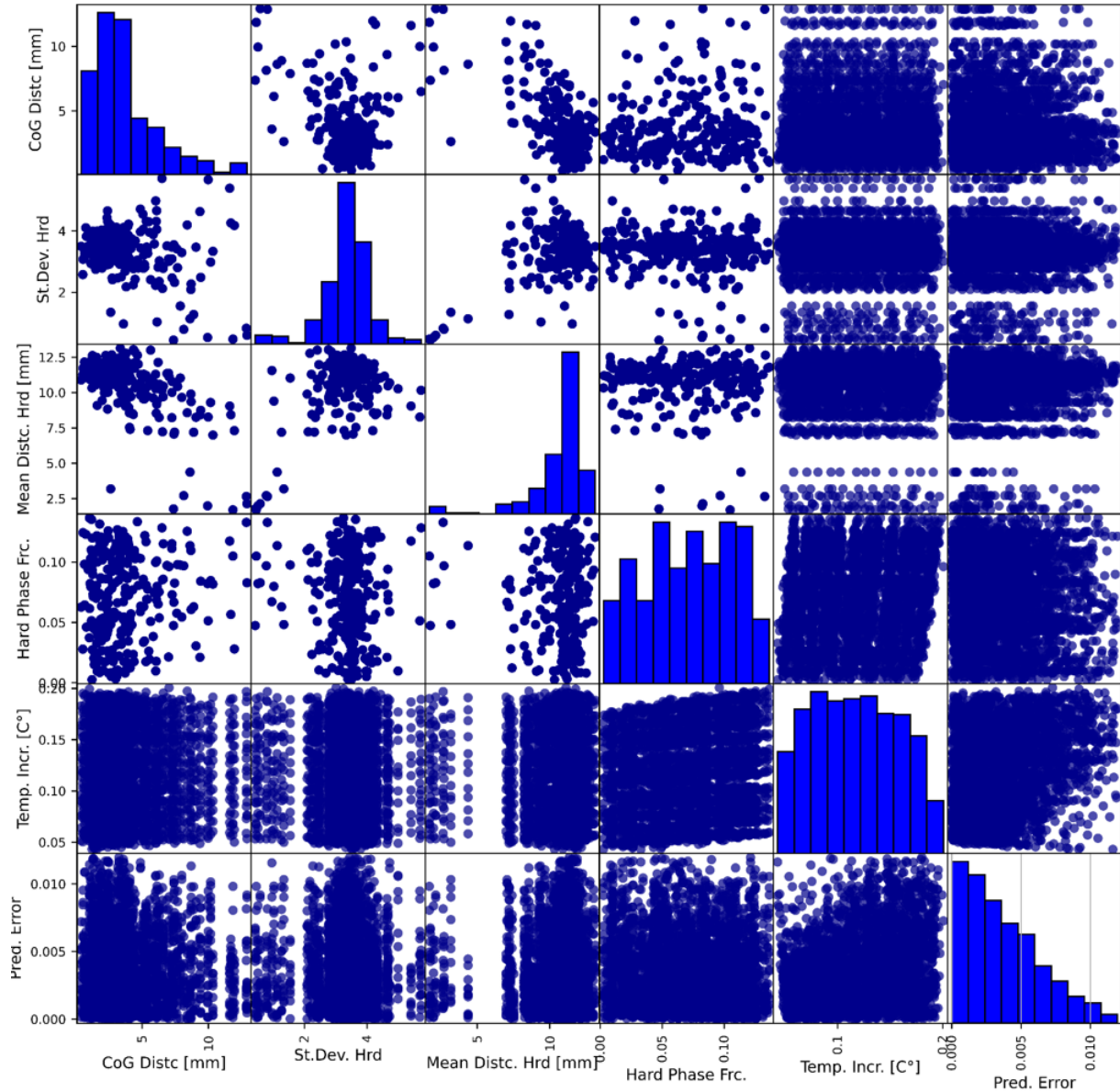


Figure 5.28: Scatter matrix of all 12 points of the temperature increase curve for all RVEs, showing the CoG distances of the hard phase from the center, the standard deviation, the mean distances of the hard and soft phases from the center, the hard phase fractions, and the prediction error.

Chapter 6

Conclusion

The investigation conducted in the present study has led to the confirmation of the central hypothesis that the plastic deformation-induced heat generation and the temperature-dependent stress-strain curves based on microstructural configuration could be determined by ML methods. This validation underpins the potential of ML in the field of computational materials science and engineering mechanics and its potential to replace traditional calculation methods.

The two ML models examined have shown quite good performance and have only minor prediction errors. The first ML model, which considers temperature-dependent stress-strain curves over six distinct temperature intervals, also provided very good results. The ML model showed an RMSE of 0.99 MPa and an MSE of 0.98 MPa. The maximum error for this model was 7.8 MPa or 10.12 %, while the average error was 0.7 MPa or in average 0.65 %, much lower than the maximum error. The performance consistency of this model is also demonstrated. Incorporating a random temperature dataset the analysis of the model, it was observed that the performance remained consistently high, reflecting its robustness and versatility. These observations provide evidence that the precision and reliability of these models are suitable for adoption in both industry and academic research as well as the potential of ML models in complex real-world applications. This model showed very good computational efficiency making single prediction in about 0.001 s.

The second model incorporated the phenomenon of temperature increase during plastic deformation. It attained an RMSE of 0.004353 °C, and an MSE of 1.9648×10^{-5} °C. These error metrics are quite low, suggesting the very well precision of the model. The maximum error reported by this model was 0.012 °C, a value considerably larger than the average error, which was much smaller at 5.87×10^{-5} °C. It is noteworthy that these error magnitudes were analyzed

over a temperature range of 0.04 °C to 0.2 °C, demonstrating the robustness of the model over this interval. Again, the model showed very good computational efficiency making a single prediction in about 0.001 s.

A detailed investigation of the effects of phase fraction on prediction accuracy revealed that the amount of hard phase – the material phase with increased resistance to deformation – directly affects both the thermal and mechanical characteristics of the RVE under plastic deformation. In particular, an increased fraction of hard phase enhances the temperature increase during plastic deformation and amplifies the true stress-true strain curves. The underlying cause can be attributed to the contribution of the hard phase to increased overall stiffness in the RVE configuration. The increased stiffness results in higher true stress for the same strain amount, which leads to a more elevated stress-strain curves.

Upon examining the effect of temperature on stress-strain curves, it was found to be the most important factor affecting these curves. A range of temperatures was incorporated into the procedure. The observations confirmed a significant decrease in average stress values with increasing temperature. This pattern is consistent with conventional materials science theories that assume that increased energy at higher temperatures allows easier dislocation movement, thus lowering stress values.

An in-depth investigation was also conducted to understand the effects of the TQC value on the heat generated, focusing on the relationship between plastic strain and temperature increase. Surprisingly, within the current TQC range, the change in TQC value was not found to significantly influence the temperature increase. Instead, the dataset revealed that the microstructure configuration and hard phase fraction plays a much more critical role in the temperature increase under the given plastic strain. Despite its importance, a detailed study of microstructure configuration was hindered by its random nature, which prevents a clear deterministic understanding of its role.

Furthermore, the analysis of both dataset reveals that the distribution of hard and soft phases significantly impacts the CoG distances within the RVEs. A higher fraction of the hard phase correlates with shorter CoG distances, primarily due to the clustering of hard phase particles. The data indicates that the primary factor influencing temperature increase is the fraction of the hard phase, with no significant relationship between CoG distance and prediction error. Additionally, the standard deviation of CoG distances supports the conclusion that phase distribution follows a normal pattern, with the soft phase showing more central CoG positioning due to its

higher fraction. This study reaffirms the importance of phase distribution in understanding material behavior under varying temperature conditions. The findings from the stress-strain dataset further confirm these conclusions, demonstrating consistent trends between phase distribution, CoG distances, and mechanical response across varying stress levels.

This study relies on numerical simulations that reflect the parameters of a macroscopic uniaxial tensile test. In these simulations, only a minimal amount of plastic strain is integrated, to reflect the characteristic material deformation during loading. The tightly controlled study design thus facilitated the generation of robust, reliable data. However, these exact conditions inherently limit the scope of applicability. The ML model, which was developed and tested within the defined parameters of this study, should be cautiously employed outside these specific BC. Despite the success of the model under the tested conditions, extending its application could potentially lead to less reliable results due to its specific nature. Therefore, this study urges discretion in applying the model to different scenarios or BC.

Exploration of various BC, particularly shear loading, offers a promising direction for future work. Shear loading's potential impact on material behavior may provide significant new insights in real-world applications. In addition, with greater computational resources, investigations could be extended to scenarios with greater plastic strain. The improved accuracy of such models could significantly improve the understanding of material responses. Finally, conducting a study on a real life material with accurate material properties and microstructure configurations would provide invaluable data. This approach could significantly enrich the current theoretical knowledge base and bring it one step closer to practical applications of this research.

Bibliography

- [1] P.W. Bridgman. The thermodynamics of plastic deformation and generalized entropy. *Reviews of Modern Physics*, 22(1):56, 1950.
- [2] J.F. Nicholas. The dissipation of energy during plastic deformation. *Acta Metallurgica*, 7(8):544–548, 1959.
- [3] B. Behrens, A. Chugreev, F. Bohne, and R. Lorenz. Approach for modelling the Taylor-Quinney coefficient of high strength steels. *Procedia Manufacturing*, 29:464–471, 2019.
- [4] M. B. Bever, D. L. Holt, and A. L. Titchener. The stored energy of cold work. *Progress in materials science*, 17:5–177, 1973.
- [5] A. Rusinek and J.R. Klepaczko. Experiments on heat generated during plastic deformation and stored energy for TRIP steels. *Materials & Design*, 30(1):35–48, 2009.
- [6] G. Ravichandran, A. J. Rosakis, J. Hodowany, and P. Rosakis. On the conversion of plastic work into heat during high-strain-rate deformation. In *AIP conference proceedings*, volume 620, pages 557–562. American Institute of Physics, 2002.
- [7] R. Kositski and D. Mordehai. Employing molecular dynamics to shed light on the microstructural origins of the Taylor-Quinney coefficient. *Acta Materialia*, 205:116511, 2021.
- [8] D. G. Gonzalez, R. Zaera, and A. Arias. A hyperelastic-thermoviscoplastic constitutive model for semi-crystalline polymers: Application to peek under dynamic loading conditions. *International Journal of Plasticity*, 88:27–52, 2017.
- [9] R. Zaera, J. Rodríguez-Martínez, and D Rittel. On the Taylor–Quinney coefficient in dynamically phase transforming materials. application to 304 stainless steel. *International Journal of Plasticity*, 40:185–201, 2013.

- [10] V.E. Rubtsov and A.V. Kolubaev. Effect of heat generation due to plastic deformation on behavior of surface-layer material during sliding. *Journal of Friction and Wear*, 30(5):324–328, 2009.
- [11] T. Bjerke, Z. Li, and J. Lambros. Role of plasticity in heat generation during high rate deformation and fracture of polycarbonate. *International Journal of Plasticity*, 18(4):549–567, 2002.
- [12] B. Li, P.C. Clapp, J.A. Rifkin, and X.M. Zhang. Molecular dynamics calculation of heat dissipation during sliding friction. *International Journal of Heat and Mass Transfer*, 46(1):37–43, 2003.
- [13] D. Brennhaugen, K. Georgarakis, Y. Yokoyama, K.S. Nakayama, L. Arnberg, and R. E. Aune. Probing heat generation during tensile plastic deformation of a bulk metallic glass at cryogenic temperature. *Scientific Reports*, 8(1):1–10, 2018.
- [14] A.S. Alghamdi, I. A. Ashcroft, M. Song, and D. Cai. Nanoparticle type effects on heat generation during the plastic deformation of polyethylene nanocomposites. *Polymer Testing*, 32(8):1502–1510, 2013.
- [15] A. Benaarbia, G. Chatzigeorgiou, B. Kiefer, and F. Meraghni. A fully coupled thermo-viscoelastic-viscoplastic-damage framework to study the cyclic variability of the Taylor-Quinney coefficient for semi-crystalline polymers. *International Journal of Mechanical Sciences*, 163:105128, 2019.
- [16] G.C. Soares and M. Hokka. The Taylor–Quinney coefficients and strain hardening of commercially pure titanium, iron, copper, and tin in high rate compression. *International Journal of Impact Engineering*, 156:103940, 2021.
- [17] L. Charles K.C. and C. A. Bronkhorst. Thermomechanical conversion in metals: dislocation plasticity model evaluation of the Taylor-Quinney coefficient. *Acta Materialia*, 202:170–180, 2021.
- [18] A. Bartels, T. Bartel, M. Canadija, and J. Mosler. On the thermomechanical coupling in dissipative materials: a variational approach for generalized standard materials. *Journal of the Mechanics and Physics of Solids*, 82:218–234, 2015.

- [19] M. Canadija and J. Mosler. A variational formulation for thermomechanically coupled low cycle fatigue at finite strains. *International Journal of Solids and Structures*, 100:388–398, 2016.
- [20] E. R. Homer. High-throughput simulations for insight into grain boundary structure-property relationships and other complex microstructural phenomena. *Computational Materials Science*, 161:244–254, 2019.
- [21] J. W. Kang, K. Choi, W. H. Jo, and S. L. Hsu. Structure-property relationships of polyimides: a molecular simulation approach. *Polymer*, 39(26):7079–7087, 1998.
- [22] I. Usov, G. Nyström, J. Adamcik, S. Handschin, C. Schütz, A. Fall, et al. Understanding nanocellulose chirality and structure-properties relationship at the single fibril level. *Nature communications*, 6(1):7564, 2015.
- [23] J. Jancar, J.F. Douglas, F.W. Starr, S.K. Kumar, P. Cassagnau, A.J. Lesser, S.S. Sternstein, and M.J. Buehler. Current issues in research on structure-property relationships in polymer nanocomposites. *Polymer*, 51(15):3321–3343, 2010.
- [24] J. Zhang, X. Li, D. Xu, and R. Yang. Recent progress in the simulation of microstructure evolution in titanium alloys. *Progress in Natural Science: Materials International*, 29(3):295–304, 2019. Special Issue of Computational Materials.
- [25] V. B. Gupta, C. Ramesh, and A. K. Gupta. Structure-property relationship in heat-set poly(ethylene terephthalate) fibers. II. thermal behavior and morphology. *Journal of Applied Polymer Science*, 29(12):3727–3739, 1984.
- [26] A. Baranek, S. B. Song, M. McBride, P. Finnegan, and C. N. Bowman. Thermomechanical formation-structure-property relationships in photopolymerized copper-catalyzed azide-alkyne (CuAAC) networks. *Macromolecules*, 49(4):1191–1200, 2016.
- [27] B. Schlund, J. Guillot, C. Pichot, and A. Cruz. Structure-property relationships in styrene-butyl acrylate emulsion copolymers: 2. viscoelastic properties of latex films-experimental results and simulation. *Polymer*, 30(10):1883–1894, 1989.
- [28] W. Yan, S. Lin, O. Kafka, Y. Lian, C. Yu, and Z. Liu. Data-driven multi-scale multiphysics models to derive process-structure-property relationships for additive manufacturing. *Computational Mechanics*, 61, 05 2018.

- [29] L. Saucedo-Mora and T. J. Marrow. 3D cellular automata finite element method with explicit microstructure: Modeling quasi-brittle fracture using meshfree damage propagation. *Procedia Materials Science*, 3:1143–1148, 2014. 20th European Conference on Fracture.
- [30] M. Metzger and T. Seifert. Computational assessment of the microstructure-dependent plasticity of lamellar gray cast iron - part I: Methods and microstructure-based models. *International Journal of Solids and Structures*, 66:184–193, 2015.
- [31] S. Balasivanandha Prabu and L. Karunamoorthy. Microstructure-based finite element analysis of failure prediction in particle-reinforced metal-matrix composite. *Journal of Materials Processing Technology*, 207(1):53–62, 2008.
- [32] A. B. Phillion, S. L. Cockcroft, and P. D. Lee. Predicting the constitutive behavior of semi-solids via a direct finite element simulation: application to AA5182. *Modelling and Simulation in Materials Science and Engineering*, 17(5):055011, jun 2009.
- [33] K. Kim, B. Forest, and J. Geringer. Two-dimensional finite element simulation of fracture and fatigue behaviours of alumina microstructures for hip prosthesis. *Proceedings of the Institution of Mechanical Engineers, Part H: Journal of Engineering in Medicine*, 225(12):1158–1168, 2011.
- [34] N. Baati, A. Nanchen, F. Stoessel, and T. Meyer. Predictive models for thermal behavior of chemicals with quantitative structure-property relationships. *Chemical Engineering & Technology*, 38(4):645–650, 2015.
- [35] M. Shibata, R. Yosomiya, J. Wang, Y. Zheng, W. Zhang, and Z. Wu. Relationship between molecular structure and thermal properties of poly(aryl ether ketone)s. *Macromolecular Rapid Communications*, 18(2):99–105, 1997.
- [36] P. Satyanarayan, V. Rahul, S. Niraj, and C.R. Bowen. Finite element analysis of the microstructure of AlN-TiN composites. *Strain*, 50(3):250–261, 2014.
- [37] G. Capuano and J. J. Rimoli. Smart finite elements: A novel machine learning application. *Computer Methods in Applied Mechanics and Engineering*, 345:363–381, 2019.
- [38] Z. Nie, H. Jiang, and L. B. Kara. Deep learning for stress field prediction using convolutional neural networks. *arXiv preprint arXiv:1808.08914*, 2018.

- [39] J. Wei, X. Chu, X. Y. Sun, K. Xu, H. Deng, J. Chen, Z. Wei, and M. Lei. Machine learning in materials science. *InfoMat*, 1(3):338–358, 2019.
- [40] C. Herriott and A. D. Spear. Predicting microstructure-dependent mechanical properties in additively manufactured metals with machine-and deep-learning methods. *Computational Materials Science*, 175:109599, 2020.
- [41] S. M. Azimi, D. Britz, M. I. Engstler, M. Fritz, and F. Mücklich. Advanced steel microstructural classification by deep learning methods. *Scientific Reports*, 8(1):1–14, 2018.
- [42] D. Mery. Aluminum casting inspection using deep learning: A method based on convolutional neural networks. *Journal of Nondestructive Evaluation*, 39(1):12, 2020.
- [43] M. K. Ferguson, A. K. Ronay, Y. Tsun T. Lee, and K. H. Law. Detection and segmentation of manufacturing defects with convolutional neural networks and transfer learning. *Smart and Sustainable Manufacturing Systems*, 2, 2018.
- [44] X. Li, Y. i Zhang, H. Zhao, C. Burkhart, L. C. Brinson, and W. Chen. A transfer learning approach for microstructure reconstruction and structure-property predictions. *Scientific Reports*, 8(1):1–13, 09 2018.
- [45] B. L. DeCost, B. Lei, T. Francis, and E. A. Holm. High throughput quantitative metallography for complex microstructures using deep learning: A case study in ultrahigh carbon steel. *Microscopy and Microanalysis*, 25(1):21–29, 2019.
- [46] A. Chowdhury, E. Kautz, B. Yener, and D. Lewis. Image driven machine learning methods for microstructure recognition. *Computational Materials Science*, 123:176–187, 2016.
- [47] B. L. DeCost and E. A. Holm. A computer vision approach for automated analysis and classification of microstructural image data. *Computational Materials Science*, 110:126–133, 2015.
- [48] L. Exl, J. Fischbacher, A. Kovacs, H. Oezelt, M. Gusenbauer, K. Yokota, T. Shoji, G. Hrkac, and T. Schrefl. Magnetic microstructure machine learning analysis. *Journal of Physics: Materials*, 2(1):014001, 2018.

- [49] B. Yucel, S. Yucel, A. Ray, L. Duprez, and S. R. Kalidindi. Mining the correlations between optical micrographs and mechanical properties of cold-rolled hsla steels using machine learning approaches. *Integrating Materials and Manufacturing Innovation*, 9(3):240–256, 2020.
- [50] B.S.S Pokuri, S. Ghosal, A. Kokate, S. Sarkar, and B. Ganapathysubramanian. Interpretable deep learning for guided microstructure-property explorations in photovoltaics. *npj Computational Materials*, 5(1):1–11, 2019.
- [51] F. Nikolić, I. Štajduhar, and M. Čanađija. Aluminum microstructure inspection using deep learning: a convolutional neural network approach toward secondary dendrite arm spacing determination. In *4th edition of My First Conference, University of Rijeka, Faculty of Engineering, Rijeka, Croatia*,, 2020.
- [52] F. Nikolić, I. Štajduhar, and M. Čanađija. Casting microstructure inspection using computer vision: Dendrite spacing in aluminum alloys. *Metals*, 11(5):756, 2021.
- [53] F. Nikolić, I. Štajduhar, and M. Čanađija. Casting defects detection in aluminum alloys using deep learning: a classification approach. *International Journal of Metalcasting*, 2022.
- [54] F. Nikolić and M. Čanađija. Deep learning of temperature - dependent deep learning of temperature - dependent stress - strain hardening curves. *Comptes Rendus Mecanique, Accepted for publication*, 2023.
- [55] F. Nikolić and M. Čanađija. Machine learning of structure–property relationships: An application to heat generation during plastic deformation. *Facta Universitatis, Series: Mechanical Engineering*, 2024.
- [56] E. King, Y. Li, S. Hu, and E. Machorro. Physics-informed machine-learning model of temperature evolution under solid phase processes. *Computational Mechanics*, 72(1):125–136, 2023.
- [57] O. Pantalé, P. T. Mha, and A. Tongne. Efficient implementation of non-linear flow law using neural network into the abaqus explicit fem code. *Finite Elements in Analysis and Design*, 198:103647, 2022.

- [58] M. Zlatić and M. Čanađija. Incompressible rubber thermoelasticity: a neural network approach. *Computational mechanics*, 71(5):895–916, 2023.
- [59] H. Zhang, Z. Guo, H. Hu, G. Zhou, Q. Liu, Y. Xu, D. Qian, and D. Dai. A novel structure-property relationship model based on machine learning. *Modelling and Simulation in Materials Science and Engineering*, 28(3):035002, 2020.
- [60] J. Jung, Jae I. Y., Hyung K. P., Jin Y. K., and Hyoung S. K. An efficient machine learning approach to establish structure-property linkages. *Computational Materials Science*, 156:17–25, 2019.
- [61] M. I. Latypov and S. R. Kalidindi. Data-driven reduced order models for effective yield strength and partitioning of strain in multiphase materials. *Journal of Computational Physics*, 346:242–261, 2017.
- [62] Z. Yang, Y. C. Yabansu, R. Al-Bahrani, W. Liao, A. N. Choudhary, S. R. Kalidindi, and A. Agrawal. Deep learning approaches for mining structure-property linkages in high contrast composites from simulation datasets. *Computational Materials Science*, 151:278–287, 2018.
- [63] Y. Wang, M. Zhang, A. Lin, A. Iyer, A. S. Prasad, X. Li, Y. Zhang, L. S. Schadler, W. Chen, and L. C. Brinson. Mining structure–property relationships in polymer nanocomposites using data driven finite element analysis and multi-task convolutional neural networks. *Molecular Systems Design & Engineering*, 5(5):962–975, 2020.
- [64] A.T. Cecen, H. Dai, Y. C. Yabansu, S. R. Kalidindi, and L. Song. Material structure-property linkages using three-dimensional convolutional neural networks. *Acta Materialia*, 146:76–84, 2018.
- [65] Z. Liu, C.T. Wu, and M. Koishi. Transfer learning of deep material network for seamless structure–property predictions. *Computational Mechanics*, 64(2):451–465, 2019.
- [66] S. Kotha, D. Ozturk, and S. Ghosh. Parametrically homogenized constitutive models (phcms) from micromechanical crystal plasticity fe simulations, part i: Sensitivity analysis and parameter identification for titanium alloys. *International Journal of Plasticity*, 120:296–319, 2019.

- [67] A. Frankel, C. Safta, C. Alleman, and R. Jones. Mesh-based graph convolutional neural network models of processes with complex initial states. *CoRR*, abs/2107.00090, 2021.
- [68] U. M. Chaudry, R. Jaafreh, A. Malik, T. Jun, K. Hamad, and T. Abuhmed. A comparative study of strain rate constitutive and machine learning models for flow behavior of az31-0.5 ca mg alloy during hot deformation. *Mathematics*, 10(5), 2022.
- [69] K. Jiang, Q. Han, Y. Bai, and X. Du. Data-driven ultimate conditions prediction and stress-strain model for frp-confined concrete. *Composite Structures*, 242:112094, 2020.
- [70] Jici W., Qingrong Z., and Yujie W. Physics-driven machine learning model on temperature and time-dependent deformation in lithium metal and its finite element implementation. *Journal of the Mechanics and Physics of Solids*, 153:104481, 2021.
- [71] C. Yang, Y. Kim, S. Ryu, and G. X. Gu. Prediction of composite microstructure stress-strain curves using convolutional neural networks. *Materials & Design*, 189:108509, 2020.
- [72] D. Versino, A. Tonda, and C. Bronkhorst. Data driven modeling of plastic deformation. *Computer Methods in Applied Mechanics and Engineering*, 318, 02 2017.
- [73] G. Kronberger, E. Kablman, J. Kronsteiner, and M. Kommenda. Extending a physics-based constitutive model using genetic programming. *Applications in Engineering Science*, 9:100080, 2022.
- [74] E. del Castillo, L. Basañez, and E. Gil. Modeling non-linear viscoelastic behavior under large deformations. *International Journal of Non-Linear Mechanics*, 57:154–162, 2013.
- [75] R. Kumar P., M. Ruzzene, and J. J. Rimoli. A continuum model for nonlinear lattices under large deformations. *International Journal of Solids and Structures*, 96:300–319, 2016.
- [76] M. Kamkar, M. Janmaleki, E. Erfanian, A. Sanati-N., and U. Sundararaj. Viscoelastic behavior of covalently crosslinked hydrogels under large shear deformations: An approach to eliminate wall slip. *Physics of Fluids*, 33(4), 2021.
- [77] X. Jia, K. Hao, Z. Luo, and Z. Fan. Plastic deformation behavior of metal materials: A review of constitutive models. *Metals*, 12(12), 2022.

- [78] X. Wang, J. Gao, Y. Wang, J. Bai, Z. Zhao, and C. Luo. Finite element analysis for linear viscoelastic materials considering time-dependent poisson's ratio: Variable stiffness method. *Applied Sciences*, 14(8), 2024.
- [79] Y. Yi, H. Dong, Z. Wei, G. Yanfei, P. Jorge, and F. Zhili. Identifying multiple synergistic factors on the susceptibility to stress relaxation cracking in variously heat-treated weldments. *Mechanics of Materials*, 195:105013, 2024.
- [80] S. Akhtar and B. Li. Modeling time-dependent uniaxial compressive behaviors of an artificial frozen sandy clay at different temperatures. *Geotechnical and Geological Engineering*, pages 1–14, 2024.
- [81] Z. Yang, Z.G. Lu, L. Jie, Y. Hailin, T. Chuxuan, N. Yongpeng, and Z. Jing. Creep behavior and viscoelastic-plastic models for polymer-blend hdpe geocell sheets based on the stepped isothermal method. *Geotextiles and Geomembranes*, 52(1):132–144, 2024.
- [82] S. A. Nabavizadeh, M. Eshraghi, and S. D. Felicelli. Three-dimensional phase field modeling of columnar to equiaxed transition in directional solidification of inconel 718 alloy. *Journal of Crystal Growth*, 549:125879, 2020.
- [83] K. Bzowski, Ł. Rauch, M. Pietrzyk, M. Kwiecień, and K. Muszka. Numerical modeling of phase transformations in dual-phase steels using level set and sssve approaches. *Materials*, 14(18), 2021.
- [84] M. Maggini, G. Falcucci, A. Rosati, S. Ubertini, and A. L. Facci. Non-dimensional numerical analysis of coupled metal hydride-phase change material hydrogen storage system. *Journal of Energy Storage*, 93:112230, 2024.
- [85] Z. Chen, D. Gao, and J. Shi. Experimental and numerical study on melting of phase change materials in metal foams at pore scale. *International Journal of Heat and Mass Transfer*, 72:646–655, 2014.
- [86] Y. Tian and C. Y. Zhao. A numerical investigation of heat transfer in phase change materials (pcms) embedded in porous metals. *Energy*, 36(9):5539–5546, 2011.
- [87] M. Čanađija. *Thermomechanics of Solids and Structures: Physical Mechanisms, Continuum Mechanics, and Applications*. Elsevier, 2023.

- [88] L. Jean and C. Jean-Louis. *Mechanics of solid materials*. Cambridge university press, 1994.
- [89] A. Lallit and G. Sanjay. *Continuum mechanics of solids*. Oxford University Press, 2020.
- [90] M. A. Groeber and M. A. Jackson. DREAM.3D: a digital representation environment for the analysis of microstructure in 3D. *Integrating Materials and Manufacturing Innovation*, 3(1):56–72, 2014.
- [91] X. Li, Z. Liu, S. Cui, C. Luo, C. Li, and Z. Zhuang. Predicting the effective mechanical property of heterogeneous materials by image based modeling and deep learning. *Computer Methods in Applied Mechanics and Engineering*, 347:735–753, 2019.
- [92] D. W. Abueidda, M. Almasri, R. Ammourah, U. Ravaioli, I. M. Jasiuk, and N. A. Sobh. Prediction and optimization of mechanical properties of composites using convolutional neural networks. *Composite Structures*, 227:111264, 2019.
- [93] Y. Sang, L. Bo, L. Qunyang, Ping Z.H., and Qiao F.X. Deep neural network method for predicting the mechanical properties of composites. *Applied Physics Letters*, 115(16):161901, 2019.
- [94] A. Mortensen and J. Llorca. Metal matrix composites. *Annual review of materials research*, 40:243–270, 2010.
- [95] G. Al Kassem. *Micromechanical material models for polymer composites through advanced numerical simulation techniques*. PhD thesis, 2009.
- [96] V. Kouznetsova, M. G. D. Geers, and W. A. M. Brekelmans. Multi-scale constitutive modelling of heterogeneous materials with a gradient-enhanced computational homogenization scheme. *International Journal for Numerical Methods in Engineering*, 54(8):1235–1260, 2002.
- [97] M.G.D. Geers, V.G. Kouznetsova, and W.A.M. Brekelmans. Multi-scale computational homogenization: Trends and challenges. *Journal of Computational and Applied Mathematics*, 234(7):2175–2182, 2010. Fourth International Conference on Advanced Computational Methods in ENgineering (ACOMEN 2008).

- [98] M. Smith. *ABAQUS/Standard User's Manual, Version 6.9*. Dassault Systèmes Simulia Corp, United States, 2009.
- [99] W. Jianxin. Introduction to convolutional neural networks. *National Key Lab for Novel Software Technology. Nanjing University. China*, 5(23):495, 2017.
- [100] Zhang X. Ren S. Sun J. Kaiming, H. Delving deep into rectifiers: Surpassing human-level performance on imagenet classification. In *Proceedings of the IEEE international conference on computer vision*, pages 1026–1034, 2015.
- [101] Hossein Gholamalinezhad and Hossein Khosravi. Pooling methods in deep neural networks, a review. *arXiv preprint arXiv:2009.07485*, 2020.
- [102] Aamir M. Mohd N. Arshad A. Riaz S. Alruban A. Dutta A. K. Almotairi S. Zafar, A. A comparison of pooling methods for convolutional neural networks. 12(17).
- [103] D. P. Kingma and J. Ba. Adam: A method for stochastic optimization. *arXiv preprint arXiv:1412.6980*, 2014.
- [104] Jersson X. L.-M., Maribel A., D. A. Tibaduiza, and F. Pozo. Manifold learning algorithms applied to structural damage classification. *Journal of Applied and Computational Mechanics*, 7(Special Issue):1158–1166, 2021.
- [105] A. Anestis. Smoothing noisy data with coiflets. *Statistica Sinica*, pages 651–678, 1994.
- [106] W. S. Cleveland and C. Loader. Smoothing by local regression: Principles and methods. In *Statistical Theory and Computational Aspects of Smoothing: Proceedings of the COMPSTAT'94 Satellite Meeting held in Semmering, Austria, 27–28 August 1994*, pages 10–49. Springer, 1996.

List of Figures

- 1.1 Schematic representation of the process of SPR and their representative evaluation by numerical simulations. 3
- 1.2 Schematic representation of the process of plastic deformation-induced head generation. 5
- 4.1 Schematic representation of the numerical procedure used in the present research. 33
- 4.2 An example of unique RVE configuration: RVE size and a random microstructural configuration: (a) arrangement of the hard and soft phases (spatial distribution) within the RVE framework and (b) visualization of the arrangement of the hard phase within the RVE discarding the soft phase. 37
- 4.3 Representative mechanical properties and their variations based on the temperature-true stress and true plastic strain for (a) the soft phase and (b) the hard phase – stress-strain curves dataset. The symbols indicate the values used in the constitutive model. 39
- 4.4 Representative mechanical properties – true stress and true plastic strain for (a) the soft phase and (b) the hard phase – deformation-induced heating (TQC) dataset. The dots indicate the values used in the software constitutive model. . . 40
- 4.5 Illustration of a 2D unit cell under macro strain with PBC [95]. 43
- 4.6 Traction continuity condition on the boundary cell [95]. 44
- 4.7 Simplified visualization – application of PBC to the RVE [95]. 46

4.8 A random microstructure configuration of phases for an RVE including all six temperature levels and different fractions of phases (i.e., higher and lower phases fraction): (a) Temp = 20 °C hard ph. frct. = 0.143, (b) Temp = 50 °C hard ph. frct. = 0.008, (c) Temp = 100 °C hard ph. frct. = 0.078, (d) Temp = 150 °C hard ph. frct. = 0.072, (e) Temp = 200 °C hard ph. frct. = 0.038, (f) Temp = 250 °C hard ph. frct = 0.110. 49

4.9 Von Mises stress (MPa) at the final simulation increment for the analyzed RVEs shown in Fig 4.8: (a) Temp = 20 °C hard ph. frct. = 0.143, (b) Temp = 50 °C hard ph. frct. = 0.008, (c) Temp = 100 °C hard ph. frct. = 0.078, (d) Temp = 150 °C hard ph. frct. = 0.072, (e) Temp = 200 °C hard ph. frct. = 0.038, (f) Temp = 250 °C hard ph. frct. = 0.110. 50

4.10 Total displacement (mm) at the final simulation increment for the analyzed RVEs shown in Fig 4.8: (a) Temp = 20 °C hard ph. frct. = 0.143, (b) Temp = 50 °C hard ph. frct. = 0.008, (c) Temp = 100 °C hard ph. frct. = 0.078, (d) Temp = 150 °C hard ph. frct. = 0.072, (e) Temp = 200 °C hard ph. frct. = 0.038, (f) Temp = 250 °C hard ph. frct. = 0.110. 51

4.11 Equivalent plastic strain at the last simulation increment for the analyzed RVEs shown in Fig 4.8: (a) Temp = 20 °C hard ph. frct. = 0.143, (b) Temp = 50 °C hard ph. frct. = 0.008, (c) Temp = 100 °C hard ph. frct. = 0.078, (d) Temp = 150 °C hard ph. frct. = 0.072, (e) Temp = 200 °C hard ph. frct. = 0.038, (f) Temp = 250 °C hard ph. frct. = 0.110. 52

4.12 Equivalent plastic strain at the last simulation increment for the analyzed RVEs shown in Fig 4.8 (i.e., only the hard phase is shown): (a) Temp = 20 °C hard ph. frct. = 0.143, (b) Temp = 50 °C hard ph. frct. = 0.008, (c) Temp = 100 °C hard ph. frct. = 0.078, (d) Temp = 150 °C hard ph. frct. = 0.072, (e) Temp = 200 °C hard ph. frct. = 0.038, (f) Temp = 250 °C hard ph. frct. = 0.110. 53

4.13 A random microstructure configuration of phases for three different RVEs including lower and higher phase fractions: (a) RVE 1: Hard phase fraction = 0.143, (b) RVE 2: Hard phase fraction = 0.082, (b) RVE 3: Hard phase fraction = 0.014. 54

4.14	Von Mises stress (MPa) at the final simulation increment for the analyzed RVEs shown in Fig 4.14 (i.e., a section of each RVE has been intentionally removed for better visualization): (a) RVE 1, (b) RVE 2, (c) RVE 3.	55
4.15	Total displacement (mm) at the final simulation increment for the analyzed RVEs shown in Fig 4.15 (i.e., a section of each RVE has been intentionally removed for better visualization): (a) RVE 1, (b) RVE 2, (c) RVE 3.	56
4.16	Equivalent plastic strain at the final simulation increment for the analyzed RVEs shown in Fig 4.16 (i.e., a section of each RVE has been intentionally removed for better visualization): (a) RVE 1, (b) RVE 2, (c) RVE 3.	56
4.17	Equivalent plastic strain at the final simulation increment for the analyzed RVEs shown in Fig 4.17 (i.e., only the hard phase is shown): (a) RVE 1, (b) RVE 2, (c) RVE 3.	57
4.18	An example of the incremental true stress-strain response of the RVE shown in Fig. 4.2. The simulation is performed at ambient conditions of 20 °C. The plotted dots indicate each of 20 increments.	57
4.19	Mesh convergence vs von Mises stress for the soft and hard phases under varying mesh densities.	59
4.20	Detailed schematic representation of the ML process employed for utilizing the temperature increase-strain dataset.	62
4.21	Detailed schematic representation of the ML process employed for utilizing the stress-strain dataset.	63
4.22	Detailed schematic representation of the ML model utilized for correlating the temperature increase-strain dataset.	64
4.23	Detailed schematic representation of the ML model utilized for correlating the stress-strain dataset.	65
5.1	Comparison between the calculated (FEA) and the predicted (CNN) value of the stress for all points of the stress-strain curve for: (a) – CNN1 Model, (b) – CNN2 Model, (c) – CNN3 Model, (d) – CNN4 Model, (e) - CNN5 Model, (f) – CNN6 Model in Table A.1.	70

5.2 Comparison between the calculated (FEA) and the predicted (CNN) value of the temperature increase for all points of the temperature increase curve for: (a) – CNN1 Model, (b) – CNN2 Model, (c) – CNN3 Model, (d) – CNN4 Model, (e) – CNN5 Model, (f) – CNN6 Model in Table A.2. 71

5.3 Visualization of true stress-true strain curves predicted by the ML model and ones simulated by FEA. 73

5.4 Visualization of true stress-true strain curves predicted by the ML model: (a) colored by temperature level and (b) colored by hard phase fraction. 74

5.5 Comparison of stress values calculated by FEA with those predicted by the ML model for strain points 1, 2, 3 & 4. The graph includes the true stress-true strain curves calculated for all six temperature levels. 76

5.6 Comparison of stress values calculated by FEA with those predicted by the ML model for strain points 17, 18, 19 & 20. The graph includes the true stress-true strain curves calculated for all six temperature levels. 77

5.7 Stress values calculated by FEA and predicted by the ML model as a function of different temperatures. Plot includes temperatures from all six temperature levels and all 20 simulation increments of the true stress-true strain curve: (a) prediction error vs. temperature, (b) true stress vs. temperature (prediction error is color-coded). 78

5.8 Stress values calculated by FEA and predicted by the ML model as a function of different phases fraction. Plot includes temperatures from all six temperature levels and all 20 simulation increments of the true stress-true strain curve: (a) prediction error vs. temperature, (b) true stress vs. temperature (prediction error is color-coded). 79

5.9 Convergence of dataset size vs MSE. 80

5.10 Comparison of stress values calculated by FEA with those predicted by the ML model for random temperature levels for different hard phase fractions. The plot includes values from all 20 simulation increments of the true stress-true strain curve 82

5.11	Stress values from random temperature dataset calculated by FEA and predicted by the ML model as a function of different temperatures. Plot includes temperatures from all six temperature levels and all 20 simulation increments of the true stress-true strain curve: (a) prediction error vs. temperature, (b) true stress vs. temperature (prediction error is color-coded)	83
5.12	Stress values from random temperature dataset calculated by FEA and predicted by the ML model as a function of different phases fraction. Plot includes temperatures from all six temperature levels and all 20 simulation increments of the true stress-true strain curve: (a) prediction error vs. temperature, (b) true stress vs. temperature (prediction error is color-coded)	84
5.13	Visualization of temperature increase-strain curves predicted by the ML model and simulated by FEA (TQC of the last simulation increment is shown).	86
5.14	Visualization of temperature increase values calculated by FEA and values predicted by the ML model. The diagram contains temperature increase-strain points from all simulation increments – The percentage prediction error is color-coded.	87
5.15	Prediction error compared to TQC value. The plot includes values from the all 12 simulation increments. The actual TQC value (β) for the last simulation increment is displayed.	88
5.16	Visualization of temperature increase values calculated by FEA for various TQC values including all 12 simulation increments and complete TQC range – The percent prediction error is color-coded, the actual TQC (β) for the last simulation increment is displayed.	88
5.17	Prediction error for the proportion of hard phase. The plot includes values from all 12 simulation increments.	89
5.18	Visualization of the values calculated by FEA and those predicted by the ML model for the temperature increase at different proportions of the hard phase. All 12 simulation increments are included – The percentage prediction error is color-coded. The arrows indicate the highest temperature increase.	89
5.19	Distance between the CoGs of the hard and soft phases for all 20 points on the stress-strain curve: (a) including prediction error, and (b) showing the true stress.	91

5.20 Distance between the CoGs of the hard phase from RVE center for all 20 points on the stress-strain curve: (a) including prediction error, and (b) showing the true stress. 92

5.21 The standard deviation of the center of gravity distances for all elements of an RVE from the CoG center across all RVEs for all 20 points of the stress-strain curve for the soft phase is depicted as follows: (a) in relation to the prediction error, and (b) in relation to the true stress. 93

5.22 The standard deviation of the center of gravity distances for all elements of an RVE from the CoG center across all RVEs for all 20 points of the stress-strain curve for the hard phase is depicted as follows: (a) in relation to the prediction error, and (b) in relation to the true stress. 94

5.23 Scatter matrix of all 20 points of the stress-strain curve for all RVEs, showing the CoG distances of the hard phase from the center, the standard deviation, the mean distances of the hard and soft phases from the center, the hard phase fractions, and the prediction error. 95

5.24 Distance between the CoGs of the hard and soft phases for all 12 points on the temperature increase curve: (a) including prediction error, and (b) showing the temperature increase. 97

5.25 Distance between the CoGs of the hard phase from RVE center for all 12 points on the temperature increase curve: (a) including prediction error and, (b) showing the temperature increase. 98

5.26 The standard deviation of the center of gravity distances for all elements of an RVE from the center of gravity center across all RVEs for all 12 points of the temperature increase curve for the soft phase is depicted as follows: (a) in relation to the prediction error, and (b) in relation to the temperature increase. . . . 99

5.27 The standard deviation of the center of gravity distances for all elements of an RVE from the center of gravity center across all RVEs for all 12 points of the temperature increase curve for the hard phase is depicted as follows: (a) in relation to the prediction error, and (b) in relation to the temperature increase. . . 100

5.28 Scatter matrix of all 12 points of the temperature increase curve for all RVEs, showing the CoG distances of the hard phase from the center, the standard deviation, the mean distances of the hard and soft phases from the center, the hard phase fractions, and the prediction error. 101

A.1 Comparison of train MSE, validation MSE, RMSE, maximum error and computational time for CNN models: (a) for stress-strain dataset, and (b) deformation induced heating dataset. 127

List of Tables

- 4.1 Number of simulations performed for different temperature levels. 48
- 4.2 The von Mises stress convergence analysis for the soft and hard phases under varying mesh densities. 58

- A.1 CNN Models configuration and performance – stress-strain dataset. 125
- A.2 CNN Models configuration and performance – deformation-induced heating dataset. 126

Appendix A

A.1 Optimization of ML Models

In this section, different CNN configurations are presented to compare the performances of different CNN configurations and to show general trend of predictive capability versus ML model complexity. Several experiments have been undertaken with various CNN configurations to identify the most effective one. As already explained, simple ML algorithms such as ANNs are not even considered for the present task due to the complexity of the task. Instead, this section focuses on six specific CNN model architectures. These six CNN configurations were evaluated using the test dataset, and their respective performance metrics are reported. The analysis centered on the maximum global prediction error (i.e., maximum single error in all of the predictions), MSE, and root mean squared error (RMSE). Detailed results can be found in Tables A.1 and A.2 and Fig A.1. All strain increments were incorporated in the evaluation process of stress-strain dataset while increments 8-20 were incorporated in the evaluation process of temperature-increase dataset. Based on the data in Tables A.1 and A.2, CNN1 configuration, with its configuration slightly varying across both datasets, exhibited the best performance. Consequently, CNN1 was selected for the current task for both datasets. Otherwise, the errors between other CNN configurations showed similar trends for both datasets. Moreover, RMSE, MSE and global error trends are much lower for the stress-strain dataset. This should indicate that capturing of the stress-strain curves was a simpler task than capturing temperature-increase curves for the ML model. As already mentioned, simpler ML models such as ANNs or other shallow learning approaches are not even considered in this study due to the complexity of the problem (e.g., even the simple CNN configurations didn't perform well on the task at hand). Additionally, a summary comparison of the performance of these various CNN configurations is provided in Chapter 5.

Table A.1: CNN Models configuration and performance – stress-strain dataset.

Model	CNN Configuration	MSE	RMSE	Error	Comp. Time
CNN1	CL_1 (f-16, (26x26x26x32) – Cf(8x8x8x32) A-PRReLU), BN, Mp_1 ((13x13x13x32) – Mpf(6x6x6x32)) CL_2 (f-16, (13x13x13x32) – Cf(5x5x5x32) A-PRReLU), BN, Mp_2 ((8x8x8x32) – Mpf(4x4x5x32)) CL_3 (f-16, (8x8x8x32) – Cf(3x3x3x32) A-PRReLU), BN, Mp_2 ((4x4x4x32) – Mpf(2x2x2x32)) D(4112, A-PRReLU), D(2056, A-PRReLU), D(1028, A-PRReLU), D(512, A-PRReLU), BN, D(256, A-PRReLU), BN, BN, D(64, A-PRReLU), BN, D(20, A-PRReLU), BN, Output (Opt: Adam), N.o.T.P: 11 824 724	1.86	1.32	7 %	82 min
CNN2	CL_1 (f-16, (26x26x26x32) – Cf(5x5x5x32) A-PRReLU), BN, Mp_1 ((13x13x13x32) – Mpf(2x2x2x32)) CL_2 (f-16, (13x13x13x32) – Cf(3x3x3x32) A-PRReLU), BN, Mp_2 ((8x8x8x32) – Mpf(2x2x2x32)) D(1024, A-PRReLU), D(0.5), BN, D(512, A-PRReLU), D(0.5), BN, D(256, A-PRReLU), D(0.5), BN, D(128, A-PRReLU), BN, D(64, A-PRReLU), BN, D(20, A-PRReLU), BN, Output, (Opt: Adam), N.o.T.P: 8 155 516	13.05	3.58	25 %	52 min
CNN3	CL_1 (f-16, (26x26x26x32) – Cf(5x5x5x32) A-ReLU), BN, Mp_1 ((13x13x13x32) – Mpf(2x2x2x32)) CL_2 (f-16, (13x13x13x32) – Cf(3x3x3x32) A-ReLU), BN, Mp_2 ((8x8x8x32) – Mpf(2x2x2x32)) D(1024, A-ReLU), D(0.5), BN, D(512, A-ReLU), D(0.5), BN, D(256, A-ReLU), D(0.5), BN, D(128, A-ReLU), BN, D(64, A-ReLU), BN, D(20, A-ReLU), BN, Output, (Opt: SGD), N.o.T.P: 7 801 992	76.45	8.94	25 %	48 min
CNN4	CL_1 (f-16, (26x26x26x32) – Cf(8x8x8x32) A-PRReLU), BN, Mp_1 ((13x13x13x32) – Mpf(6x6x6x32)) CL_2 (f-16, (13x13x13x32) – Cf(5x5x5x32) A-PRReLU), BN, Mp_2 ((8x8x8x32) – Mpf(4x4x4x32)) D(512, A-PRReLU), BN, D(256, A-PRReLU), BN, D(128, A-PRReLU), Output, (Opt: Adam), N.o.T.P: 667 492	59.54	7.58	23 %	49 min
CNN5	CL_1 (f-16, (26x26x26x32) – Cf(5x5x5x32) A-ReLU), BN, Mp_1 ((13x13x13x32) – Mpf(4x4x4x32)) CL_2 (f-16, (13x13x13x32) – Cf(3x3x3x32) A-ReLU), BN, Mp_2 ((8x8x8x32) – Mpf(3x3x3x32)) D(256, A-ReLU), BN, D(128, A-ReLU), BN, Output, (Opt: SGD), No.T.P: 1 077 332	89.85	8.94	56 %	34 min
CNN6	CL_1 (f-16, (26x26x26x32) – Cf(5x5x5x32) A-ReLU), BN, Mp_1 ((13x13x13x32) – Mpf(4x4x4x32)) D(128, A-ReLU), BN, Output, (Opt: SGD), N.o.T.P: 3 544 244	36.31	5.79	32 %	25 min

Legend: CLx – 3D convolutional layer, f – number of filters, Cf – number of convolutional filters, A – Activation function, Mpx – Max pooling layer, Mpf – Number of max pooling filters BN – batch normalization layer, Dr – Dropout layer, D – Dense (fully connected layers), Opt - Optimizer, N.o.T.P - Number of trainable parameters (Weights)

Table A.2: CNN Models configuration and performance – deformation-induced heating dataset.

Model	CNN Configuration	MSE	RMSE	Error	Comp. Time
CNN1	CL_1 (f-16, (26x26x26x32) – Cf(8x8x8x32) A-PRReLU), BN, Mp_1 ((13x13x13x32) – Mpf(6x6x6x32)) CL_2 (f-16, (13x13x13x32) – Cf(5x5x5x32) A-PRReLU), BN, Mp_2 ((8x8x8x32) – Mpf(4x4x4x32)) D(512, A-PRReLU), BN, D(256, A-PRReLU), BN, D(128, A-PRReLU), BN, D(64, A-PRReLU), BN, D(20, A-PRReLU), BN, Output (Opt: Adam), No.T.P: 672 084	1.94e-5	0.004	6 %	68 min
					N.O. Weights: 673 084
CNN2	CL_1 (f-16, (26x26x26x32) – Cf(5x5x5x32) A-PRReLU), BN, Mp_1 ((13x13x13x32) – Mpf(2x2x2x32)) CL_2 (f-16, (13x13x13x32) – Cf(3x3x3x32) A-PRReLU), BN, Mp_2 ((8x8x8x32) – Mpf(2x2x2x32)) D(1024, A-PRReLU), D(0.5), BN, D(512, A-PRReLU), D(0.5), BN, D(256, A-PRReLU), D(0.5), BN, D(128, A-PRReLU), BN, D(64, A-PRReLU), BN, D(20, A-PRReLU), BN, Output, (Opt: Adam), N.o.T.P: 8 155 516	2.97e-5	0.005	20 %	54 min
CNN3	CL_1 (f-16, (26x26x26x32) – Cf(5x5x5x32) A-ReLU), BN, Mp_1 ((13x13x13x32) – Mpf(2x2x2x32)) CL_2 (f-16, (13x13x13x32) – Cf(3x3x3x32) A-ReLU), BN, Mp_2 ((8x8x8x32) – Mpf(2x2x2x32)) D(1024, A-ReLU), D(0.5), BN, D(512, A-ReLU), D(0.5), BN, D(256, A-ReLU), D(0.5), BN, D(128, A-ReLU), BN, D(64, A-ReLU), BN, D(20, A-ReLU), BN, Output, (Opt: SGD), N.o.T.P: 7 801 992	0.01	0.094	400 %	42 min
CNN4	CL_1 (f-16, (26x26x26x32) – Cf(8x8x8x32) A-PRReLU), BN, Mp_1 ((13x13x13x32) – Mpf(6x6x6x32)) CL_2 (f-16, (13x13x13x32) – Cf(5x5x5x32) A-PRReLU), BN, Mp_2 ((8x8x8x32) – Mpf(4x4x4x32)) D(512, A-PRReLU), BN, D(256, A-PRReLU), BN, D(128, A-PRReLU), Output, (Opt: Adam), N.o.T.P: 667 492	6.52e-5	0.007	50 %	52 min
CNN5	CL_1 (f-16, (26x26x26x32) – Cf(5x5x5x32) A-ReLU), BN, Mp_1 ((13x13x13x32) – Mpf(4x4x4x32)) CL_2 (f-16, (13x13x13x32) – Cf(3x3x3x32) A-ReLU), BN, Mp_2 ((8x8x8x32) – Mpf(3x3x3x32)) D(256, A-ReLU), BN, D(128, A-ReLU), BN, Output, (Opt: SGD), No.T.P: 1 077 332	0.03	0.17	1400 %	38 min
CNN6	CL_1 (f-16, (26x26x26x32) – Cf(5x5x5x32) A-ReLU), BN, Mp_1 ((13x13x13x32) – Mpf(4x4x4x32)) D(128, A-ReLU), BN, Output, (Opt: SGD), N.o.T.P: 3 544 244	0.07	0.26	2000 %	28 min
Legend:	CLx – 3D convolutional layer, f – number of filters, Cf – number of convolutional filters, A – Activation function, Mpx – Max pooling layer, Mpf – Number of max pooling filters BN – batch normalization layer, Dr – Dropout layer, D – Dense (fully connected layers), Opt - Optimizer, N.o.T.P - Number of trainable parameters (Weights)				

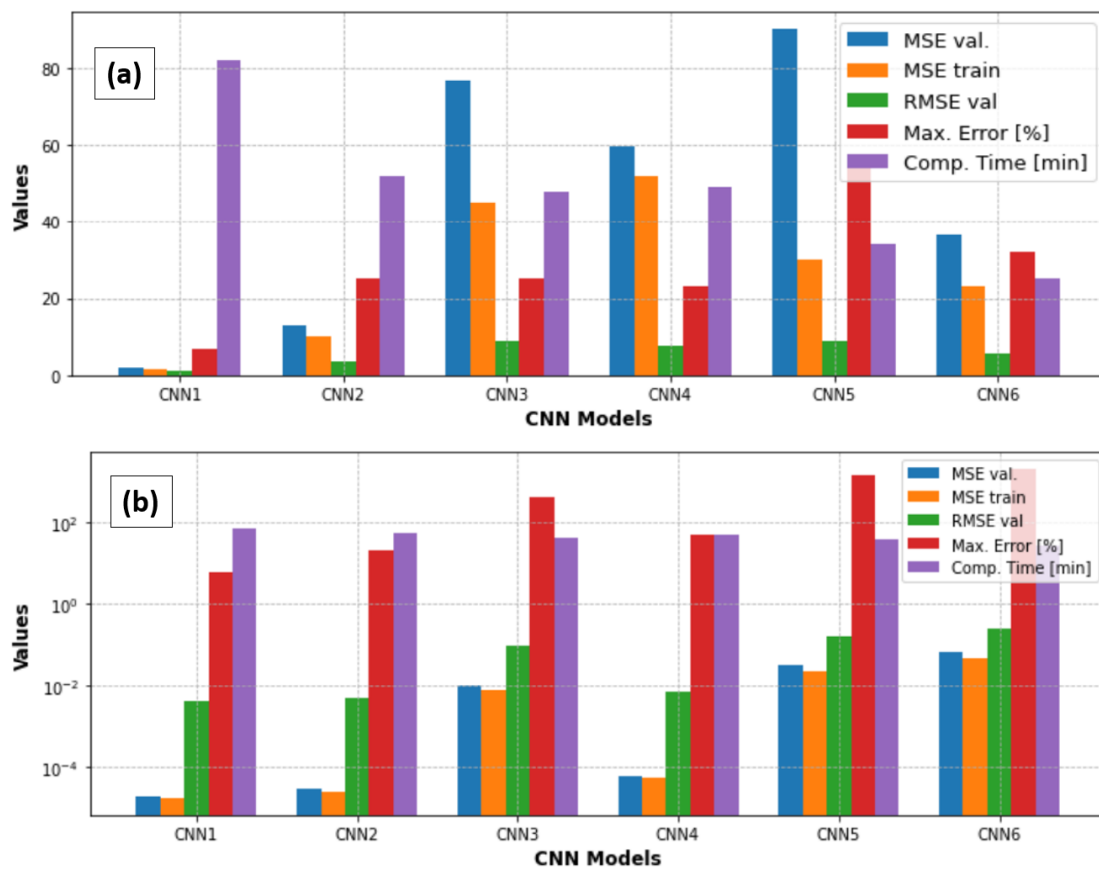


Figure A.1: Comparison of train MSE, validation MSE, RMSE, maximum error and computational time for CNN models: (a) for stress-strain dataset, and (b) deformation induced heating dataset.

Curriculum Vitae

Filip Nikolić was born on May 09, 1993, in Rijeka, Croatia. After completing his primary and secondary education, he enrolled mechanical engineering at University of Rijeka, Faculty of Engineering, in 2012. He completed his undergraduate and graduate university studies at the same institution in 2017. He then pursued a Ph.D. in Mechanical Engineering, specializing in Computational Mechanics, starting in 2019.

In 2017, just after completing studies, he began his professional career as a Project Engineer at Cimos d.d. Automotive Industry in Roč, Croatia, where he was in charge for developed of production processes for aluminum die cast products for turbocharging and powertrain automotive components. From 2018 to 2020, he advanced to a CAE Simulation Engineer role at Cimos d.d. Automotive Industry in Koper, Slovenia, focusing on numerical analysis various automotive components for turbocharging, powertrain and electric mobility. During this time, he conducted a lot of advanced FEA and CFD simulations. His responsibilities included optimizing casting designs, predicting mechanical properties, and ensuring the accuracy of simulation results through physical testing. In early 2020, he was promoted to Senior CAE Simulation Engineer and relocated to Buzet Plant in Croatia which ended in January 2021.

In January 2021, he joined Elaphe Propulsion Technologies Ltd. as a Senior CAE Simulation Engineer in Ljubljana, Slovenia. In this role, he mastered FEA and CFD analyses and Abaqus Software, managed multiple projects in the CAE and testing domain, supported the design and qualification process of electric motors, and mentored colleagues in the use of simulation softwares such as Abaqus, Tosca, fe-safe and Solidworks. This role ended in January 2024.

In January 2024, he joined Aventa Adriatic d.o.o company (Branch of Aventa) as a Pipeline Design Engineer in Rijeka, Croatia. In this role which is currently ongoing, the focus is on design and Installation of subsea rigid pipelines and cables as well as the internal development and enhancement of numerical analyses and simulation procedures.

In addition to his full time employment, Filip co-founded Fizio Tech d.o.o. in September

2018, a startup company focused on developing specialized technical solutions in rehabilitation industry. He led the company's technical development, secured a successful patent application, and supported prototype testing on physical patients. His responsibilities included design of components and products, numerical simulations, creation of technical standards, and collaboration with component suppliers.

Filip has also been involved in several research projects at the University of Rijeka, including "Mechanical Behavior of Nanostructures" and "Nonlocal Mechanical Models of Nanobeams." under the supervision of Professor Marko Čanađija.

Filip is fluent in Croatian and English, with intermediate proficiency in Slovenian and basic knowledge of Italian and German.

List of Publications

F. Nikolić and M. Čanađija. Machine Learning of Structure-Property Relationships: an Application to Heat Generation During Plastic Deformation. *Facta Universitatis, Series: Mechanical Engineering*, 2024. doi: 10.22190/FUME240215019N

F. Nikolić and M. Čanađija. Deep Learning of Temperature – Dependent Stress – Strain Hardening Curves. *Comptes Rendus. Mécanique*, 351, 151-170, 2023. doi: 10.5802/crmeca.185

F. Nikolić, I. Štajduhar, and Marko Čanađija. Casting Defects Detection in Aluminum Alloys Using Deep Learning: a Classification Approach. *International Journal of Metalcasting*. *International Journal of Metalcasting*, 17, 386–398, 2022. doi: <https://doi.org/10.1007/s40962-022-00777-x>.

F. Nikolić, I. Štajduhar, and M. Čanađija. Deep Learning for Casting Microstructure Inspection: A Convolutional Neural Network Approach. *My First Conference*, University of Rijeka: Faculty of Maritime Studies, 2021.

F. Nikolić, I. Štajduhar, and M. Čanađija. Casting Microstructure Inspection Using Computer Vision: Dendrite Spacing in Aluminum Alloys. *Metals*, 11(5) 756, 2021. doi: <https://doi.org/10.3390/met11050756>

F. Nikolić, I. Štajduhar, and M. Čanađija. Aluminum Microstructure Inspection Using Deep Learning: a Convolutional Neural Network Approach Toward Secondary Dendrite Arm Spacing Determination. *My First Conference*, University of Rijeka: Faculty of Engineering, September 2020.

